



저작자표시-비영리-동일조건변경허락 2.0 대한민국

이용자는 아래의 조건을 따르는 경우에 한하여 자유롭게

- 이 저작물을 복제, 배포, 전송, 전시, 공연 및 방송할 수 있습니다.
- 이차적 저작물을 작성할 수 있습니다.

다음과 같은 조건을 따라야 합니다:



저작자표시. 귀하는 원저작자를 표시하여야 합니다.



비영리. 귀하는 이 저작물을 영리 목적으로 이용할 수 없습니다.



동일조건변경허락. 귀하가 이 저작물을 개작, 변형 또는 가공했을 경우에는, 이 저작물과 동일한 이용허락조건하에서만 배포할 수 있습니다.

- 귀하는, 이 저작물의 재이용이나 배포의 경우, 이 저작물에 적용된 이용허락조건을 명확하게 나타내어야 합니다.
- 저작권자로부터 별도의 허가를 받으면 이러한 조건들은 적용되지 않습니다.

저작권법에 따른 이용자의 권리는 위의 내용에 의하여 영향을 받지 않습니다.

이것은 [이용허락규약\(Legal Code\)](#)을 이해하기 쉽게 요약한 것입니다.

[Disclaimer](#)

공학박사 학위논문

**Performance Enhancement of
Electronic and Optoelectronic Devices
by Interfacial Layer Engineering**

**계면제어기술을 통한 전자 및 광전자 소자의
성능 향상**

2016 년 2 월

서울대학교 대학원

기계항공공학부

성 향 기

계면제어기술을 통한 전자 및 광전자 소자의 성능 향상

Performance Enhancement of Electronic and
Optoelectronic Devices by Interfacial Layer Engineering

지도교수 최 만 수

이 논문을 공학박사 학위논문으로 제출함
2015 년 11 월

서울대학교 대학원
기계항공공학부
성 향 기

성향기의 공학박사 학위논문을 인준함
2015 년 12 월

위원장	이 준 식	(인)
부위원장	최 만 수	(인)
위원	권 누리	(인)
위원	고 승 훈	(인)
위원	정 훈 석	(인)

Performance Enhancement of Electronic and Optoelectronic Devices by Interfacial Layer Engineering

Hyangki Sung

School of Mechanical and Aerospace Engineering

The Graduate School

Seoul National University

Abstract

Selection of an appropriate interfacial layer is a requirement to achieve high-performing electronic and optoelectronic devices. In particular, the performance of these devices is closely related to the transport of charge carriers, and thus can be improved by controlling the electrical property of interfacial layers with hole or electron doping. In recent years, organic materials and graphene have attracted great research interest for their potential applications in the next-generation devices such as flexible and transparent electronics. However, they can be easily damaged by established processes of doping which typically involves high energy impact, due to their small dissociation energies, and, especially, organic materials are vulnerable to chemicals. Therefore, experimental methods for controlling their electrical properties through doping to enhance device performance are limited. This dissertation aims to improve performance of devices based on organic

materials and graphene, such as an organic light-emitting diode (OLED), a graphene field-effect transistor (FET), and a graphene perovskite solar cell by interfacial layer engineering.

First, gold nanoparticles (Au NPs) have been precisely positioned in a specific plane in a fluorescent Alq₃-based OLED, and showed that there exist an optimum distance between the NP layer and the emitting layer for the maximum external quantum efficiency of the device. Au NPs are positioned in the hole transport layer (HTL) using a dry, room temperature aerosol technique. By controlling the position and the density of the Au NPs, the external quantum efficiency of the Au-NP-embedded OLEDs can be optimized, presenting a 38% enhanced maximum efficiency compared to that of the control device without Au NPs. In contrast to typically used methods for incorporating metal NPs in an organic layer, such as vacuum thermal evaporation or spin coating, the aerosol-deposited Au NPs do not penetrate into the underlying organic layer, not only allowing for precise control of their vertical position, but also minimizing damage to the hole transport organic material. Optical and electrical characterizations show that the existence of the optimum distance results from the competition between the metal induced quenching and the increased electron–hole recombination probability arising from electrostatic effects of holes trapped in the Au NPs.

Secondly, reliable control of doping type and doping level of graphene has been realized by controlled deposition of aerosol-derived metal NPs on the channel of a graphene FET. Ag or Pt NPs with a fairly narrow size distribution are deposited on graphene channels using an aerosol technique that is capable of controlling size, shape, and deposited density of NPs

independently. The transfer characteristics of the aerosol NP-decorated graphene FETs show that deposition of the Ag NPs and the Pt NPs induces a shift of the Dirac point in the negative and positive direction, respectively, indicating n-type and p-type doping of graphene, respectively. The change in doping level and doping type of graphene is attributed to the electron transfer between the metal NPs and graphene owing to the work function difference. Due to the consistent size and shape of the aerosol-derived metal NPs, doping level shows a monotonic change with increasing the surface coverage of the NPs, which has been hardly achieved with typically used methods such as thermal evaporation and spin coating due to morphology change and random aggregation of metal NPs. The minimum conductance at the Dirac point also shows no appreciable change with deposition of the aerosol NPs on graphene, implying that the aerosol NPs delivered on graphene by weak electrostatic force do not degrade the graphene sp^2 hybridization during their deposition.

Thirdly, highly efficient transparent conductive oxide (TCO)-free inverted perovskite solar cells have been fabricated by employing graphene as a transparent anode. The interface between the graphene electrode and the HTL, poly (3, 4-ethylenedioxythiophene):poly (styrenesulfonate) (PEDOT:PSS), has been engineered by introducing a few nanometer thick molybdenum trioxide (MoO_3) layer to improve hydrophilicity and increase the work function of graphene. With a 2 nm-thick MoO_3 layer, the graphene-based perovskite solar cells show the best PCE of 17.1% and the average PCE of 16.1% under AM 1.5G one sun illumination (100 mW cm^{-2}), which is so far the highest efficiency for TCO-free solar cells. Interestingly, the

interface engineering using MoO₃ also enhances the performance of the ITO-based devices, resulting in the best PCE of 18.8% and the average PCE of 18.2%, which is also the highest efficiency for inverted perovskite solar cells.

Keywords: Nanoparticles, aerosols, graphene, electronic devices, optoelectronic devices, organic light-emitting diodes, graphene field-effect transistors, graphene perovskite solar cells

Student Number: 2010-20686

Contents

Abstract	i
Contents	v
List of Tables	ix
Nomenclature	x
List of Figures	xiv
Chapter 1. Introduction	1
1.1. Research Background	2
1.2. Research Objectives	5
1.3. Thesis Outline	7
1.4. References	8
Chapter 2. Aerosols, Graphene, and Electronic/ Optoelectronic Devices	13
2.1. Aerosol Nanoparticles	14
2.1.1. Definition of Aerosols	14
2.1.2. Measurement of Size Distribution of Nanoparticles	14
2.2. Generation of Nanoparticles via Spark Discharge	16
2.3. Graphene	20
2.3.1. Electronic Properties	21
2.3.2. Optical Properties	23
2.3.3. Raman Spectroscopy of Graphene	25
2.4. Doping of Graphene	27

2.5.	Electronic Devices: Graphene Field-Effect Transistors...	29
2.6.	Optoelectronic Devices I: Organic Light-Emitting Diodes	32
2.6.1.	Structure and Light-Emitting Mechanism	32
2.6.2.	Fluorescence	34
2.6.3.	Measuring the Efficiency of OLEDs	35
2.6.4.	Interaction between Fluorophores and Adjacent Metal Particles	38
2.7.	Optoelectronic Devices II: Perovskite-Based Solar Cells	42
2.7.1.	Perovskite: Structure and Properties	42
2.7.2.	Perovskite Application in Photovoltaic Devices.....	44
2.8.	References	45
Chapter 3. Performance Enhancement of Organic Light-Emitting Diodes by Position-Controlled Incorporation of Nanoparticles.....		57
3.1.	Introduction	58
3.2.	Experimental Methods	60
3.2.1.	Fabrication of Gold Nanoparticle-Embedded OLEDs.....	60
3.2.2.	Characterization.....	64
3.3.	Results and Discussion	66
3.3.1.	Characteristics of Gold Nanoparticle Layers	66
3.3.2.	Device Characteristics of Gold Nanoparticle-Embedded OLEDs	66
3.3.3.	Photoluminescence Analysis	73
3.3.4.	Charge Transport Analysis	75

3.4.	Conclusion	80
3.5.	References	81
Chapter 4. Reliable Control of Doping Type and Doping Level of Graphene by Aerosol-Derived Metal Nanoparticles.....		85
4.1.	Introduction	86
4.2.	Experimental Methods	88
4.2.1.	Fabrication of Graphene Field-Effect Transistors	88
4.2.2.	Metal Nanoparticles Deposition Employing an Aerosol Technique.....	88
4.3.	Characterization	91
4.4.	Results and Discussion	92
4.4.1.	Characteristics of Metal Nanoparticle Layers.....	92
4.4.2.	Controlled Electrical Transport Properties of Graphene by Doping.....	93
4.5.	Conclusion	102
4.6.	References	103
Chapter 5. High-Efficiency Transparent Conductive Oxide-Free Solar Cells with Metal Oxide-Modified Graphene Anode		107
5.1.	Introduction	108
5.2.	Experimental Methods	110
5.2.1.	Fabrication of Graphene-Based Perovskite Solar Cells..	110
5.2.2.	Characterization.....	113
5.3.	Results and Discussion	114

5.3.1.	Device Structure	114
5.3.2.	Wetting Issue of PEDOT:PSS on Graphene Surfaces	115
5.3.3.	Device Characteristics	119
5.3.4.	Analysis on Electrical and Optical Properties	123
5.3.5.	Analysis on the Open-Circuit Voltage Difference.....	125
5.4.	Conclusion	133
5.5.	References	134
Chapter 6. Concluding Remarks.....		141
Acknowledgement.....		145
Abstract (in Korean).....		146
List of Publications		149
Conferences		150

List of Tables

Table 2.1 Properties of Graphene	21
Table 5.1 Photovoltaic parameters of the graphene- and ITO-based devices with MoO ₃ layers of varying thickness	119

Nomenclature

a	lattice constant	[m]
a_{CC}	carbon-carbon bonding length	[m]
c	light speed	$[3.0 \times 10^8 \text{ m s}^{-1}]$
C_c	Cunningham correction factor	
C_A	absorption cross section	[cm ²]
C_E	extinction cross section	[cm ²]
C_S	scattering cross section	[cm ²]
C_G	gate capacitance per unit area	[F cm ⁻²]
d	distance of nanoparticle layer away from emissive layer	[nm]
d_p	particle diameter	[m]
e	elementary charge	$[1.602 \times 10^{-19} \text{ C}]$
E	energy of electrons	[eV]
E_T	efficiency of energy transfer	
G	optical conductivity	[S m ⁻¹]
h	Planck's constant	$[4.136 \times 10^{-15} \text{ eV s}]$
I	electrical current	[A]
I_F	emission intensity due to fluorophore	[a.u.]
I_P	emission intensity due to radiating plasmon	[a.u.]
I_T	total emission intensity	[a.u.]
J	electrical current density	[A m ⁻²]
J_{sc}	short-circuit current density	[mA cm ⁻²]

k	wave vector	$[\text{m}^{-1}]$
K_m	constant to convert from radiant to luminous scales	$[683 \text{ lm W}^{-1}]$
k_{nr}	nonradiative decay rate in the absence of acceptors	$[\text{s}^{-1}]$
k_r	intrinsic radiative decay rate	$[\text{s}^{-1}]$
k_T	energy transfer rate	$[\text{s}^{-1}]$
l	luminous intensity	$[\text{cd}]$
l_0	maximum luminous intensity	$[\text{cd}]$
L	luminance	$[\text{cd m}^{-2}]$
L	length of nano-DMA	$[\text{m}]$
N	surface coverage density of nanoparticle layer	$[\mu\text{m}^{-2}]$
n	number of elementary charge	
Δn	net carrier concentration	$[\text{cm}^{-2}]$
P_{OLED}	radiant flux emitted by device	$[\text{W}]$
Q_0	quantum yield in the absence of acceptors	
Q_A	efficiencies of absorption	
Q_E	efficiencies of extinction	
Q_S	efficiencies of scattering	
Q_{sh}	sheath flow rate	$[\text{m}^3 \text{ s}^{-1}]$
r	particle radius	$[\text{cm}]$
R	distance from fluorophore to acceptor	$[\text{nm}]$
R_0	Forster distance	$[\text{nm}]$
r_1	inner radius of nano-DMA	$[\text{m}]$

r_2	outer radius of nano-DMA	[m]
S	emission area	[m ²]
t	nearest-neighbor hopping energy	[eV]
v	impinging velocity of nanoparticle	[m s ⁻¹]
v_F	Fermi velocity in graphene	[m s ⁻¹]
V	voltage bias	[V]
$V(\lambda)$	photo-optical response normalized with respect to the human eye	
V_{oc}	out-circuit voltage	[V]
V_{TE}	terminal electrical velocity	[m s ⁻¹]
ΔV_{Dirac}	shift of the Dirac point	[V]
Z_p	electrical mobility	[m ² V ⁻¹ s ⁻¹]
α	polarizability of the particle	[cm ³]
γ	electron–hole charge balance factor	
ε	complex dielectric constant	
ε_F	absorption coefficient of fluorophore	
\mathcal{E}	electric field	[V m ⁻¹]
η_{ext}	external quantum efficiency	
η_L	luminous (or current) efficiency	
η_{out}	out-coupling efficiency	
η_{int}	internal quantum efficiency	
η_P	luminous power efficiency	[lm W ⁻¹]
θ	emission angle	[°]

λ	gas mean free path	[m]
μ	viscosity of gas	[N s m ⁻²]
τ_0	lifetime of donor in the absence of acceptors	[s]
φ	intrinsic quantum efficiency	
φ_S	fraction of the light to be scattered	
Φ_{total}	total luminous flux	[lm]
χ	fraction of excitons that decay radiatively	

List of Figures

Figure 2.1 Schematics of the spark discharge generators with (a) a pin-to-plate configuration and (b) a rod-to-rod configuration.[13].	18
Figure 2.2 Schematic of an electric circuit connected to the electrode of the SDG to control spark generation.[13].	18
Figure 2.3 (a), (b) TEM images of the Ag nanoparticles generated by (a) pin-to-plate type SDG and (b) rod-to-rod type SDG. (c) Size distribution of the silver nanoparticles extracted from the TEM images based on the projected area equivalent diameter.[13]	20
Figure 2.4 Schematics of graphene's crystal structure, Brillouin zone and dispersion spectrum.[19]	23
Figure 2.5 (a) Photograph of a 50- μm aperture partially covered with graphene and its bilayer. The line profile shows the intensity of the transmitted light along the yellow line. (b) Transmittance spectrum of single layer graphene (open circles). The red line is the transmittance $T = (1+1/2\pi\alpha)^{-2}$ expected for Dirac fermions in graphene, while the green line considers a nonlinearity and triangular warping of graphene's electronic spectrum. (Inset) The relation of transmittance and the number of graphene layer. The dashed lines indicate an intensity reduction by $\pi\alpha$ with each added layer.[28]	24
Figure 2.6 (a) Optical microscope image of a flake composed of different number (N) of graphene layers and (b) the corresponding Raman spectrum.[33] (c) The 2D peaks measured on single- and bi-layer	

graphene and graphite.[34].....	26
Figure 2.7 Scheme of the relative position of the highest occupied molecular orbitals (HOMO) and the lowest unoccupied molecular orbitals (LUMO) of an adsorbate to the Fermi level of graphene for (a) p-type and (b) n-type dopant.[45]	29
Figure 2.8 The traditional Si-based FETs formed on SiO ₂ substrates [46].	30
Figure 2.9 (a) AFM scan of top-gated transistor fabricated using epitaxial graphene on SiC as the active material. (b) $I_d - V_d$ characteristics of the device for two drain voltages showing typical V shape transfer characteristics for graphene transistors; current flows for both positive and negative top-gate voltages.[51]	31
Figure 2.10 Light emitting mechanism of an OLED device	33
Figure 2.11. Jablonski diagram for absorption, fluorescence, and phosphorescence.	35
Figure 2.12 Effect of the particle size on the scattering efficiency Q_s and the light-scattering yield (ϕ_s) of gold and silver colloids. Data from [71].	42
Figure 2.13 Crystal structure of CH ₃ NH ₃ PbI ₃	43
Figure 3.1 Schematic structure of the Au-NP-embedded OLED, where Au NPs in the hole transport layer composed of NPB is positioned d away from the Alq ₃ -NPB interface.	61
Figure 3.2 (a) Schematic illustration of the experimental setup to fabricate Au-NP-embedded OLEDs consisting of a conventional vacuum thermal evaporator and a homemade SDG-ESP system. (b) Electric circuit used to control spark discharge in the SDG.....	62

Figure 3.3 (a) The size distribution of Au NPs generated in the spark discharge generator, which was obtained by analyzing HRTEM images. The geometric mean diameter and standard deviation of the Au NPs were found to be 4.0 and 1.5 nm, respectively. (b) - (e) The SEM images of the Au NPs deposited on ITO substrates by the homemade aerosol deposition system shown in Figure 3.1. The particle density corresponds to (b) 200, (c) 920, (d) 5150, and (e) 8400 μm^{-2} on average.67

Figure 3.4 (a) Current density vs. voltage characteristics of the SDG OLEDs with different d 's ($d = 10, 20, 30$ or 40 nm), and the VTE OLED ("thickness" = 3.0 \AA , deposition rate = 0.2 \AA/s) with $d = 20$ nm. (b) External quantum efficiency vs. current density characteristics of the devices shown in (a).69

Figure 3.5 (a) Luminous power efficiency vs. current density characteristics of the SDG OLEDs ($N \approx 5150 \mu\text{m}^{-2}$) with different d 's ($d = 10, 20, 30$ or 40 nm), and the VTE OLED ($N \approx 36000 \mu\text{m}^{-2}$, "thickness" = 3.0 \AA , deposition rate = 0.2 \AA/s) with $d = 20$ nm.69

Figure 3.6 Cross-sectional TEM images of (a) the SDG OLED and (b) the VTE OLED structures, both with $d = 20$ nm, deposited on Si substrates. For the VTE OLED, the "thickness" and the deposition rate of the Au layer are 3.0 \AA and 0.2 \AA/s , respectively. (c) and (d) are STEM images of the same samples in (a) and (b), respectively. In (b), small Au NPs marked by black arrows were formed at $d > 20$ nm, indicating that thermally evaporated Au atoms have penetrated into the underlying NPB, which is more clearly shown in (d).71

Figure 3.7 (a) Photoluminescence spectra and (b) transient

photoluminescence decay profiles of the samples whose structures were identical to the SDG OLEDs with different d 's ($d = 10, 20, 30$ or 40 nm), except that the 50-nm-thick Alq₃ layer in the SDG OLEDs was replaced with a bilayer of 5-nm-thick Alq₃ (on the NPB side) and 45-nm-thick NPB (on the Al side). In (a) and (b), the excitation wavelength was 430 nm, while the photoluminescence decay profiles were detected at 600 nm.75

Figure 3.8 (a) Plots of η_{ext} , η_{out} , ϕ , and γ normalized to the corresponding values of the control device as functions of d . (b) Current density vs. voltage characteristics of hole-only devices comprising: glass / ITO / 100 nm NPB / 100 nm Al, where Au NPs were embedded in the NPB layer using the SDG-ESP system. The distance between the Au NP layer and the ITO–NPB interface, d_{ITO} , was chosen to be the same as that in the SDG OLEDs ($d_{\text{ITO}} = 10, 20, 30$, or 40 nm).77

Figure 3.9 Schematic energy-level diagrams. (a) Control device without Au NPs, (b) SDG OLED with $d = 40$ nm. The reduced electric field at the anode due to trapped holes in the Au NPs decreases the hole current, leading to an increased probability of exciton formation. (c) SDG OLED with $d = 10$ nm. As the Au NPs are located closer to the Alq₃–NPB interface, the electrostatic field in the Alq₃ near that interface increases, resulting into a further increase in the exciton formation probability.79

Figure 4.1 (a) Schematic of metal NP-deposited graphene FET fabricated on SiO₂/Si substrate. The electrical contacts are indicated as source, drain, and gate. (b) Raman spectrum (514 nm excitation) of a monolayer

graphene film transferred on a SiO ₂ /Si substrate. The inset shows a top view image of graphene channel and source/drain electrodes from an optical microscope.	89
Figure 4.2 (a) Schematic diagram of spark discharge generator consisting of a pin and a plate electrode in a cylindrical chamber for controlling the metal NP generation, equipped with (b) an electrostatic precipitator system composed of a bottom electrode in a grounded cylindrical chamber for regulating the amount of carrier gas.	90
Figure 4.3 Size distribution of aerosol-derived Ag and Pt NPs measured by SMPS system. Geometrical mean diameters of Ag and Pt NPs are 7.5 and 6.4 nm, respectively, and the size of Ag NPs is distributed slightly broader than that of Pt NPs.	92
Figure 4.4 FESEM images of the graphene channel deposited with different surface densities of Ag NPs from (a) 12% to (b) 21% and Pt NPs from (c) 24% to (d) 32%, revealing uniformly distributed NPs with consistent size and shape. The scale bars in the images are 100 nm, and the insets represent 2-fold enlarged images.	93
Figure 4.5 Transfer characteristics of graphene FETs with and without (a) Ag NP deposition and (b) Pt NP deposition. Ag NPs on graphene cause a shift in the Dirac point into the negative gate bias direction, while Pt NPs cause a shift into the positive gate bias direction.	95
Figure 4.6 Carrier density per unit area of graphene as a function of (a) the surface coverage or (b) the inter-particle spacing for Ag and Pt NPs: the open squares and the closed black circles correspond to Ag and Pt NPs deposited on graphene, respectively, while the solid lines are the fit	

curves.	97
Figure 4.7 Schematic energy band diagrams of graphenes before and after (a) Ag NPs doping with different density of 12, 16, 18, and 21%, and (b) Pt NPs doping with 24, 26, 29 and 32%.....	98
Figure 5.1 Raman spectrum of the as-prepared graphene transferred on a SiO ₂ /Si substrate.....	111
Figure 5.2 Schematic structure of the inverted MAPbI ₃ perovskite solar cells utilizing graphene as a transparent anode.....	114
Figure 5.3 Droplets of PEDOT:PSS on (a) as-prepared graphene, (b) graphene covered with 1 nm MoO ₃ , (c) graphene covered with 2 nm MoO ₃ , (d) as-prepared ITO, (e) UVO-treated ITO, and (f) ITO covered with 1 nm MoO ₃ after UVO treatment. Enhanced wetting of PEDOT:PSS on both graphene and ITO surfaces was observed after thermal deposition of the MoO ₃ layers. The insets in (a) – (c) show the optical images of PEDOT:PSS/MAPbI ₃ films fabricated on the corresponding glass/graphene surfaces. The MoO ₃ layers were pre-formed in a square shape at the center of the substrates before spin-coating those PEDOT:PSS/MAPbI ₃ films.....	116
Figure 5.4 Plan-view SEM images of (a) as-prepared graphene, (b) graphene/1 nm MoO ₃ and (c) graphene/2 nm MoO ₃ (scale bar, 100 nm). The MoO ₃ layers were deposited by thermal evaporation with deposition rate of 0.1 Å s ⁻¹ , followed by 150 °C annealing for 10 min.	117
Figure 5.5 Cross-sectional SEM images of the devices employing (a) graphene/2 nm MoO ₃ electrode and (b) ITO/1 nm MoO ₃ electrode	

measured in SE mode (left) and BSE mode (right).....	118
Figure 5.6 (a), (b) Relationship between average PCE and MoO ₃ thickness for (a) graphene electrodes and (b) ITO electrodes. (c), (d) $J-V$ curves for best-performing (c) G-M2 and (d) ITO-M1 devices under AM 1.5G illumination at 100 mW cm ⁻² measured via reverse (blue) and forward (black) bias sweep.....	120
Figure 5.7 $J-V$ curves of (a) G-M1 and (b) G-M2 devices under AM 1.5G illumination at 100 mW cm ⁻² . Non-consistent $J-V$ characteristics appeared in G-M1 devices due to incomplete covering of 1 nm-thick MoO ₃ layers over hydrophobic graphene surfaces, resulting in nonuniform formation of PEDOT:PSS and MAPbI ₃ films.	121
Figure 5.8 PCE Histogram of 10 devices for each electrode type, G-M2 and ITO-M1.	123
Figure 5.9 (a) Relationship between sheet resistance and MoO ₃ thickness for graphene and ITO. (b) Transmittance of graphene and ITO with/without 2 nm-thick MoO ₃ layers.	124
Figure 5.10 EQE spectra (black lines) and integrated J_{sc} (blue lines) of best-performing (a) G-M2 and (b) ITO-M1 devices. The integrated photocurrents were calculated as 20.2 and 21.0 mA cm ⁻² , respectively.....	125
Figure 5.11 Transmittance of glass/graphene and glass/ITO with/without 2 nm-thick MoO ₃ layers, and a bare glass substrate.....	125
Figure 5.12 (a), (b) UPS spectra and calculated work functions of (a) ITO and (b) graphene with MoO ₃ layers of varying thickness. (c) Schematic energy level diagram of the fabricated inverted structure. The energy	

levels are taken from Jeng et al.[39] The work function of as-prepared graphene (denoted by black dashed line, 4.23 eV) was increased to 4.71 eV by MoO₃ doping (denoted by blue solid line).....127

Figure 5.13 AFM topography images (3 μm × 3 μm) of (a) as-prepared graphene, (b) graphene/2 nm MoO₃, (c) graphene/2 nm MoO₃ after spin-coating of PEDOT:PSS, (d) as-prepared ITO, (e) ITO/1 nm MoO₃, (f) ITO/1 nm MoO₃ after spin-coating of PEDOT:PSS. The calculated surface rms roughness values were presented in each figure.....129

Figure 5.14 Plan-view SEM images of the MAPbI₃ perovskite films fabricated on (a) G-M2/PEDOT:PSS and (b) ITO-M1/PEDOT:PSS surfaces. (c) and (d) are the higher magnification images of (a) and (b), respectively.....131

Figure 5.15 X-ray diffraction patterns of G-M2/PEDOT:PSS/MAPbI₃ and ITO-M1/PEDOT:PSS/MAPbI₃. Peaks for perovskite films were observed identically in the X-ray diffraction patterns for both G-M2 and ITO-M1 samples although all the peaks were not seen clearly for the G-M2 sample due to the large difference in intensity among them. It is noticeable that the (110) and (220) peak intensities of the G-M2 sample is much stronger than those of the ITO-M1 sample, which implies that the MAPbI₃ film was formed with better alignment of the grain orientation on the smoother graphene surface than on the relatively rough ITO surface.132

Chapter 1.

Introduction

1.1. Research Background

Nanotechnology has led to a wide range of new materials, devices, and systems in a variety of fields including energy storage, energy harvesting, medicine, sensing, and electronics since the base concept of nanotechnology was firstly addressed by the physicist Richard Feynman in his lecture “There’s plenty of room at the bottom”[1] in 1959. Nanotechnology is the manipulation and manufacture of materials and devices at extremely small scaled ranging from 1 – 100 nm. At these dimensions, materials possess unique physical and chemical properties [2], which has triggered tremendous breakthroughs in the related technologies.

In electronic and optoelectronic devices, energy-level engineering of nanometer-scale thick composing layers alters the transport characteristics of charge carriers, and thus the interfaces between layers play an significant role in device performance.[3]

In the first place, metal nanoparticles (NPs) have been used in electronic and optoelectronic devices to modify interfacial layers for enhanced performances [4-8] because metal NPs present unique optical, electronic, or chemical properties that can be tuned by controlling their size, shape and composition.[9] In the case of metal NP-enhanced electronic devices, especially graphene-based FETs, a metal layer adsorbed on graphene is theoretically predicted to induce p- or n-type doping depending on the work function difference between the metal and graphene.[10] Recently, several demonstrations on doping control of graphene by thermally evaporated thin

metal films have been reported.[11,12] However, the surface morphology of this metal layer changed with its deposition thickness, and thus graphene-metal equilibrium separation was hardly controlled. For example, the isolated Al NPs formed by thermally depositing Al thin metal film with effective thickness of 0.5 nm showed large contact area with graphene to provide proper doping effect, whereas Al NPs formed with effective thickness of 1.0 nm started to coalesce towards continuous film turning the graphene into a metal.[13] Another investigation reported that the configuration of Au layer caused a change of doping type: n-type for Au NPs and p-type for Au thin film.[14] These results can be explained by the interplay between the electron transfer induced by work-function difference and the potential variation by change of surface morphology induced by chemical interaction.[14] Meanwhile, metal NPs formed on graphene by solution process have tended to form aggregates with spatially non-uniform distribution.[15] Thus, common methods for forming metal NP layers such as thermal evaporation or spin-coating of metal NP dispersion are lacking in modulating carrier doping of graphene in precisely controlled manner.

In the case of optoelectronic devices such as surface-plasmon-enhanced light-emitting devices [5,6] and solar cells,[7,8] close proximity between metal NPs and photoactive materials is required to facilitate light-matter interactions. However, in respect of weakly bonded organic solids, they can be easily damaged or degraded by exposure to a wet chemical or a high temperature process. For this reason, incorporation of metal NPs in the interior of an organic devices is limited. In some metal NP-enhanced organic devices, particularly those made of small molecules, metal NPs have been

fabricated on the bottom electrode prior to depositing organic layers.[6] Thermal evaporation has been used to form nano-sized metal islands on an organic surface followed by further organic deposition, and thus to fabricate metal NP-embedded organic devices.[16] In this case, however, the particle size and number density cannot be controlled, and the evaporated, energetic metal atoms may damage the underlying organic materials.

In the second place, an ultra-thin layer with a few nanometer thickness can play an important role as an effective interfacial layer by forming a preferable energy level alignment. In particular, in the field of organic photovoltaics, there have been lots of studies on bendable conducting electrodes to replace brittle TCOs for flexible solar cell applications, such as graphene,[17-20] carbon nanotubes,[21-23] metal grids,[24-26] and conductive polymers.[27,28] Among them, graphene, a single layer of carbon atoms bonded in a hexagonal lattice, seems to be the most promising substitute for TCO electrodes given its high transparency (about 97% in visible range), mechanical robustness, flexibility and stretchability. For efficient solar cell operation, the work function of the anode should be well aligned with the HOMO level of the HTL. However, graphene's work function of ~ 4.3 eV is highly mismatched with the HOMO level of commonly used HTL such as PEDOT:PSS (~ 5.2 eV). In order to increase the work function of graphene and to improve the PCE of a graphene-based OPV, thin interfacial layers such as metal oxide,[18] organic self-assembled monolayer,[29] and metal NPs[30] have been applied between the graphene anode and the PEDOT:PSS layer.

1.2. Research Objectives

This dissertation aims to improve the performance of electronic and optoelectronic devices by controlling the properties of interfacial layers. The devices investigated are classified into three types: an OLED, a graphene FET, and a graphene-based perovskite solar cell.

Firstly, to improve the efficiency of an OLED, a monolayer of Au NPs has been introduced in a specific plane in the HTL using an aerosol technique. To achieve a high efficiency OLED, it is necessary to balance the numbers of injected holes and electrons into the emissive layer. This aerosol technique adopts dry and room temperature processes, and thus it is capable of locating Au NPs with a precise control of the vertical (perpendicular to the substrate surface) position within the HTL, while minimizing possible damage to the underlying layer. This study aims to investigate the effect of the position of Au NPs away from the emissive layer on the electrical and optical properties of an OLED. Furthermore, this aims to show the existence of the optimal position of a metal NP layer in an OLED for largest EQE enhancement.

Secondly, to achieve a reliable control in doping and carrier concentration of graphene, a monolayer of Ag or Pt NPs has been formed on graphene using an aerosol technique. When a conventional thermal evaporation method is used, not only the particle size grows with deposition thickness showing changes in morphology, but also the surface coverage density cannot be controlled. However, the aerosol method has enabled to fabricate a monodisperse NP layer with desired size and surface coverage density by

controlling them independently. This study aims to show a reliable doping control of graphene using the aerosol-derived metal NPs. This study also aims to investigate the effect of the graphene's doping type and doping concentration controlled with aerosol metal NPs on the transport characteristics of a graphene FET.

Lastly, to realize a high efficiency TCO-free solar cell, graphene anode has been utilized with an ultra-thin MoO₃ layer as an interfacial layer. TCO-free OPV devices with graphene anode have already been successfully demonstrated reaching a PCE of 8.48%, the highest PCE among the TCO-free tandem polymer solar cells,[20] although still lower than the highest PCE of 11.0% of the TCO-free perovskite solar cells.[31] Graphene is considered as one of the most effective alternatives to the conventional TCO electrodes such as indium tin oxide (ITO) and fluorine-doped tin oxide (FTO). This study aims to demonstrate a high efficiency TCO-free solar cell using graphene as an anode and perovskite as an absorber. In addition, this study aims to investigate the role of a few nanometer-thick MoO₃ as an interfacial layer between graphene and a PEDOT:PSS HTL for the use of graphene as an effective anode electrode.

1.3. Thesis Outline

This thesis is organized into six chapters. Following this Chapter 1 on Introduction, Chapter 2 describes some basic knowledge about aerosols, spark discharge for generating aerosol nanoparticles, graphene, and electronic and optoelectronic devices such as a graphene FET, an OLED and a perovskite-based solar cell.

Chapter 3 and Chapter 4 deal with the enhanced performance of devices by means of aerosol nanoparticles. Chapter 3 focuses on a metal-nanoparticle enhanced OLED, and investigates the effect of the position of the metal nanoparticle layer on the performance enhancement of OLEDs. Chapter 4 examines control of doping type and doping level of graphene with metal nanoparticles by an aerosol technique, which is studied by graphene FET measurements.

Chapter 5 is devoted to a high-efficiency transparent conductive oxide-free solar cell using graphene as a transparent anode and perovskite as an absorber, and investigates how the thickness of an interfacial layer influences on the device performance.

Finally, Chapter 6 summarizes the research work presented in this thesis, with emphasis on the major results and conclusions, and suggests further research work related to this topic.

1.4. References

- [1] R.P. Feynman, "There's plenty of room at the bottom", *Engineering and science*, **23**, 22-36 (1960)
- [2] J. Osuwa, P. Anusionwu, "Some advances and prospects in nanotechnology: a review", *Asian J Inf Technol*, **10**, 96-100 (2011)
- [3] S.-S. Sun, L.R. Dalton, "Introduction to organic electronic and optoelectronic materials and devices"(2008), *CRC Press*,
- [4] K.R. Catchpole, S. Pillai, "Surface plasmons for enhanced silicon light-emitting diodes and solar cells", *J. Lumin.*, **121**, 315-318 (2006)
- [5] M.-K. Kwon, J.-Y. Kim, B.-H. Kim, I.-K. Park, C.-Y. Cho, C.C. Byeon, S.-J. Park, "Surface-plasmon-enhanced light-emitting diodes", *Adv. Mater.*, **20**, 1253-1257 (2008)
- [6] A. Fujiki, T. Uemura, N. Zettsu, M. Akai-Kasaya, A. Saito, Y. Kuwahara, "Enhanced fluorescence by surface plasmon coupling of Au nanoparticles in an organic electroluminescence diode", *Appl. Phys. Lett.*, **96**, (2010)
- [7] D. Derkacs, S.H. Lim, P. Matheu, W. Mar, E.T. Yu, "Improved performance of amorphous silicon solar cells via scattering from surface plasmon polaritons in nearby metallic nanoparticles", *Appl. Phys. Lett.*, **89**, 093103-093103 (2006)
- [8] F.-C. Chen, J.-L. Wu, C.-L. Lee, Y. Hong, C.-H. Kuo, M.H. Huang, "Plasmonic-enhanced polymer photovoltaic devices incorporating solution-processable metal nanoparticles", *Appl. Phys. Lett.*, **95**, 013305 (2009)

- [9] M.-C. Daniel, D. Astruc, "Gold nanoparticles: assembly, supramolecular chemistry, quantum-size-related properties, and applications toward biology, catalysis, and nanotechnology", *Chem. Rev.*, **104**, 293-346 (2003)
- [10] G. Giovannetti, P.A. Khomyakov, G. Brocks, V.M. Karpan, J. van den Brink, P.J. Kelly, "Doping graphene with metal contacts", *Phys. Rev. Lett.*, **101**, (2008)
- [11] J. Lee, K.S. Novoselov, H.S. Shin, "Interaction between metal and graphene: dependence on the layer number of graphene", *ACS Nano*, **5**, 608-612 (2011)
- [12] Y. Ren, S. Chen, W. Cai, Y. Zhu, C. Zhu, R.S. Ruoff, "Controlling the electrical transport properties of graphene by in situ metal deposition", *Appl. Phys. Lett.*, **97**, 053107 (2010)
- [13] X. Shi, G. Dong, M. Fang, F. Wang, H. Lin, W.-C. Yen, K.S. Chan, Y.-L. Chueh, J.C. Ho, "Selective n-type doping in graphene via the aluminium nanoparticle decoration approach", *J. Mater. Chem. A*, **2**, 5417 (2014)
- [14] Y. Wu, W. Jiang, Y. Ren, W. Cai, W.H. Lee, H. Li, R.D. Piner, C.W. Pope, Y. Hao, H. Ji, J. Kang, R.S. Ruoff, "Tuning the doping type and level of graphene with different gold configurations", *Small*, **8**, 3129-3136 (2012)
- [15] R. Muszynski, B. Seger, P.V. Kamat, "Decorating graphene sheets with gold nanoparticles", *The Journal of Physical Chemistry C*, **112**, 5263-5266 (2008)
- [16] B.P. Rand, P. Peumans, S.R. Forrest, "Long-range absorption enhancement in organic tandem thin-film solar cells containing silver

- nanoclusters", *J. Appl. Phys.*, **96**, 7519-7526 (2004)
- [17] J. Wu, H.A. Becerril, Z. Bao, Z. Liu, Y. Chen, P. Peumans, "Organic solar cells with solution-processed graphene transparent electrodes", *Appl. Phys. Lett.*, **92**, 263302 (2008)
- [18] Y. Wang, S.W. Tong, X.F. Xu, B. Özyilmaz, K.P. Loh, "Interface engineering of layer-by-layer stacked graphene anodes for high-performance organic solar cells", *Adv. Mater.*, **23**, 1514-1518 (2011)
- [19] H. Park, S. Chang, X. Zhou, J. Kong, T. Palacios, S. Gradecak, "Flexible graphene electrode-based organic photovoltaics with record-high efficiency", *Nano Lett.*, **14**, 5148-5154 (2014)
- [20] A.R.b. Mohd Yusoff, D. Kim, F.K. Schneider, W.J. da Silva, J. Jang, "Au-doped single layer graphene nanoribbons for a record-high efficiency ITO-free tandem polymer solar cell", *Energy Environ. Sci.*, **8**, 1523-1537 (2015)
- [21] M.W. Rowell, M.A. Topinka, M.D. McGehee, H.-J. Prall, G. Dennler, N.S. Sariciftci, L. Hu, G. Gruner, "Organic solar cells with carbon nanotube network electrodes", *Appl. Phys. Lett.*, **88**, 233506 (2006)
- [22] I. Jeon, K. Cui, T. Chiba, A. Anisimov, A.G. Nasibulin, E.I. Kauppinen, S. Maruyama, Y. Matsuo, "Direct and dry deposited single-walled carbon nanotube films doped with MoOx as electron-blocking transparent electrodes for flexible organic solar cells", *J. Am. Chem. Soc.*, **137**, 7982-7985 (2015)
- [23] R.V. Salvatierra, C.E. Cava, L.S. Roman, A.J.G. Zarbin, "ITO-free and flexible organic photovoltaic device based on high transparent and conductive polyaniline/carbon nanotube thin films", *Adv. Funct. Mater.*, **23**,

1490-1499 (2013)

[24] B. Muhsin, R. Roesch, G. Gobsch, H. Hoppe, "Flexible ITO-free polymer solar cells based on highly conductive PEDOT:PSS and a printed silver grid", *Sol. Energy Mater. Sol. Cells*, **130**, 551-554 (2014)

[25] J. Zou, H.-L. Yip, S.K. Hau, A.K.-Y. Jen, "Metal grid/conducting polymer hybrid transparent electrode for inverted polymer solar cells", *Appl. Phys. Lett.*, **96**, 203301 (2010)

[26] M. Song, H.-J. Kim, C.S. Kim, J.-H. Jeong, C. Cho, J.-Y. Lee, S.-H. Jin, D.-G. Choi, D.-H. Kim, "ITO-free highly bendable and efficient organic solar cells with Ag nanomesh/ZnO hybrid electrodes", *J. Mater. Chem. A*, **3**, 65-70 (2015)

[27] Y.H. Kim, C. Sachse, M.L. Machala, C. May, L. Müller-Meskamp, K. Leo, "Highly conductive PEDOT:PSS electrode with optimized solvent and thermal post-treatment for ito-free organic solar cells", *Adv. Funct. Mater.*, **21**, 1076-1081 (2011)

[28] W. Zhang, B. Zhao, Z. He, X. Zhao, H. Wang, S. Yang, H. Wu, Y. Cao, "High-efficiency ITO-free polymer solar cells using highly conductive PEDOT:PSS/surfactant bilayer transparent anodes", *Energy Environ. Sci.*, **6**, 1956-1964 (2013)

[29] Y. Wang, X. Chen, Y. Zhong, F. Zhu, K.P. Loh, "Large area, continuous, few-layered graphene as anodes in organic photovoltaic devices", *Appl. Phys. Lett.*, **95**, - (2009)

[30] H. Park, P.R. Brown, V. Bulovic, J. Kong, "Graphene as transparent conducting electrodes in organic photovoltaics: studies in graphene morphology, hole transporting layers, and counter electrodes", *Nano Lett.*,

12, 133-140 (2012)

[31] K. Sun, P. Li, Y. Xia, J. Chang, J. Ouyang, "Transparent conductive oxide-free perovskite solar cells with PEDOT:PSS as transparent electrode", *ACS Appl. Mater. Inter.*, **7**, 15314-15320 (2015)

Chapter 2.

Aerosols, Graphene, and Electronic/ Optoelectronic Devices

2.1. Aerosol Nanoparticles

2.1.1. Definition of Aerosols

Airborne particles are present throughout our environment in many forms such as mist, dust, fog, fume, smoke, or smog. These airborne particles are all examples of aerosols. These aerosols are closely related to our living environment given their influence on visibility, climate, and our health and quality of life.

An aerosol is defined as a suspension of liquid or solid particles in a gas – usually air. Particle size ranges from about 0.002 to more than 100 μm . [1] Monodisperse aerosols consist of particles with the same size and can be produced in laboratory for use as test aerosols. Most of aerosols generated naturally or artificially are polydisperse with a broad range of particle sizes.

2.1.2. Measurement of Size Distribution of Nanoparticles

Size distribution of aerosol NPs can be characterized by statistical measures. In this thesis, the size distribution of aerosol NPs has been characterized with a scanning mobility particle sizer (SMPS) system consisting of an electrostatic classifier (TSI 3080) with a Kr-85 radiative neutralizer, a nano-differential mobility analyzer (nano-DMA, TSI 3085), and a condensation nuclei counter (CNC, TSI 3776). A charged aerosol particle in electric field experiences an electrostatic force to move through the gas in which it is suspended. Then it very quickly reaches its terminal velocity. The resulting drag force on the particle is given by Stokes law and

can be equated to the electrostatic force to determine the electrical mobility of the particle.[1] The electrical mobility, then, is a measure of the particle's ability to move in an electric field. The electrical mobility, Z_p , is defined as [1]

$$Z_p = \frac{V_{TE}}{E} = \frac{neC_c}{3\pi\mu d_p} \text{ for } Re < 1 \quad (2.1)$$

where V_{TE} is the terminal electrical velocity, E is the electric field, e is the elementary charge, n is the number of elementary charge, μ is the viscosity of gas, d_p is the diameter of the particle, and C_c is the Cunningham slip correction factor, which is a correction factor associated with drag coefficient determined by

$$C_c = 1 + \frac{\lambda}{d_p} \left[2.34 + 1.05 \exp\left(-\frac{0.39d_p}{\lambda}\right) \right] \quad (2.2)$$

where λ is the gas mean free path.

The electrical mobility is also related to the parameters of nano-DMA (TSI 3085) by

$$Z_p = \frac{Q_{sh}}{2\pi VL} \ln\left(\frac{r_2}{r_1}\right) \quad (2.3)$$

where Q_{sh} is the sheath flow rate, V is the applied voltage on the inner collector rod of nano-DMA. L , r_1 , and r_2 is the length, inner radius, and outer radius of the nano-DMA, respectively.

By combining Equation (2.1) and Equation (2.3), an equation that relates the particle diameter to the collector rod voltage and the number of charges on the particle can be obtained:

$$d_p = \frac{2neVLC_c}{3\mu Q_{sh} \ln\left(\frac{r_2}{r_1}\right)} \quad (2.4)$$

Equation (2.4) allows to calculate the diameter of particles passing through the exit slit of the electrostatic classifier at a certain applied voltage to the collector rod of DMA if the number of charges on the particle is known. In the SMPS system used in this thesis, a Kr-85 neutralizer is used to charge the particles to a known bipolar charge distribution.[2] Then the number of the aerosol particles classified by the electrostatic classifier is counted by CNC. By sweeping the applied voltage to the collector rod of DMA, the size distribution of the particles is obtained.

2.2. Generation of Nanoparticles via Spark Discharge

Metal NPs possess unique optical, electronic, or chemical properties that can be tuned by controlling their composition, size, and shape.[3] Owing to these characteristics, they have been used for various applications including catalysis, [4,5] biological and chemical sensors, [6] and electronic and optoelectronic device.[7-11]

The most common method for utilizing metal NPs is the use of wet-chemically synthesized colloidal NPs. This method, however, may involve

undesirable solvent and residues along with NPs. On the other hand, the use of aerosol metal NPs that are prepared by physical methods such as evaporation/condensation and spark discharge has advantage in utilizing pure NPs without other additives such as solvent and surfactants.

Since the use of spark discharge generator (SDG) was first demonstrated to produce monodisperse carbon and gold aerosol particles in 1988 [12], research on the production of various aerosol NPs has been widely carried out using this method. SDGs are generally composed of two opposing electrodes separated by a gap, and an electric circuit is connected to the electrodes to control the spark generation. The electric circuit is commonly composed of a high voltage source, a capacitor, a resistor, and an inductor. As the shunt capacitor charges, electrical charges build up in the electrodes in the SDG, producing high electric field across the gap between electrodes. If the electric field is high enough, ionized gas molecules forms a conducting plasma channel through which spark discharge occurs. This rapid discharge generates a locally high temperature (between 20,000K and 30,000K), resulting in evaporation of electrode material. This evaporated could is followed by rapid cooling and transformed to NPs with the size range of 1 – 9 nm.

In 2012, Han et al. [13] suggested a newly designed SDG with a pin-to-plate configuration (PP-SDG) consisting of opposing electrodes with asymmetric geometry as shown in Figure 2.1a; a sharpened electrode and a grounded plate electrode with a central exit hole. Figure 2.1b shows the commonly used rod-to-rod type SDG (RR-SDG) consisting of two linearly opposing cylindrical electrodes with a gap between them. The electric circuit

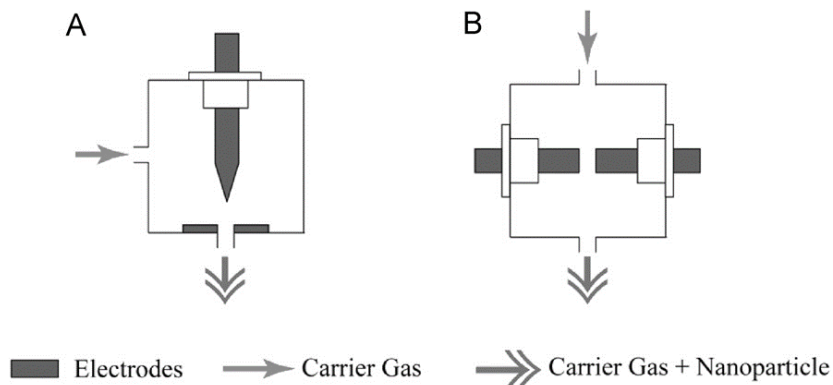


Figure 2.1 Schematics of the spark discharge generators with (a) a pin-to-plate configuration and (b) a rod-to-rod configuration.[13]

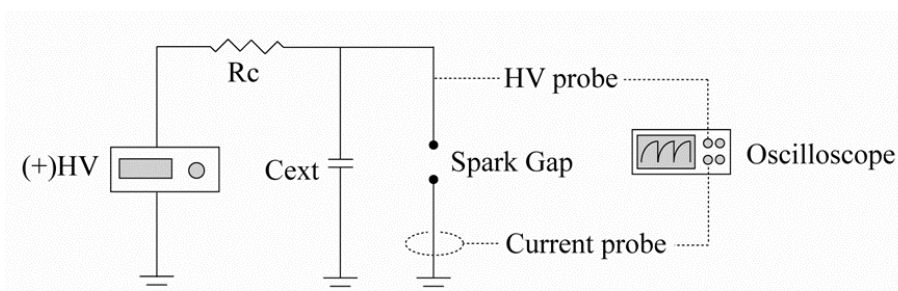


Figure 2.2 Schematic of an electric circuit connected to the electrode of the SDG to control spark generation.[13]

used to control the spark generation in both types of SDG was composed of a high voltage source, a capacitor of 8 nF, and a resistor of 10 M Ω , as shown in Figure 2.2.

Figure 2.3a and Figure 2.3b show the transmission electron microscopy (TEM) images of the Ag NPs generated from each type of SDG, respectively.

As shown, the PP-SDG was found to generate much smaller and unagglomerate NPs than the RR-SDG. The size distributions of the NPs were extracted from the TEM images based on the projected area equivalent diameter as shown in Figure 2.3c, from which the geometric mean diameter and the standard deviation of the silver NPs were found to be 5.36 nm and 1.37 for PP-SDG and 7.19 nm and 1.59 for RR-SDG, respectively. The generation of much smaller and unagglomerated NPs with a narrow size distribution from the PP-SDG compared to the RR-SDG was attributed the formation of a high flow velocity at the spark discharge sites in the PP-SDG. The evaporated electrode materials by spark discharge in the PP-SDG was immediately sucked out through the exit hole of the plate electrode where a high flow velocity was formed due to the small size of the exit hole.

Other kinds of unagglomerated metal NPs also can be produced with the PP-SDG by using electrodes with different materials. The NPs generated by spark discharge are inherently charged because their formation occurs in a plasm, and thus the charged aerosol NPs transported by a carrier gas such as nitrogen and argon can be collected using an electrostatic precipitator (ESP). It should be noted here that other additives such as dispersing solutions and surfactants, typically used when forming a NP layer by solution processing from NP dispersions, are not involved in this process. This is very beneficial to make use of NPs in devices that are vulnerable to or can be degraded by chemicals.

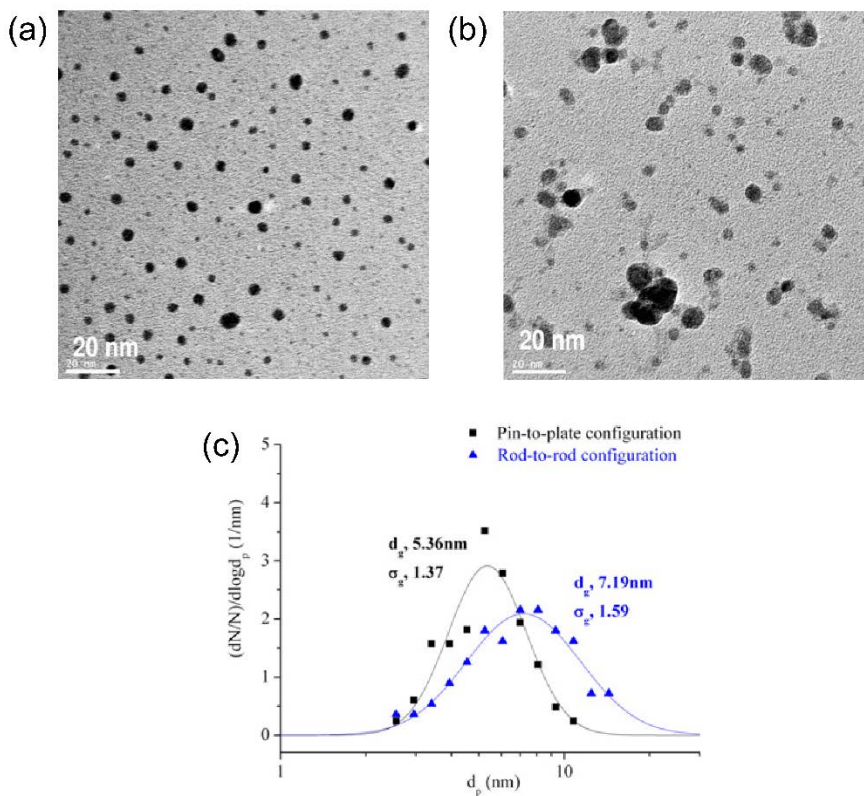


Figure 2.3 (a), (b) TEM images of the Ag nanoparticles generated by (a) pin-to-plate type SDG and (b) rod-to-rod type SDG. (c) Size distribution of the silver nanoparticles extracted from the TEM images based on the projected area equivalent diameter.[13]

2.3. Graphene

Graphene is a two dimensional single layer of carbon atoms arranged in a honeycomb lattice. Graphene forms graphite by weak interaction among

graphene layers or becomes carbon nanotubes or fullerenes by edge bonding. Graphene is an exciting material. Professor Andre Geim described graphene in New Scientist as follows: “Graphene is stronger and stiffer than diamonds, yet can be stretched by a quarter of its length, like rubber. Its surface area is the largest known for its weight.”[14] This implies that graphene with various superb properties (summarized in Table 2.1 [15]) possesses high potential to be utilized in diverse practical applications.

Table 2.1 Properties of Graphene

Property	Graphene	Remark
Mass density	$7.610 \times 10^{-8} \text{ g cm}^{-2}$ [16]	Aluminum: 2.7 g cm^{-3} [17]
Specific surface area	$2630 \text{ m}^2\text{g}^{-1}$ (Theoretical)	
Young’s modulus	1 TPa	30 times stronger than Kevlar 200 times stronger than steel
Ultimate strength	130 GPa	
Flexibility	Stable at very small bending radius	
Electrical conductivity	6000 S cm^{-1} (vacuum)	Isotropic conductivity unlike CNT
Thermal conductivity	$5000 \text{ W m}^{-1}\text{K}^{-1}$ (room temperature)	Diamond: $3320 \text{ W m}^{-1}\text{K}^{-1}$
Gas-barrier property	Perfect barrier[18]	
Transmittance	97.7%[19]	
Electron mobility	$200,000 \text{ cm}^2\text{V}^{-1}\text{s}^{-1}$ [20]	~100 times greater than that of Si

2.3.1. Electronic Properties

Graphene is composed of carbon atoms in a periodic hexagonal arrangement as shown in Figure 2.4. Each carbon atom with four valence

electrons in graphene bonds together with adjacent three carbon atoms via sp^2 hybridization, leaving the fourth electron to form π orbital that contributes to a delocalized network of electrons on the graphene plane. As the consequence of the hexagonal symmetry of graphene, the valence and conduction bands cross the Fermi level without a band gap at a single point (K points) in the Brillouin zone, and therefore graphene behaves as a semi-metal. Using a tight-binding approach considering the first nearest neighbor interaction, the dispersion relation that provides energy of the electrons with wave vector k near the K/K' points is obtained as[21,22]

$$E_{\pm}(\vec{k}) = \pm t \sqrt{1 + 4\cos\frac{\sqrt{3}k_x a}{2} \cos\frac{k_y a}{2} + 4\cos^2\frac{k_y a}{2}} \quad (2.5)$$

where $a=\sqrt{3}a_{CC}$, a_{CC} is carbon-carbon bonding length (0.142 nm), and t is the nearest neighbor hopping energy with a magnitude of 2.8 eV. The minus and plus signs correspond to the valence (π) band that is fully occupied in graphene and the empty conduction (π^*) band, respectively. By expanding Equation (2.5) near the K/K' points, the dispersion can be expressed as[19]

$$E_{\pm}(\vec{q}) \approx \pm \hbar v_F \sqrt{k_x^2 + k_y^2} \quad (2.6)$$

Where $\hbar = h/2\pi$ where h is Planck's constant, and v_F is the Fermi velocity given by $v_F = \sqrt{3} ta/2$ ($= \sim 1 \times 10^6$ ms⁻¹). This tight-binding approximation shows that graphene has a linear dispersion relation resembling the Dirac spectrum for massless fermions.[23] As a zero band gap material, graphene exhibits a strong ambipolar electric field effect. By

continuously tuning between electrons and holes, graphene has shown mobilities of up to 15,000 cm²/Vs at room temperature.[24,25] Significantly high mobilities over 200,000 cm²/Vs have also demonstrated in suspended graphene by minimizing impurity scattering. [20]

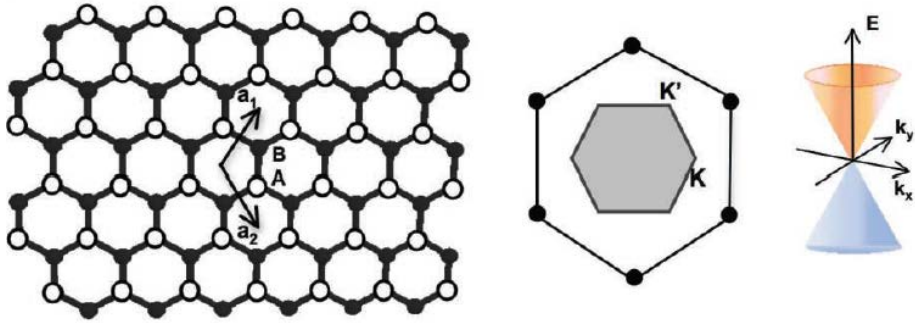


Figure 2.4 Schematics of graphene's crystal structure, Brillouin zone and dispersion spectrum.[19]

2.3.2. Optical Properties

The high-frequency conductivity G for Dirac fermions in graphene has been argued to be a universal constant equal to $\pi e^2/2h$ from the infrared through the visible frequency range.[26,27] The universal G implies that observable quantities such as graphene's transmittance T and reflectance R are also universal given by $T \equiv (1 + 2\pi G/c)^{-2} = (1+1/2\pi\alpha)^{-2}$ and $R \equiv 1/4\pi^2\alpha^2 T$ for the normal incidence light where $\alpha = 2\pi e^2/hc \approx 1/137$, e is the electron charge, c the light speed, and h Planck's constant. Then the opacity of graphene is obtained as $(1 - T) \approx \pi\alpha \approx 2.3\%$. This constant transparency

($\sim 97.7\%$) of graphene has been experimentally observed in the visible range as shown in Figure 2.5.[28] In addition, the transmission of graphene has been found to decrease with the number of graphene layer, by 2.3% with each added layer.

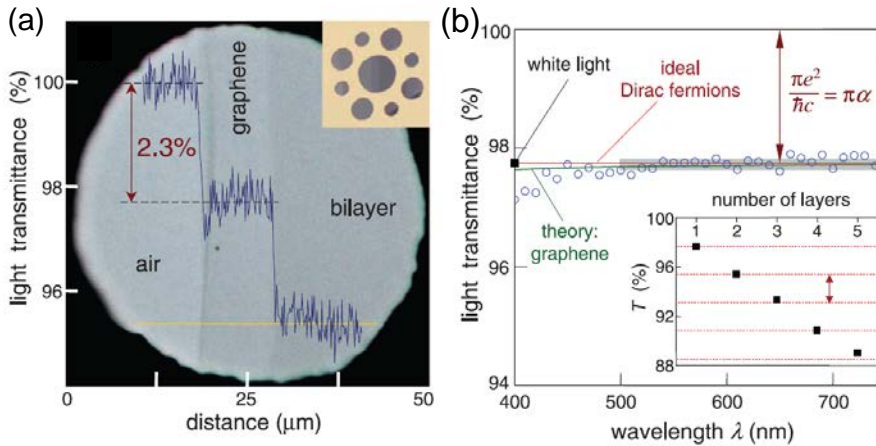


Figure 2.5 (a) Photograph of a 50- μm aperture partially covered with graphene and its bilayer. The line profile shows the intensity of the transmitted light along the yellow line. (b) Transmittance spectrum of single layer graphene (open circles). The red line is the transmittance $T = (1+1/2\pi\alpha)^{-2}$ expected for Dirac fermions in graphene, while the green line considers a nonlinearity and triangular warping of graphene's electronic spectrum. (Inset) The relation of transmittance and the number of graphene layer. The dashed lines indicate an intensity reduction by $\pi\alpha$ with each added layer.[28]

2.3.3. Raman Spectroscopy of Graphene

Raman spectroscopy has been widely used to characterize graphene because the Raman scattering process in graphene involves resonant and defect-activated processes. All sp^2 bonded carbons show common features in their Raman spectra, the so-called G ($\sim 1580\text{ cm}^{-1}$) and D ($\sim 1360\text{ cm}^{-1}$) peaks.[29] The G peak comes from the E_{2g} phonon mode by in-plane optical vibration of aromatic carbon rings. The D peak is generated by the breathing modes of six-atom rings and requires a defect for its activation.[30] The 2D peak is the D-peak overtone. Since this 2D peaks are activated by a process of momentum conservation satisfied by two phonons with opposite wave vectors, no defects are needed for their activation, and are always present in the Raman spectrum of graphene.[31] It was proposed that Raman could be used to distinguish the ‘quality’ of graphene and to determine the number of layers of graphene flakes by the shape, width, and position of the 2D peak.[32] Figure 2.6a shows an optical micrograph of a graphene flake composed of a different number of layers and Figure 2.6b shows the corresponding Raman spectra. As shown, no strong changes are observed from the G peak while the shape of 2D peak is strongly affected with increasing the number of graphene layers. Graphene presents a sharp and single 2D peak with a typical Full Width at Half Maximum (FWHM) of $\sim 30\text{ cm}^{-1}$. On the other hand, 2D peak of bi-layer graphene splits into four components and that of graphite into at least two components as shown in Figure 2.6c. Furthermore, the relative intensity between G and 2D peak is considerably different in graphene and graphite. When it comes to graphene,

the intensity of 2D peak is generally $\sim 4\text{--}6$ times larger than that of the G peak.[32] In addition, the relative intensity between D and G peak has been used as a measure of disorder in graphene, arising from ripples, edges, charged impurities, presence of domain boundaries, and others.[29]

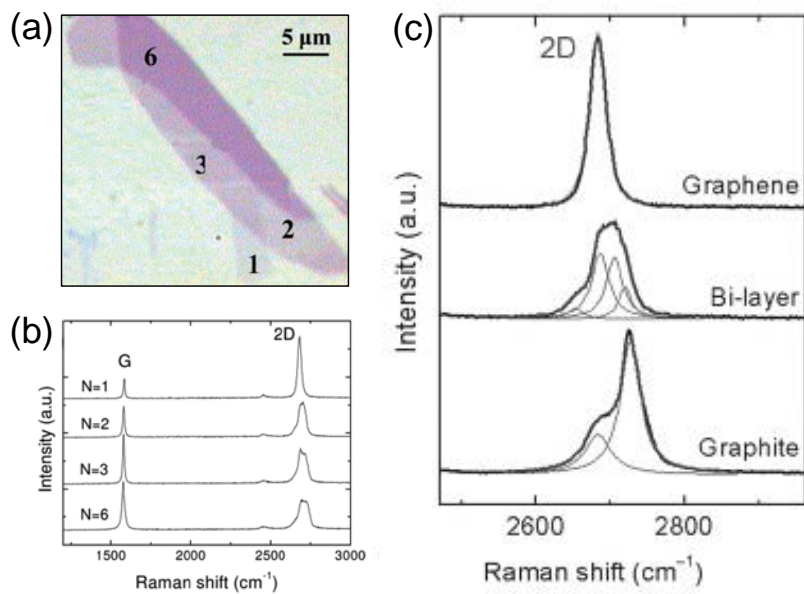


Figure 2.6 (a) Optical microscope image of a flake composed of different number (N) of graphene layers and (b) the corresponding Raman spectrum.[33] (c) The 2D peaks measured on single- and bi-layer graphene and graphite.[34]

2.4. Doping of Graphene

As addressed earlier, graphene is a zero band gap material with its valence and conduction bands linearly crossing at the corners of the Brillouin zone, the so-called Dirac points.[21,22] This suggests that the intrinsic charge carrier concentration of graphene is zero in principle when neglecting the effect of thermal excitations. However, it is required to control the carrier concentration and carrier type of graphene for its utilization in electronic devices, especially in complementary metal oxide semiconductor (CMOS) circuits which are widely used in the modern silicon-based semiconductor industry due to low static power consumption and high noise immunity.[35] In addition, complementary doping in graphene is also demanded in emerging novel devices based on P-N junction structure such as FETs and Veselago lens.[36,37] On this account, much research has been carried out to modify the majority carriers in graphene-based transistors, such as electric field effect doping and chemical doping.

The electric field effect doping is generally performed in graphene-based FETs. By applying the gate voltage charge carriers can be induced in graphene due to the electric potential developed between graphene and the gate (Si^+ , for example) across the dielectric film (SiO_2 , for example).[38,39] By varying the gate voltage, the type and concentration of charge carriers induced in graphene can be tuned. The polarity of the charge carriers induced on graphene is opposite to that of the applied gate voltage; a positive (negative) gate voltage induces electrons (holes).

Chemical doping is achieved by interactions of graphene with chemical species.[40] Chemical doping is classified to two types: substitutional and surface transfer doping. Substitutional doping involves substituting some of carbon atoms in graphene with other atoms with different number of valence electrons such as nitrogen and boron, which induces electrons and holes to graphene, respectively.[41,42] However, introduction of foreign atoms into graphene lattice can significantly change graphene's electronic structure, resulting in degrading its originally high electrical mobility.[42] The surface transfer doping occurs due to the charge transfer between graphene and surface adsorbates, not destroying the graphene lattice. If there exists a difference in energy level between graphene and an adsorbate, direct charge transfer occurs between them. As shown in Figure 2.7, if the lowest unoccupied molecular orbitals (LUMO) of an organic adsorbate lies in lower energy than the Fermi level of graphene, electrons will flow from graphene to adsorbate making graphene p-type doped (Figure 2.7a). If the HOMO of adsorbate lies in higher energy than the Fermi level of graphene, electrons will flow from adsorbate to graphene making graphene n-type doped (Figure 2.7b). When a metal particles are used as adsorbates, charge transfer occurs according to the relative position of the Fermi levels of the metal and graphene at the interface.[43,44] The concentration of charge carriers induced in graphene also can be tuned by the concentration of the adsorbates. The conductivity of graphene can be enhanced by increasing the charge carrier concentration, however, the ionized dopants can act as additional scattering sites for the charge carriers and reduce their mobility.

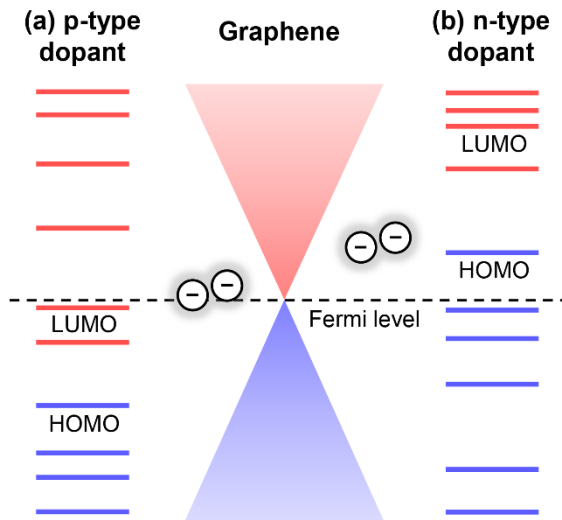


Figure 2.7 Scheme of the relative position of the highest occupied molecular orbitals (HOMO) and the lowest unoccupied molecular orbitals (LUMO) of an adsorbate to the Fermi level of graphene for (a) p-type and (b) n-type dopant.[45]

2.5. Electronic Devices: Graphene Field-Effect Transistors

A FET is a three-terminal device typically composed of a source contact, a channel with a gate, and a drain contact, as shown in Figure 2.8. The operation of a conventional FET depends on the control of the channel conductivity, and thus the drain current, which is varied by a gate voltage, V_g , applied between the gate and source.

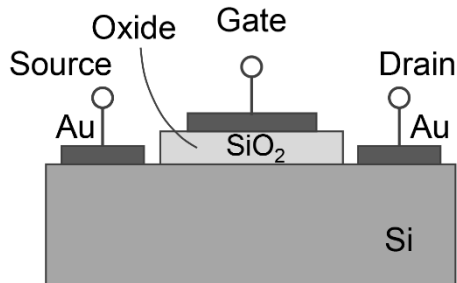


Figure 2.8 The traditional Si-based FETs formed on SiO₂ substrates [46].

The key issues in high-performance thin-film transistors are high on/off ratios and carrier mobilities for low-energy consumption and high-speed operation. The main obstacle for graphene is the absence of a band gap. Figure 2.9 shows the typical V-shaped drain current (I_d) – gate voltage (V_g) transfer characteristic of semimetal graphene transistors. The type of carrier (electrons or holes) and the carrier density in the graphene channel are controlled by the potential differences between the channel and the gates (top-gate and/or back-gate). Negative gate voltages cause hole accumulation in the channel, and larger negative gate voltage leads to a corresponding increase in the hole conduction. Similarly, positive gate voltages induce electron accumulation in the channel, and the electron conduction increases with higher positive values. The conduction is minimum at a certain gate voltage, which indicates the position of the Dirac point. In this case, the Dirac point is not located in zero voltage but upshifted due to p-type doping by adsorbed oxygen and moisture under ambient conditions. Such ambipolar

devices are not suitable for logic applications due to a lack of switch-off ability to offer low static power dissipation. However, the band gap of graphene can be opened by reducing the shape of graphene to several nanometer scale to form graphene nanoribbons,[47] by biasing bilayer graphene,[48] by doping,[49] and by applying strain to graphene.[50]

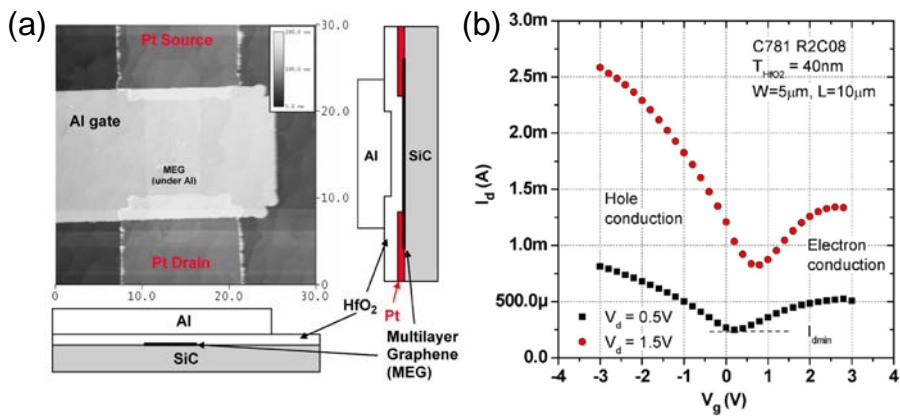


Figure 2.9 (a) AFM scan of top-gated transistor fabricated using epitaxial graphene on SiC as the active material. (b) $I_d - V_d$ characteristics of the device for two drain voltages showing typical V shape transfer characteristics for graphene transistors; current flows for both positive and negative top-gate voltages.[51]

2.6. Optoelectronic Devices I: Organic Light-Emitting Diodes

An organic light-emitting diode (OLED) is a light emitter with a thickness of about 100–200 nm. Since it is a self-lighting displaying device, it does not need backlight, which allows it to be thinner and less power-consuming than a liquid crystal display. It is also more efficient and has a wide viewing angle over 170°.

Since the electroluminescence properties of anthracene was discovered in the 1960s,[52] the first low-driving-voltage OLEDs were demonstrated in the 1980s.[53] In 1990s, the first OLEDs based on lanthanides elements [54] and very bright OLEDs based on transition metals phosphors [55] were presented. Since then, much progress on such devices has been made greatly to bring OLEDs into the market with full success.[56-58].

2.6.1. Structure and Light-Emitting Mechanism

A simplest OLED structure consists of a single organic layer between two metallic contacts. For this OLED to operate properly, the organic layer must have both good electron and hole transport properties because a photon is generated by recombination of a bound electron–hole pair, i.e. an exciton. However, such organic materials with both good hole and electron transport properties are not common, and thus most OLEDs are composed of two layers of organic material; the layer with good hole conducting properties is in contact with the anode whereas the other layer with good electron

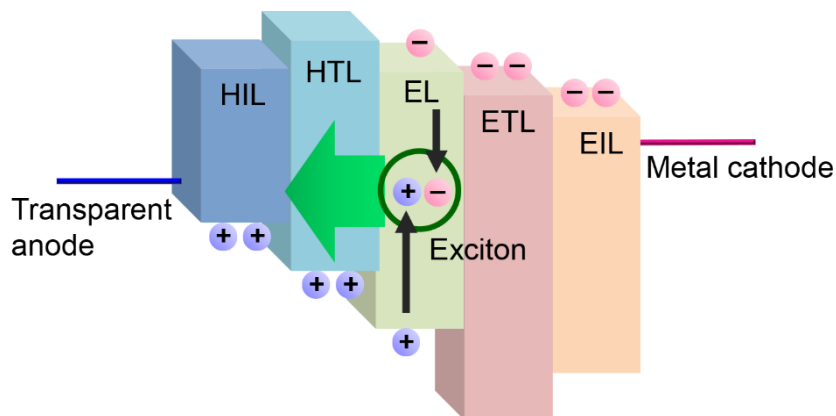


Figure 2.10 Light emitting mechanism of an OLED device

transporting properties is in contact with the cathode. The holes and electrons recombine at the interface to generate light. An extra emissive layer can be sandwiched between the hole and the electron transport layers which acts as a recombination sites of the holes and electrons. Other layers such as hole or electron injection layers also can be introduced in OLEDs in order to promote injection efficiency of charge carriers into the device by reducing Schottky barrier at the interface of the organic layers and metallic contacts.

The general structure of an OLED and its light-emitting mechanism is illustrated in Figure 2.10. Light emission from OLEDs is based on electroluminescence. When a voltage bias is applied to the device, electrons/holes are injected from cathode/anode to the electron/hole transport layers via electron/hole injection layers. These electrons/holes meet and generate excitons in the emissive layer. Finally, these excitons radiatively recombine to emit light. The wavelength of the emitted light is determined by the energy difference between LUMO and HOMO levels of the emissive

layer. The brightness of the OLED device is related to the number of electron–hole pairs which recombine radiatively, and thus a larger current passing through the device provides brighter light emission.

2.6.2. Fluorescence

Figure 2.11 shows the Jablonski diagram which represents the electronic energy levels in a molecule, and transfer/relaxation processes of the excited electron in the molecule. Fluorescence is light emission occurred by a radiative internal conversion of the excited electron from the lowest excited singlet state S_1 and the ground state S_0 . This process often proceeds quickly showing lifetime of $\sim 10^{-9} - 10^{-8}$ s. Phosphorescence is an intersystem crossing (ISC) process occurring between the lowest excited triplet state T_1 and the ground state S_0 . The typical lifetime of phosphorescence is $\sim 10^{-6} - 10$ s, longer than that of the fluorescence, because ISC is often a slow process. Electrons and holes are both fermions with spin = 1/2, and, statistically, the excitons formed by electrical injection have four different spin combinations of one singlet (antiparallel spins) and three triplets (parallel spins); 25% of the excitons are singlets and 75% of them are triplets.[59] The ground state S_0 for the organic molecules is a singlet state and the direct decay from T_1 to S_0 is forbidden. However, it can be allowed by interaction with heavy atoms or paramagnetic species in proximity because they increase spin-orbit interaction and facilitate the inter-system crossing. Therefore, in OLEDs using fluorescent organic emitters, only singlet excitons can decay radiatively, and triplet excitons decay through nonradiative channels, placing its theoretical limit on internal quantum efficiency of 25%.

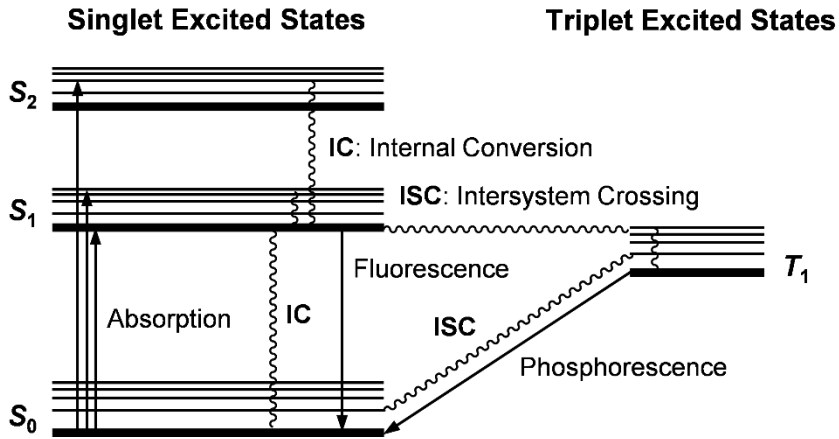


Figure 2.11. Jablonski diagram for absorption, fluorescence, and phosphorescence.

2.6.3. Measuring the Efficiency of OLEDs

There are various efficiencies employed in evaluating the fundamental emission properties of OLEDs, such as quantum efficiency, luminous efficiency, and power efficiency. The internal quantum efficiency η_{int} is the ratio of the total number of photons generated within the device to the number of electrons injected and can be written as[60]

$$\eta_{\text{int}} = \gamma\chi\phi \quad (2.7)$$

where γ is the electron–hole charge balance factor that is a measure of the balance between the number of holes and electrons injected in emissive layer, and probably close to 1 in relatively efficient OLEDs, χ is the fraction of excitons that decay radiatively ($\chi = 0.25$ for fluorescent, $\chi = 1$ for

phosphorescent emitters), and φ is the intrinsic quantum efficiency for radiative decay (including both fluorescence and phosphorescence).[61,62]

The external quantum efficiency η_{ext} is defined as the ratio of the number of photons emitted by the OLEDs into the viewing direction to the number of electrons injected, and can be expressed as[61,62]

$$\eta_{\text{ext}} = \eta_{\text{int}}\eta_{\text{out}} \quad (2.8)$$

where η_{out} is the out-coupling efficiency. According to classical ray optics theory, about 80% of generated light is lost in wave-guided modes due to the difference between refractive indexes of glass substrate and ITO/organic materials. Assuming a η_{out} of 20%, the maximum η_{ext} is limited to 5% in the case of fluorescent-based OLEDs because they only utilize singlet excitons for emission. On the other hand, phosphorescent OLEDs can utilize both singlet and triplet excitons for emission, allowing η_{ext} to reach 20%.[62,63].

The luminous (or current) efficiency η_{L} in candelas per amperes (cd A^{-1}) is the ratio of the luminous intensity in normal direction to the plane of emission to the current through the device. Given that the luminance (cd m^{-2}) is $L = I(\theta = 0)/S$ where I is the luminous intensity, θ is the emission angle and S is the emission area, and the electrical current density (A m^{-2}) is $J = I/S$, the luminous efficiency η_{L} is obtained as follows:

$$\eta_{\text{L}} = \frac{L}{J} \quad (2.9)$$

In many respects, η_{L} is equivalent to η_{ext} , with the exception that η_{L} weights

the photons according to the photopic response of the human eye, while η_{ext} weights all photons equally.[64]

The luminous power efficiency (η_P) in lumens per watt (lm W^{-1}) represents the ratio of the output power from an OLED (measured in lumens, which is the unit of light intensity perceived by the human eye) to the electrical power input (measured in watts), and can be calculated as

$$\eta_P = \frac{\Phi_{\text{total}}}{IV} = \frac{\int_{\lambda_1}^{\lambda_2} K_m V(\lambda) P_{\text{OLED}}(\lambda) d\lambda}{IV} \quad (2.10)$$

where the Φ_{total} is the total luminous flux in lumens (lm), K_m is the constant to convert from radiant to luminous scales in lumens per watts (lm W^{-1}), $V(\lambda)$ is the photo-optical response normalized with respect to the human eye whose values are zero outside of the visible spectrum between $\lambda_1 = 380 \text{ nm}$ and $\lambda_2 = 780 \text{ nm}$, P_{OLED} is the radiant flux emitted by the device in watts (W), and I is the electrical current in amperes (A) and V is the driving voltage in volts (V) of the device in operation.

In addition, when the emission of an OLED is Lambertian, the Φ_{total} is obtained in a simple form: πl_0 where l_0 is the maximum luminous intensity perpendicular to the emitting surface. Then, η_P can be simply given by:[65]

$$\eta_P = \frac{\pi l_0}{IV} = \frac{\pi \eta_L}{V} \quad (2.11)$$

2.6.4. Interaction between Fluorophores and Adjacent Metal Particles

The interaction of fluorophores and adjacent metal particles has been widely investigated in the metal enhanced fluorescence (MEF) research. In contrast to continuous metal surfaces, metal colloids present intense colors by a combination of both absorption and scattering.[66] Electrons can move over larger distances in a bulk metal while the distances are limited in metallic colloids due to their size, resulting in the creation of dipoles and higher order moments. By using Mie theory which considers small spherical particles and particles with a size comparable to the incident wavelength, the extinction cross section C_E of a particle with a dielectric constant ϵ_1 is written as[66]

$$C_E = C_A + C_S = k_1 \text{Im}(\alpha) + \frac{k_1^4}{6\pi} |\alpha^2| \quad (2.12)$$

where $k_1 = 2\pi n_1/\lambda_0$ is the wavevector of the incident light in medium 1 and α is the polarizability of the particle of radius r given as

$$\alpha = 4\pi r^3 \left(\frac{\epsilon_m - \epsilon_1}{\epsilon_m + 2\epsilon_1} \right) \quad (2.13)$$

where ϵ_m is the complex dielectric constant of the metal. In Equation (2.12), the first term represents the absorption cross section (C_A) and the second term the scattering cross section (C_S). When discussing the cross sections of colloids, it is convenient to use the efficiencies of extinction, absorption, and scattering, denoted by Q_E , Q_A , and Q_S , respectively, which are obtained by dividing the cross sections for interaction with light by the geometric cross

sections πr^2 . [67,68] These efficiencies present the ability of the particle to scatter light outside its physical cross sectional area, and are greater than unity because the field near the particle surface can exceed the average incident field in the medium. In the case of metal-enhanced fluorescence, the absorption term (C_A) and the scattering term (C_S) are considered to cause quenching and enhancement, respectively. Given the Equation (2.12) where C_A increases as r^3 whereas C_S increases as r^6 , it can be expected that larger metal colloids are desirable for metal-enhanced fluorescence.

The lifetimes of plasmons are very short, typically near 10 fs, which suggests that energy transfer is basically one way, fluorophore to metal. [69] Therefore, the enhanced quantum yield of a fluorophore near a metal surface can be understood by a rapid energy transfer to the plasmons and their radiation to the far-field, which was suggested as a radiating plasmon model. [66] This energy transfer is Forster transfer, and occurs before the donor can decay nonradiatively if the transfer rate is high.

The rate of energy transfer k_T to an acceptor or a group of acceptors, which can be a metal surface or typical fluorophores, depends on the distance R from the fluorophore to the acceptor as follows:

$$k_T = \frac{1}{\tau_0} \left(\frac{R_0}{R} \right)^n \quad (2.14)$$

where $n = 4$ or 3 for a plane or field half-space of acceptors, respectively, R_0 is the Forster distance, and τ_0 is the lifetime of the donor fluorophores in the absence of acceptors.

The quantum yield (Q_0) and lifetime (τ_0) of a donor in the absence of metal are given by

$$Q_0 = \frac{k_r}{k_r + k_{nr}} \quad (2.15)$$

and

$$\tau_0 = \frac{1}{k_r + k_{nr}} \quad (2.16)$$

where k_r is the intrinsic radiative decay rate and k_{nr} is the nonradiative decay rate in the absence of metal. The efficiency of energy transfer into the plasmons is given by

$$E_T = \frac{k_T}{k_r + k_{nr} + k_T} \quad (2.17)$$

As the rate of energy transfer becomes larger, the transfer efficiency approaches unity. Given this transfer efficiency, the total emission intensity (I_T) due to the fluorophore (I_F) and the radiating plasmon (I_P) can be obtained as follows:

$$I_T = I_F + I_P = k\varepsilon_F Q_0(1 - E_T) + k\varepsilon_F Q_S \quad (2.18)$$

where Q_S is the scattering quantum yield, ε_F is the absorption coefficient of the fluorophore, and k is an instrument constant. As E_T approaches 100%, the total emission intensity becomes

$$I_T = k\varepsilon_F Q_S \quad (2.19)$$

Thus, the overall quantum yield of the fluorophores becomes the scattering quantum yield by metal whether the quantum yield (Q_0) of the fluorophore is low or high. As discussed, in the light–metal interaction, the fraction of the light to be scattered (φ_S) is important for enhanced fluorescence and is defined as

$$\varphi_S = \frac{C_S}{C_E} = \frac{C_S}{C_A + C_S} \quad (2.20)$$

Again, the relative contribution of absorption and scattering depends on the size of the metal colloids. For example, as shown in Figure 2.12, the scattering efficiency of both silver and gold colloids approaches unity for larger particles. [70]

This value is defined as $\varphi_S = \frac{C_S}{C_E} = \frac{C_S}{C_A + C_S}$ and the relative contribution of absorption and scattering depends on the metal and on the size of the colloids. For example, as shown in both silver and gold colloids the scattering efficiency approaches unity for larger particles. This suggests that larger metallic colloids are likely to be preferred for metal-enhanced fluorescence and that the optimal size for metal-enhanced fluorescence is near 80 nm in diameter.

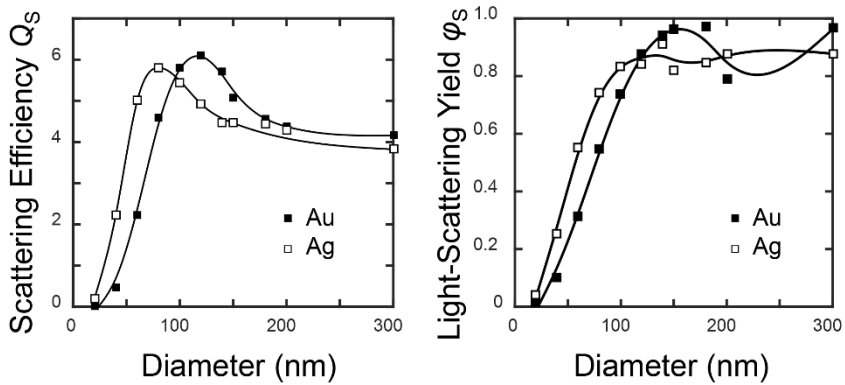


Figure 2.12 Effect of the particle size on the scattering efficiency Q_s and the light-scattering yield (ϕ_s) of gold and silver colloids. Data from [71].

2.7. Optoelectronic Devices II: Perovskite-Based Solar Cells

2.7.1. Perovskite: Structure and Properties

Perovskite is a material with a crystal structure with the AMX_3 formula where X is an oxygen or halogen anion, A is a larger metal cation occupying a cubo-octahedral site shared with twelve X anions, and M is smaller metal cation occupying an octahedral site shared with six X anions. Figure 2.13 shows the crystal structure of methylammonium lead iodide ($CH_3NH_3PbI_3$) which has been widely used as an absorber for perovskite-based solar cell applications.

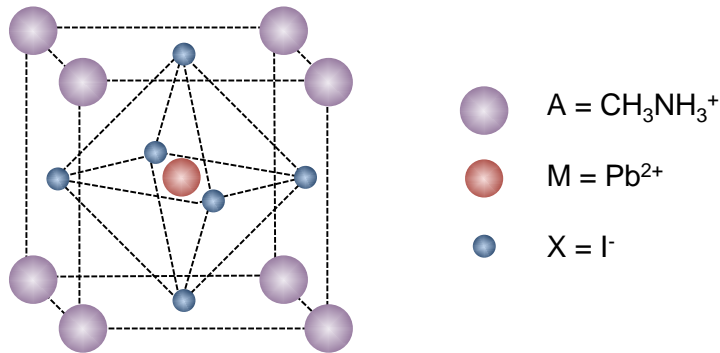


Figure 2.13 Crystal structure of $\text{CH}_3\text{NH}_3\text{PbI}_3$

The band gap of hybrid organic-inorganic perovskites can be tuned either by changing the alkyl group, the metal atom, or the halide.[72,73] Kim et al. have determined the band gap (E_g) and the position of the valence band maximum (E_v) of the $\text{CH}_3\text{NH}_3\text{PbI}_3$ based on diffuse reflectance spectroscopy and ultraviolet photoelectron spectroscopy measurements, respectively.[74]; E_g and E_v of the $\text{CH}_3\text{NH}_3\text{PbI}_3$ deposited on a TiO_2 film were estimated to be 1.5 eV and -5.43 eV, respectively. Accordingly, its conduction band energy (E_{CB}) is determined to be -3.93 eV.

The electron mobility of $\text{CH}_3\text{NH}_3\text{PbI}_3$ was determined to be $66 \text{ cm}^2\text{V}^{-1}\text{s}^{-1}$ by Stoumpos et al.[75], which is much higher than the carrier mobilities of organic semiconductors, ranging between 10^{-5} to $10^0 \text{ cm}^2\text{V}^{-1}\text{s}^{-1}$. [76] Also, the electron mobility of $\text{CH}_3\text{NH}_3\text{SnI}_3$ was found to be $2320 \text{ cm}^2\text{V}^{-1}\text{s}^{-1}$, [75] which is even comparable to that of classical silicon semiconductors ($1400 \text{ cm}^2\text{V}^{-1}\text{s}^{-1}$).

The diffusion length of both electrons and holes of perovskites has been reported to be very similar, [77,78] and this ambipolar character of

$\text{CH}_3\text{NH}_3\text{PbI}_3$ was verified by a recent theoretical work.[79] In this report, the effective masses of photogenerated electrons and holes in $\text{CH}_3\text{NH}_3\text{PbI}_3$ were estimated to be $m_e^* = 0.23m_0$ and $m_h^* = 0.29m_0$, respectively, including spin-orbit coupling effects, which supports both the long-range ambipolar transport property and the larger diffusion constant for electrons compared with that for holes in $\text{CH}_3\text{NH}_3\text{PbI}_3$. Furthermore, these values are comparable to those in silicon, suggesting the high potentiality in photovoltaic applications.

The diffusion length of electrons and holes in $\text{CH}_3\text{NH}_3\text{PbI}_3$ was found to be 100 nm,[78] and it has been demonstrated that, by doping a small amount of Cl, it can be increased to over 1 μm in mixed halide $\text{CH}_3\text{NH}_3\text{PbI}_{3-x}\text{Cl}_x$ without altering its optical properties.[77,80]

2.7.2. Perovskite Application in Photovoltaic Devices

In 2009, Miyasaka et al. first employed $\text{CH}_3\text{NH}_3\text{PbX}_3$ ($X = \text{Br}$ and I) as a semiconductor sensitizer to a dye-sensitized solar cells.[81] However, little attention was paid due to their low power conversion efficiency (PCE) of 3 – 4% and significantly unstable liquid electrolytes. Although Park et al. reported a $\text{CH}_3\text{NH}_3\text{PbI}_3$ perovskite solar cell with PCE of 6.5%, [82] stability was still a problem. An organic-inorganic halide perovskite was an ionic crystal so that it easily dissolved in polar liquid electrolytes. In 2012, Park et al. reported 9.7% efficient $\text{CH}_3\text{NH}_3\text{PbI}_3$ -sensitized solar cells with high stability by substituting liquid electrolytes with a solid hole conductor.[74] In the same year, Snaith et al. demonstrated a non-sensitized type-perovskite solar cell with PCE of 10.9% using a $\text{CH}_3\text{NH}_3\text{PbI}_{3-x}\text{Cl}_x$ -coated Al_2O_3

film.[83] These achievements triggered rapid progress in perovskite solar cell research,[84-86] reaching a PCE over 20% [87].

2.8. References

- [1] W.C. Hinds, "Aerosol technology: properties, behavior, and measurement of airborne particles"(1999), *John Wiley & Sons*,
- [2] A. Wiedensohler, H.J. Fissan, "Aerosol charging in high purity gases", *J. Aerosol Sci.*, **19**, 867-870 (1988)
- [3] M.-C. Daniel, D. Astruc, "Gold nanoparticles: assembly, supramolecular chemistry, quantum-size-related properties, and applications toward biology, catalysis, and nanotechnology", *Chem. Rev.*, **104**, 293-346 (2003)
- [4] M. Haruta, "Catalysis of gold nanoparticles deposited on metal oxides", *CATTECH*, **6**, 102-115 (2002)
- [5] R. Narayanan, M.A. El-Sayed, "Shape-dependent catalytic activity of platinum nanoparticles in colloidal solution", *Nano Lett.*, **4**, 1343-1348 (2004)
- [6] J.N. Anker, W.P. Hall, O. Lyandres, N.C. Shah, J. Zhao, R.P. Van Duyne, "Biosensing with plasmonic nanosensors", *Nat. Mater.*, **7**, 442-453 (2008)
- [7] K.R. Catchpole, S. Pillai, "Surface plasmons for enhanced silicon light-emitting diodes and solar cells", *J. Lumin.*, **121**, 315-318 (2006)
- [8] M.-K. Kwon, J.-Y. Kim, B.-H. Kim, I.-K. Park, C.-Y. Cho, C.C. Byeon, S.-J. Park, "Surface-plasmon-enhanced light-emitting diodes", *Adv. Mater.*, **20**, 1253-1257 (2008)
- [9] A. Fujiki, T. Uemura, N. Zettsu, M. Akai-Kasaya, A. Saito, Y.

- Kuwahara, "Enhanced fluorescence by surface plasmon coupling of Au nanoparticles in an organic electroluminescence diode", *Appl. Phys. Lett.*, **96**, (2010)
- [10] D. Derkacs, S.H. Lim, P. Matheu, W. Mar, E.T. Yu, "Improved performance of amorphous silicon solar cells via scattering from surface plasmon polaritons in nearby metallic nanoparticles", *Appl. Phys. Lett.*, **89**, 093103-093103 (2006)
- [11] F.-C. Chen, J.-L. Wu, C.-L. Lee, Y. Hong, C.-H. Kuo, M.H. Huang, "Plasmonic-enhanced polymer photovoltaic devices incorporating solution-processable metal nanoparticles", *Appl. Phys. Lett.*, **95**, 013305 (2009)
- [12] S. Schwyn, E. Garwin, A. Schmidt-Ott, "Aerosol generation by spark discharge", *J. Aerosol Sci.*, **19**, 639-642 (1988)
- [13] K. Han, W. Kim, J. Yu, J. Lee, H. Lee, C. Gyu Woo, M. Choi, "A study of pin-to-plate type spark discharge generator for producing unagglomerated nanoaerosols", *J. Aerosol Sci.*, **52**, 80-88 (2012)
- [14] "Andre Geim: Why graphene is the stuff of the future", *New Scientist*, (2010)
- [15] X. Qi, C. Tan, J. Wei, H. Zhang, "Synthesis of graphene-conjugated polymer nanocomposites for electronic device applications", *Nanoscale*, **5**, 1440-1451 (2013)
- [16] E.H. Hwang, S. Das Sarma, "Acoustic phonon scattering limited carrier mobility in two-dimensional extrinsic graphene", *Phys. Rev. B*, **77**, 115449 (2008)
- [17] J.R. Davis, "Corrosion of aluminum and aluminum alloys"(1999), *Asm International*,

- [18] J.S. Bunch, S.S. Verbridge, J.S. Alden, A.M. van der Zande, J.M. Parpia, H.G. Craighead, P.L. McEuen, "Impermeable atomic membranes from graphene sheets", *Nano Lett.*, **8**, 2458-2462 (2008)
- [19] Y. Zhu, S. Murali, W. Cai, X. Li, J.W. Suk, J.R. Potts, R.S. Ruoff, "Graphene and graphene oxide: synthesis, properties, and applications", *Adv. Mater.*, **22**, 3906-3924 (2010)
- [20] K.I. Bolotin, K.J. Sikes, Z. Jiang, M. Klima, G. Fudenberg, J. Hone, P. Kim, H.L. Stormer, "Ultrahigh electron mobility in suspended graphene", *Solid State Commun.*, **146**, 351-355 (2008)
- [21] P.R. Wallace, "The band theory of graphite", *Phys. Rev.*, **71**, 622-634 (1947)
- [22] A.H. Castro Neto, F. Guinea, N.M.R. Peres, K.S. Novoselov, A.K. Geim, "The electronic properties of graphene", *Rev. Mod. Phys.*, **81**, 109-162 (2009)
- [23] A.K. Geim, K.S. Novoselov, "The rise of graphene", *Nat. Mater.*, **6**, 183-191 (2007)
- [24] K.S. Novoselov, A.K. Geim, S.V. Morozov, D. Jiang, M.I. Katsnelson, I.V. Grigorieva, S.V. Dubonos, A.A. Firsov, "Two-dimensional gas of massless Dirac fermions in graphene", *Nature*, **438**, 197-200 (2005)
- [25] Y. Zhang, Y.-W. Tan, H.L. Stormer, P. Kim, "Experimental observation of the quantum Hall effect and Berry's phase in graphene", *Nature*, **438**, 201-204 (2005)
- [26] N.M.R. Peres, F. Guinea, A.H. Castro Neto, "Electronic properties of disordered two-dimensional carbon", *Phys. Rev. B*, **73**, 125411 (2006)
- [27] V.P. Gusynin, S.G. Sharapov, J.P. Carbotte, "Unusual microwave

response of Dirac quasiparticles in graphene", *Phys. Rev. Lett.*, **96**, 256802 (2006)

[28] R.R. Nair, P. Blake, A.N. Grigorenko, K.S. Novoselov, T.J. Booth, T. Stauber, N.M.R. Peres, A.K. Geim, "Fine structure constant defines visual transparency of graphene", *Science*, **320**, 1308 (2008)

[29] A.C. Ferrari, "Raman spectroscopy of graphene and graphite: Disorder, electron-phonon coupling, doping and nonadiabatic effects", *Solid State Commun.*, **143**, 47-57 (2007)

[30] A.C. Ferrari, D.M. Basko, "Raman spectroscopy as a versatile tool for studying the properties of graphene", *Nat. Nanotechnol.*, **8**, 235-246 (2013)

[31] D.M. Basko, S. Piscanec, A.C. Ferrari, "Electron-electron interactions and doping dependence of the two-phonon Raman intensity in graphene", *Phys. Rev. B*, **80**, 165413 (2009)

[32] A.C. Ferrari, J.C. Meyer, V. Scardaci, C. Casiraghi, M. Lazzeri, F. Mauri, S. Piscanec, D. Jiang, K.S. Novoselov, S. Roth, A.K. Geim, "Raman spectrum of graphene and graphene layers", *Phys. Rev. Lett.*, **97**, 187401 (2006)

[33] C. Casiraghi, A. Hartschuh, E. Lidorikis, H. Qian, H. Harutyunyan, T. Gokus, K.S. Novoselov, A.C. Ferrari, "Rayleigh imaging of graphene and graphene layers", *Nano Lett.*, **7**, 2711-2717 (2007)

[34] C. Casiraghia, "Raman spectroscopy of graphene", *Spectrosc. Prop. Inorg. Organomet. Compd.*, **43**, 29-56 (2012)

[35] F. Schwierz, "Graphene transistors", *Nat Nano*, **5**, 487-496 (2010)

[36] B. Zhan, C. Li, J. Yang, G. Jenkins, W. Huang, X. Dong, "Graphene

field-effect transistor and its application for electronic sensing", *Small*, **10**, 4042-4065 (2014)

[37] V.V. Cheianov, V. Fal'ko, B.L. Altshuler, "The focusing of electron flow and a Veselago lens in graphene p-n junctions", *Science*, **315**, 1252-1255 (2007)

[38] K.S. Novoselov, A.K. Geim, S.V. Morozov, D. Jiang, Y. Zhang, S.V. Dubonos, I.V. Grigorieva, A.A. Firsov, "Electric field effect in atomically thin carbon films", *Science*, **306**, 666-669 (2004)

[39] R. Dharmendar, F.R. Leonard, D.C. Gary, K.B. Sanjay, "Graphene field-effect transistors", *J. Phys. D: Appl. Phys.*, **44**, 313001 (2011)

[40] H. Liu, Y. Liu, D. Zhu, "Chemical doping of graphene", *J. Mater. Chem. A*, **21**, 3335-3345 (2011)

[41] L.S. Panchakarla, K.S. Subrahmanyam, S.K. Saha, A. Govindaraj, H.R. Krishnamurthy, U.V. Waghmare, C.N.R. Rao, "Synthesis, structure, and properties of boron- and nitrogen-doped graphene", *Adv. Mater.*, **21**, 4726-4730 (2009)

[42] D. Wei, Y. Liu, Y. Wang, H. Zhang, L. Huang, G. Yu, "Synthesis of n-doped graphene by chemical vapor deposition and its electrical properties", *Nano Lett.*, **9**, 1752-1758 (2009)

[43] X. Shi, G. Dong, M. Fang, F. Wang, H. Lin, W.-C. Yen, K.S. Chan, Y.-L. Chueh, J.C. Ho, "Selective n-type doping in graphene via the aluminium nanoparticle decoration approach", *J. Mater. Chem. A*, **2**, 5417 (2014)

[44] Y. Wu, W. Jiang, Y. Ren, W. Cai, W.H. Lee, H. Li, R.D. Piner, C.W. Pope, Y. Hao, H. Ji, J. Kang, R.S. Ruoff, "Tuning the doping type and level

- of graphene with different gold configurations", *Small*, **8**, 3129-3136 (2012)
- [45] H. Pinto, A. Markevich, "Electronic and electrochemical doping of graphene by surface adsorbates", *Beilstein J. Nanotech.*, **5**, 1842-1848 (2014)
- [46] C. Yu, H. Liu, W. Ni, N. Gao, J. Zhao, H. Zhang, "Theoretical study of the source-drain current and gate leakage current to understand the graphene field-effect transistors", *Phys. Chem. Chem. Phys.*, **13**, 3461-3467 (2011)
- [47] X. Li, X. Wang, L. Zhang, S. Lee, H. Dai, "Chemically derived, ultrasmooth graphene nanoribbon semiconductors", *Science*, **319**, 1229-1232 (2008)
- [48] Y. Zhang, T.-T. Tang, C. Girit, Z. Hao, M.C. Martin, A. Zettl, M.F. Crommie, Y.R. Shen, F. Wang, "Direct observation of a widely tunable bandgap in bilayer graphene", *Nature*, **459**, 820-823 (2009)
- [49] Y.-B. Tang, L.-C. Yin, Y. Yang, X.-H. Bo, Y.-L. Cao, H.-E. Wang, W.-J. Zhang, I. Bello, S.-T. Lee, H.-M. Cheng, C.-S. Lee, "Tunable band gaps and p-type transport properties of boron-doped graphenes by controllable ion doping using reactive microwave plasma", *ACS Nano*, **6**, 1970-1978 (2012)
- [50] V.M. Pereira, A.H. Castro Neto, N.M.R. Peres, "Tight-binding approach to uniaxial strain in graphene", *Phys. Rev. B*, **80**, 045401 (2009)
- [51] J. Kedzierski, H. Pei-Lan, P. Healey, P.W. Wyatt, C.L. Keast, M. Sprinkle, C. Berger, W.A. de Heer, "Epitaxial graphene transistors on SiC substrates", *Electron Devices, IEEE Transactions on*, **55**, 2078-2085 (2008)
- [52] M. Pope, H.P. Kallmann, P. Magnante, "Electroluminescence in organic crystals", *J. Chem. Phys.*, **38**, 2042-2043 (1963)
- [53] C.W. Tang, S.A. VanSlyke, "Organic electroluminescent diodes",

Appl. Phys. Lett., **51**, 913-915 (1987)

[54] J. Kido, K. Nagai, Y. Ohashi, "Electroluminescence in a Terbium complex", *Chem. Lett.*, **19**, 657-660 (1990)

[55] M.A. Baldo, D.F. O'Brien, Y. You, A. Shoustikov, S. Sibley, M.E. Thompson, S.R. Forrest, "Highly efficient phosphorescent emission from organic electroluminescent devices", *Nature*, **395**, 151-154 (1998)

[56] J. Wang, F. Zhang, J. Zhang, W. Tang, A. Tang, H. Peng, Z. Xu, F. Teng, Y. Wang, "Key issues and recent progress of high efficient organic light-emitting diodes", *J. Photoch. Photobio. C*, **17**, 69-104 (2013)

[57] S. Ho, S. Liu, Y. Chen, F. So, "Review of recent progress in multilayer solution-processed organic light-emitting diodes", *PHOTOE*, **5**, 057611-057611 (2015)

[58] M.S. AlSalhi, J. Alam, L.A. Dass, M. Raja, "Recent advances in conjugated polymers for light emitting devices", *Int. J. Mol. Sci.*, **12**, 2036-2054 (2011)

[59] H. Yersin, "Highly efficient OLEDs with phosphorescent materials"(2008), *John Wiley & Sons*,

[60] S.M. Sze, K.K. Ng, "Physics of semiconductor devices"(2006), *John Wiley & Sons*,

[61] S.R. Forrest, D.D.C. Bradley, M.E. Thompson, "Measuring the efficiency of organic light-emitting devices", *Adv. Mater.*, **15**, 1043-1048 (2003)

[62] K. Saxena, V.K. Jain, D.S. Mehta, "A review on the light extraction techniques in organic electroluminescent devices", *Optical Materials*, **32**, 221-233 (2009)

- [63] S.R. Forrest, "The road to high efficiency organic light emitting devices", *Org. Electron.*, **4**, 45-48 (2003)
- [64] D. Liu, in *Organometallics and Related Molecules for Energy Conversion*, Springer, 2015, 241-284
- [65] L.F. Pereira, "Organic light emitting diodes: the use of rare earth and transition metals"(2012), *CRC Press*,
- [66] L. Joseph R, "Radiative decay engineering 5: metal-enhanced fluorescence and plasmon emission", *Anal. Biochem.*, **337**, 171-194 (2005)
- [67] D.L. Fedlheim, C.A. Foss, "Metal nanoparticles: synthesis, characterization, and applications"(2001), *CRC Press*,
- [68] M. Kerker, C.G. Blatchford, "Elastic scattering, absorption, and surface-enhanced Raman scattering by concentric spheres comprised of a metallic and a dielectric region", *Phys. Rev. B*, **26**, 4052-4063 (1982)
- [69] M. Scharte, R. Porath, T. Ohms, M. Aeschlimann, J.R. Krenn, H. Ditlbacher, F.R. Aussenegg, A. Liebsch, "Do Mie plasmons have a longer lifetime on resonance than off resonance?", *Applied Physics B*, **73**, 305-310 (2001)
- [70] J. Yguerabide, E.E. Yguerabide, "Light-scattering submicroscopic particles as highly fluorescent analogs and their use as tracer labels in clinical and biological applications: I. Theory", *Anal. Biochem.*, **262**, 137-156 (1998)
- [71] J. Yguerabide, E.E. Yguerabide, "Light-scattering submicroscopic particles as highly fluorescent analogs and their use as tracer labels in clinical and biological applications: II. experimental characterization", *Anal. Biochem.*, **262**, 157-176 (1998)
- [72] J.L. Knutson, J.D. Martin, D.B. Mitzi, "Tuning the band gap in

- hybrid Tin Iodide perovskite semiconductors using structural templating", *Inorg. Chem.*, **44**, 4699-4705 (2005)
- [73] D.B. Mitzi, "Templating and structural engineering in organic-inorganic perovskites", *Journal of the Chemical Society, Dalton Transactions*, 1-12 (2001)
- [74] H.-S. Kim, C.-R. Lee, J.-H. Im, K.-B. Lee, T. Moehl, A. Marchioro, S.-J. Moon, R. Humphry-Baker, J.-H. Yum, J.E. Moser, M. Grätzel, N.-G. Park, "Lead Iodide perovskite sensitized all-solid-state submicron thin film mesoscopic solar cell with efficiency exceeding 9%", *Sci. Rep.*, **2**, 591 (2012)
- [75] C.C. Stoumpos, C.D. Malliakas, M.G. Kanatzidis, "Semiconducting tin and lead iodide perovskites with organic cations: phase transitions, high mobilities, and near-infrared photoluminescent properties", *Inorg. Chem.*, **52**, 9019-9038 (2013)
- [76] H. Hoppe, N.S. Sariciftci, "Organic solar cells: An overview", *J. Mater. Res.*, **19**, 1924-1945 (2004)
- [77] S.D. Stranks, G.E. Eperon, G. Grancini, C. Menelaou, M.J.P. Alcocer, T. Leijtens, L.M. Herz, A. Petrozza, H.J. Snaith, "Electron-hole diffusion lengths exceeding 1 micrometer in an organometal trihalide perovskite absorber", *Science*, **342**, 341-344 (2013)
- [78] G. Xing, N. Mathews, S. Sun, S.S. Lim, Y.M. Lam, M. Grätzel, S. Mhaisalkar, T.C. Sum, "Long-range balanced electron- and hole-transport lengths in organic-inorganic CH₃NH₃Pb₃", *Science*, **342**, 344-347 (2013)
- [79] G. Giorgi, J.-I. Fujisawa, H. Segawa, K. Yamashita, "Small photocarrier effective masses featuring ambipolar transport in Methylammonium Lead Iodide perovskite: a density functional analysis", *J.*

Phys. Chem. Lett., **4**, 4213-4216 (2013)

[80] S. Colella, E. Mosconi, P. Fedeli, A. Listorti, F. Gazza, F. Orlandi, P. Ferro, T. Besagni, A. Rizzo, G. Calestani, G. Gigli, F. De Angelis, R. Mosca, "MAPbI₃-xCl_x mixed halide perovskite for hybrid solar cells: The role of Chloride as dopant on the transport and structural properties", *Chem. Mater.*, **25**, 4613-4618 (2013)

[81] A. Kojima, K. Teshima, Y. Shirai, T. Miyasaka, "Organometal halide perovskites as visible-light sensitizers for photovoltaic cells", *J. Am. Chem. Soc.*, **131**, 6050-6051 (2009)

[82] J.-H. Im, C.-R. Lee, J.-W. Lee, S.-W. Park, N.-G. Park, "6.5% efficient perovskite quantum-dot-sensitized solar cell", *Nanoscale*, **3**, 4088-4093 (2011)

[83] M.M. Lee, J. Teuscher, T. Miyasaka, T.N. Murakami, H.J. Snaith, "Efficient hybrid solar cells based on meso-superstructured organometal halide perovskites", *Science*, **338**, 643-647 (2012)

[84] M. Liu, M.B. Johnston, H.J. Snaith, "Efficient planar heterojunction perovskite solar cells by vapour deposition", *Nature*, **501**, 395-398 (2013)

[85] J.H. Heo, H.J. Han, D. Kim, T.K. Ahn, S.H. Im, "Hysteresis-less inverted CH₃NH₃PbI₃ planar perovskite hybrid solar cells with 18.1% power conversion efficiency", *Energy Environ. Sci.*, **8**, 1602-1608 (2015)

[86] N.J. Jeon, J.H. Noh, W.S. Yang, Y.C. Kim, S. Ryu, J. Seo, S.I. Seok, "Compositional engineering of perovskite materials for high-performance solar cells", *Nature*, **517**, 476-480 (2015)

[87] W.S. Yang, J.H. Noh, N.J. Jeon, Y.C. Kim, S. Ryu, J. Seo, S.I. Seok,

"High-performance photovoltaic perovskite layers fabricated through intramolecular exchange", *Science*, **348**, 1234-1237 (2015)

Chapter 3.

Performance Enhancement of Organic Light-Emitting Diodes by Position- Controlled Incorporation of Nanoparticles

3.1. Introduction

In many applications, electronic and optoelectronic devices in particular, metal NPs (MNPs) need to be located inside the device to properly operate or to fully exploit benefits that MNPs offer. For example, organic non-volatile memory devices operate based on charge trapping on Au NPs located between two electrodes.[1] Surface-plasmon-enhanced light-emitting devices[2,3] and solar cells[4,5] also demand close proximity between MNPs and photoactive materials for enhanced light-matter interactions.

However, incorporation of MNPs in the middle of an inorganic device, typically made of crystalline or poly-crystalline active materials, can significantly degrade the crystalline quality of the subsequent layer, leading to degraded electrical and/or optical properties. For this reason, in most demonstrations of inorganic devices employing MNPs, MNPs have been positioned outside the devices or away from active regions,[4,6] not fully making use of benefits that NPs offer. Meanwhile, organic electronic and optoelectronic devices, such as organic light-emitting devices (OLEDs)[7], organic solar cells (OSCs),[8,9] and organic memory devices,[1] are comprised of small-molecules or polymers that are typically held together by weak van der Waals forces. Therefore, in organic devices, lattice matching is not required when forming a heterojunction between dissimilar materials unlike in inorganic counterparts. This suggests that the presence of MNPs in an organic device does not provide electrical or optical degradation arising

from the change in thin-film crystallinity, making it a good platform for MNP-embedded devices.

However, these weakly bonded organic solids can be easily damaged or degraded by exposure to a wet chemical or a high temperature process, presenting limitations to introducing MNPs in the interior of an organic device. For this reason, in some MNP-enhanced organic devices, especially those made of small molecules, MNPs have been placed on a bottom electrode before deposition of organic materials.[3] Thermal evaporation of metal onto an organic surface followed by further organic deposition has been used to incorporate MNPs in organic devices.[10] However, in this case, the particle size and distribution cannot be controlled, and the evaporated, energetic metal atoms can degrade the underlying organic material, as is discussed in this paper. For solution-processed organic materials, typically polymers, a MNP-embedded organic layer can be easily formed by spin-coating a polymer solution blended with pre-synthesized MNPs.[5,11] The drawbacks of this method are that (i) MNPs are distributed throughout the polymer layer so that their position cannot be accurately controlled, and (ii) surfactants attached to the MNPs to prevent their aggregation in the polymer matrix may have adverse effects on the electrical properties, such as charge transport and separation.[12]

Here, Au-NP-embedded OLEDs where Au NPs with a geometric mean diameter of 4.0 nm are incorporated in a specific plane in the HTL using an aerosol technique is dealt with. The incorporation of the Au NPs in the HTLr composed of *N,N'*-bis(naphthalen-1-yl)-*N,N'*-bis(phenyl)benzidine (NPB) is achieved by the generation of charged Au NP aerosols by spark

discharge[13] and their deposition on an electrically biased substrate coated with NPB, followed by the deposition of a capping NPB layer. The aerosol technique enables to locate Au NPs with a precise control of the vertical (perpendicular to the substrate surface) position within the NPB layer, while minimizing possible damage to the NPB. The Au-NP-embedded OLEDs fabricated by the aerosol technique present increased external quantum efficiencies, compared with the control device without Au NPs. Furthermore, the precise control of the Au NP position achieved by the aerosol technique enables to find an optimum vertical position of the Au NPs within the NPB layer, in which case the external quantum efficiency is 38% larger than that of the control device. Semi-quantitative analysis shows that the efficiency increase, which is accompanied by a slight increase in driving voltage, is attributed to the improved electron-hole recombination probability caused by the electrostatic effects of holes trapped in the Au NPs. The results in this chapter are mainly adapted from the publication by Sung et al.[14]

3.2. Experimental Methods

3.2.1. Fabrication of Gold Nanoparticle-Embedded OLEDs

Figure 3.1 illustrates the structure of OLEDs studied in this work, which is an archetype bilayer fluorescent device with Au NPs incorporated in the HTL composed of NPB. The structure is: ITO / 50 nm NPB HTL / 50 nm

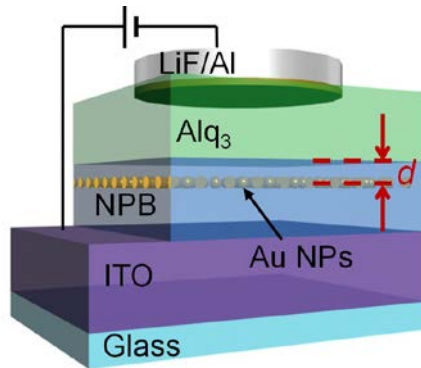


Figure 3.1 Schematic structure of the Au-NP-embedded OLED, where Au NPs in the hole transport layer composed of NPB is positioned d away from the Alq₃-NPB interface.

tris-(8-hydroxyquinoline) aluminum (Alq₃) electron-transport and light-emitting layer / 0.5 nm lithium fluoride (LiF) / 100 nm Al, where Au NPs are placed in the HTL d away from the NPB-Alq₃ interface. To examine the effect of the Au NPs on the device performance, we characterized the performance of OLEDs with different d 's (= 10, 20, 30, or 40 nm) and densities (N 's) of the Au NPs of the Au NPs, while fixing the HTL thickness at 50 nm.

The generation and deposition of the Au NPs were performed in a homemade system consisting of a SDG and an ESP, whose schematics is shown in Figure 3.2. The SDG-ESP system was installed inside a nitrogen glove box connected to a vacuum thermal evaporator for the organic and electrode depositions so that the samples were kept in an inert environment throughout the entire fabrication processes. For comparison, we also fabricated Au-NP-embedded OLEDs, where Au NPs were formed in

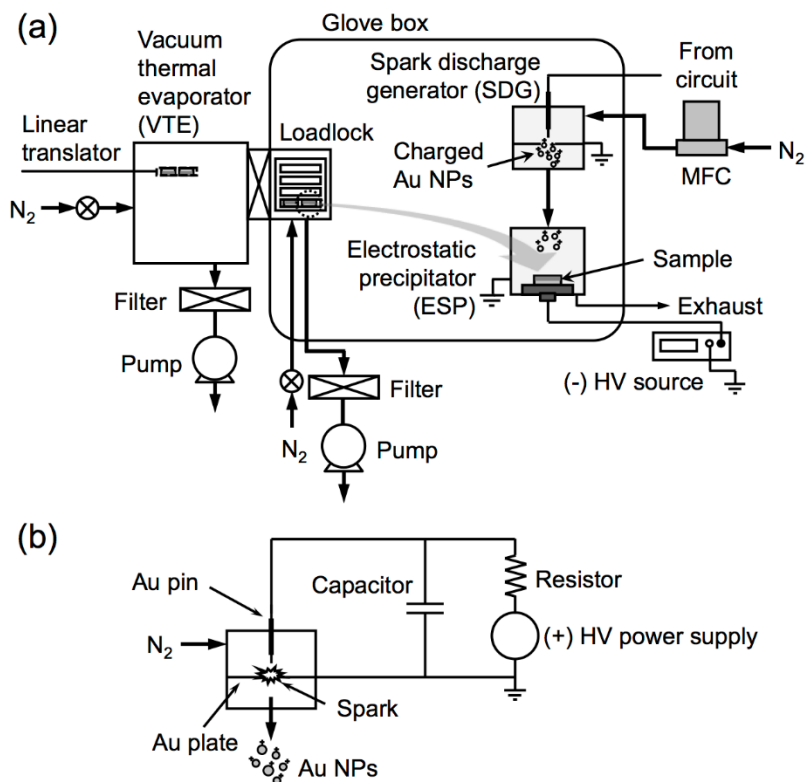


Figure 3.2 (a) Schematic illustration of the experimental setup to fabricate Au-NP-embedded OLEDs consisting of a conventional vacuum thermal evaporator and a homemade SDG-ESP system. (b) Electric circuit used to control spark discharge in the SDG.

the NPB layer by depositing an ultrathin Au layer by vacuum thermal evaporation. Various Au deposition conditions, such as deposition rate (0.05, 0.1, 0.2, and 0.5 \AA s^{-1}) and thickness (0.5, 1.0, 2.0, 3.0, and 5.0 \AA), were tested. Since the thickness values, as measured by a quartz crystal sensor, are very small, they represent the total mass of deposited Au, rather than the

actual thickness of the Au “layer”. Hereafter, we refer to the OLEDs with Au NPs deposited by the SDG-ESP system and the vacuum thermal evaporator as the SDG OLED and the VTE OLED, respectively.

Devices, whose active area is a circle with a diameter of 2.0 mm, were fabricated on commercially obtained ITO-coated glass substrates ($15 \Omega \text{ sq}^{-1}$, $25 \text{ mm} \times 25 \text{ mm}$), which were sequentially cleaned in an ultrasonic bath with detergent, de-ionized water, acetone, and isopropyl alcohol, followed by ultraviolet/ozone (UVO) treatment for 30 min. The Au NPs for the Au-NP-embedded OLEDs were fabricated and deposited using the homemade SDG-ESP system, as shown in Figure 3.2a. The Au-NP-embedded OLED with $d = x \text{ nm}$ was fabricated by the following procedure: (i) an NPB layer with a thickness of $(50 - x) \text{ nm}$ was deposited on an ITO-coated glass substrate by vacuum thermal evaporation; (ii) the substrate was transferred to the SDG-ESP system, where Au NPs were generated in the SDG, and then deposited on the NPB layer in the ESP; (iii) the sample was transferred back into the vacuum thermal evaporator, where a $x\text{-nm}$ -thick NPB layer was deposited, followed by deposition of the rest of the organic and electrode layers. The base pressure of the vacuum thermal evaporator was lower than 1.0×10^{-6} Torr. The SDG consisted of a cylindrical chamber with an inner diameter of 30 mm and a height of 37 mm, a pin electrode made of a gold wire with a diameter of 1.0 mm (Sigma Aldrich), and a plate electrode made of a 0.25-mm-thick gold foil with a size of $5 \text{ mm} \times 5 \text{ mm}$ (Sigma Aldrich). The plate electrode had a 1-mm-diameter exit hole at the center, which was aligned with the axis of the pin electrode. The tip of the pin was located 1 mm above the plate electrode. The generation of the Au NPs in the SDG was controlled

by varying the frequency and energy of spark generated between the pin and plate electrodes using a simple RC circuit consisting of a positive high-voltage power supply (AU-10N3-L, Matsusada), a 2-nF capacitor, and a 20-M Ω resistor (Figure 3.2b). The plate electrode was grounded, and the electric potential at the pin electrode was 5.0 kV. The Au NPs generated by spark discharge between the electrodes were inherently bipolarly charged, and were transported through the exit hole to be delivered to the ESP by a nitrogen carrier gas with a flow rate of 2.0 L min⁻¹. The ESP was composed of a grounded cylindrical chamber with an inner diameter of 52 mm and a height of 47 mm, and a bottom electrode made of copper connected to a negative high-voltage power supply (AU-10N3-L, Matsusada). An ITO-coated glass substrate coated with an NPB layer was placed on the bottom electrode in the ESP, with the ITO connected electrically to the electrode. When the bottom electrode was negatively biased, the positively charged one among the bipolarly charged Au NPs fed into the ESP were electrostatically guided to and deposited on the substrate surface. The magnitude of the negative potential⁷ at the bottom electrode was chosen to be high (= -5.5 kV) to form a non-uniform electric field distribution in ESP so that various values of N were obtained across a substrate in a single deposition.

3.2.2. Characterization

Size distribution of Au NPs generated from the SDG was obtained by measurement of the projected area equivalent diameters using high-resolution transmission electron microscope (HRTEM; JEM ARM 200F, JEOL) images. For the HRTEM measurement, Au NPs were deposited using

the SDG-ESP system on a molybdenum mesh coated with a carbon film. The scanning electron microscope (SEM) images of Au NPs deposited on ITO layers were obtained using a Zeiss SUPRA 55 VP.

Cross-sectional TEM measurements of the OLEDs were performed using a JEOL JEM-2100F, and TEM specimens were prepared using a focused ion beam instrument (Nova 600 NanoLab, FEI). These specimens were also used to obtain scanning TEM (STEM) images using the same TEM apparatus. Current density–voltage (J – V) and external quantum efficiency–current density (η_{ext} – J) characteristics were obtained using a Keithley 2400 source meter and a calibrated silicon photodiode (818-SL, Newport). Photoluminescence (PL) spectra were measured using a fluorescence spectrometer (FS-2, Sinco) with 430 nm excitation at 25° to the sample surface obtained using a monochromator and a xenon lamp. The PL was collected at 90° to the excitation beam. Pumping of the samples and collection of the PL were both carried out through the ITO side. A time-correlated single-photon-counting system was used for measurements of spontaneous fluorescence decay profiles. As an excitation light source, we used a mode-locked Ti:sapphire laser (Mai Tai BB, Spectra-Physics) which provides ultrashort pulses [80 fs, full width at half maximum (FWHM)] with a high repetition rate (80 MHz). This high repetition rate was decreased to $1\text{M} \sim 800\text{ kHz}$ using a homemade pulse-picker. The pulse-picked output pulse was frequency-doubled by a 1-mm-thick BBO crystal (EKSPA). The fluorescence was collected by a microchannel plate photomultiplier tube (MCP-PMT; R3809U-51, Hamamatsu) with a thermoelectric cooler (C4878, Hamamatsu) connected to a TCSPC board (SPC-130, Becker&Hickel). The

overall instrumental response function was about 25 ps (FWHM). A vertically polarized pump pulse by a Glan-laser polarizer was irradiated onto samples, and a sheet polarizer, set at an angle complementary to the magic angle (54.7°), was placed in the fluorescence collection path to obtain polarization-independent fluorescence decays. All electrical and optical measurements were performed under ambient conditions without device encapsulation.

3.3. Results and Discussion

3.3.1. Characteristics of Gold Nanoparticle Layers

The geometric mean diameter and standard deviation of the Au NPs generated in the SDG were determined to be 4.0 and 1.5 nm, respectively, from the particle size distribution (Figure 3.3), which was obtained by analyzing the HRTEM images. The values of four different surface coverage density provided by the SDG-ESP system were determined to be approximately 200, 920, 5150, and 8400 particles per μm^2 , respectively, from the SEM images in Figure 3.3.

3.3.2. Device Characteristics of Gold Nanoparticle-Embedded OLEDs

Figure 3.4 shows the J - V and η_{ext} - J characteristics of the SDG OLEDs with $N \approx 5150 \mu\text{m}^{-2}$ and $d = 10, 20, 30, \text{ or } 40 \text{ nm}$. Here, $N \approx 5150 \mu\text{m}^{-2}$ among

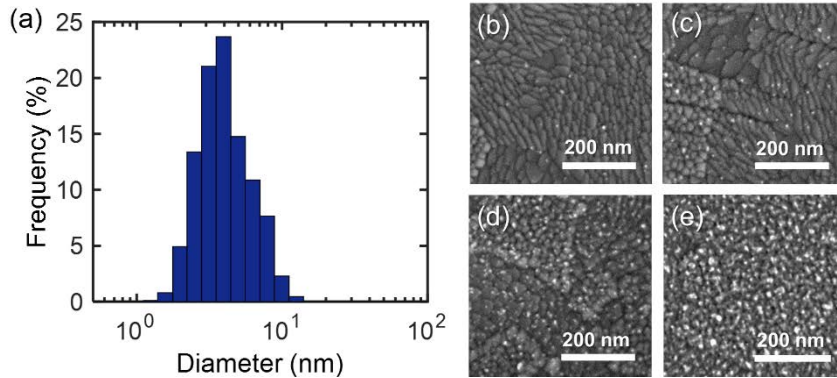


Figure 3.3 (a) The size distribution of Au NPs generated in the spark discharge generator, which was obtained by analyzing HRTEM images. The geometric mean diameter and standard deviation of the Au NPs were found to be 4.0 and 1.5 nm, respectively. (b) - (e) The SEM images of the Au NPs deposited on ITO substrates by the homemade aerosol deposition system shown in Figure 3.1. The particle density corresponds to (b) 200, (c) 920, (d) 5150, and (e) 8400 μm^{-2} on average.

four different N s was chosen to be tested for the position effect of Au NPs because the greatest device performance was achieved from the SDG OLED with this N value (data not shown). Also shown are the characteristics of the VTE OLED with $d = 20$ nm, incorporating a 3.0-Å-thick Au “layer” deposited at a rate of 0.2 \AA s^{-1} . The value of N for the VTE OLED was estimated to be $36,000 \mu\text{m}^{-2}$ from the “thickness” of the Au NP layer and the average particle size. Throughout the entire current density range, the driving voltage of the VTE OLED was significantly increased compared to that of the control device without Au NPs. For example, the voltage corresponding

to $J = 20 \text{ mA cm}^{-2}$ for the VTE OLED was 12.3 V, which is by a factor of 2.5 larger than that of the control device (= 4.90 V). In contrast, the SDG OLEDs exhibited remarkably different characteristics compared to the VTE OLED; although the SDG OLEDs also showed higher driving voltages than the control device, the extent of increase ranged from 10% to 55% depending on d , much smaller than that for the VTE OLED (150%). The large increase in voltage for the VTE OLED is likely due to severe degradation in the hole transporting property of the NPB layer caused by energetic, thermally evaporated Au atoms. It may be argued that this contrast is due to the fact that the surface coverage of the Au NPs in the VTE OLED ($\approx 25\%$) is much larger than that of the SDG OLED ($\approx 6.5\%$). However, all other VTE OLEDs with different deposition rates and thicknesses of Au NP layers also showed a similar extent of increase in driving voltage (data not shown). For example, the VTE OLED with a 0.5-Å-thick Au layer deposited at a rate of 0.2 Å s^{-1} had, at $J = 20 \text{ mA cm}^{-2}$, a driving voltage that is 110% larger than that of the control device. In addition, severe reductions in η_{ext} were observed in all VTE OLEDs: the smallest reduction was observed when the Au layer thickness was the smallest (= 0.5 Å), whose η_{ext} was approximately 75% of that of the control OLED, and the values of η_{ext} for the VTE OLEDs with a thicker Au NP layer were similar ($< 15\%$ of η_{ext} of the control device) to that of the VTE OLED shown in Figure 3.4b. In contrast, all SDG OLEDs exhibited enhanced η_{ext} compared to the control device: the values of η_{ext} at $J = 50 \text{ mA cm}^{-2}$ for those with $d = 10, 20, 30$ and 40 nm were, respectively, 1.40, 1.58, 1.56, and 1.45%, which correspond to 22, 38, 36, and 27% enhancement, respectively, compared to the control device ($\eta_{\text{ext}} = 1.15\%$ at $J = 50 \text{ mA cm}^{-2}$).

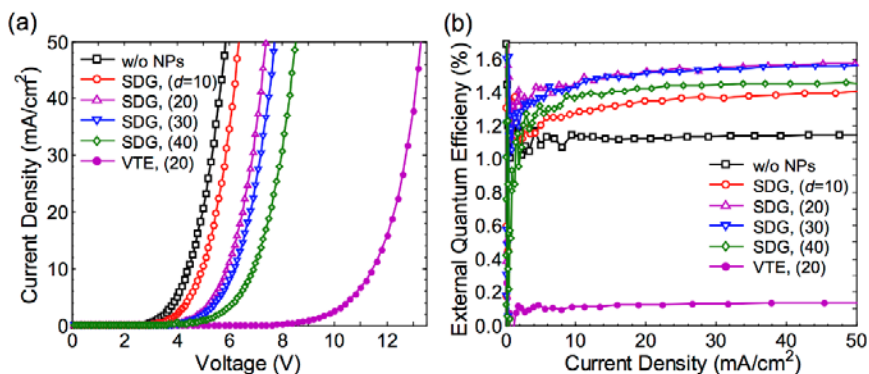


Figure 3.4 (a) Current density vs. voltage characteristics of the SDG OLEDs with different d 's ($d = 10, 20, 30$ or 40 nm), and the VTE OLED (“thickness” = 3.0 \AA , deposition rate = 0.2 \AA/s) with $d = 20$ nm. **(b)** External quantum efficiency vs. current density characteristics of the devices shown in (a).

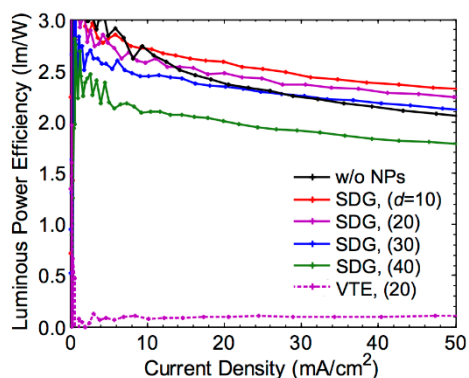


Figure 3.5 (a) Luminous power efficiency vs. current density characteristics of the SDG OLEDs ($N \approx 5150 \mu\text{m}^2$) with different d 's ($d = 10, 20, 30$ or 40 nm), and the VTE OLED ($N \approx 36000 \mu\text{m}^2$, “thickness” = 3.0 \AA , deposition rate = 0.2 \AA/s) with $d = 20$ nm.

²). Here, it should be noted that the largest η_{ext} was obtained for the SDG OLED with $d = 20$ nm. Due to the increase in driving voltage, the enhancement in luminous power efficiency was smaller than that in η_{ext} , maximized at 13% for the device with $d = 10$ nm exhibiting the smallest increase in V as shown in Figure 3.5.

To investigate how the two methods for positioning Au NPs in the NPB layer resulted into the remarkably different device characteristics, cross-sectional TEM measurements were carried out. Figure 3.6a and Figure 3.6b show, respectively, the TEM images of the SDG OLED ($N \approx 5,150 \mu\text{m}^{-2}$) and the VTE OLED ($N \approx 36,000 \mu\text{m}^{-2}$, “thickness” = 3.0 \AA , deposition rate = 0.2 \AA s^{-1}), both with $d = 20$ nm. To avoid misinterpretation of the TEM images due to the roughness of the ITO surface, a Si substrate was used instead of the ITO-coated glass substrate. As shown in Figure 3.6a and Figure 3.6b, in both SDG and VTE cases, the Au NPs formed a “layer” at a specific, desired location – approximately 30 nm away from the Si–NPB interface. The Au NP layer in the VTE OLED is different from that in the SDG OLED in that it was composed of larger number of smaller NPs. Furthermore, Figure 3.6b shows that the small Au NPs in the VTE OLED penetrated into the NPB layer as marked by black arrows. The corresponding STEM image of the VTE OLED in Figure 3.6d clearly shows the penetration of the Au NPs into the underlying NPB layer, which is not observed in the STEM image of the SDG OLED in Figure 3.6c. This is not unexpected,[15] since the Au atoms boiled off from a crucible or boat during vacuum thermal evaporation are ballistically transported to the substrate, with a mean free path of the order of a few meters at the pressure of $\sim 1.0 \times 10^{-6}$ Torr, impinging on the organic

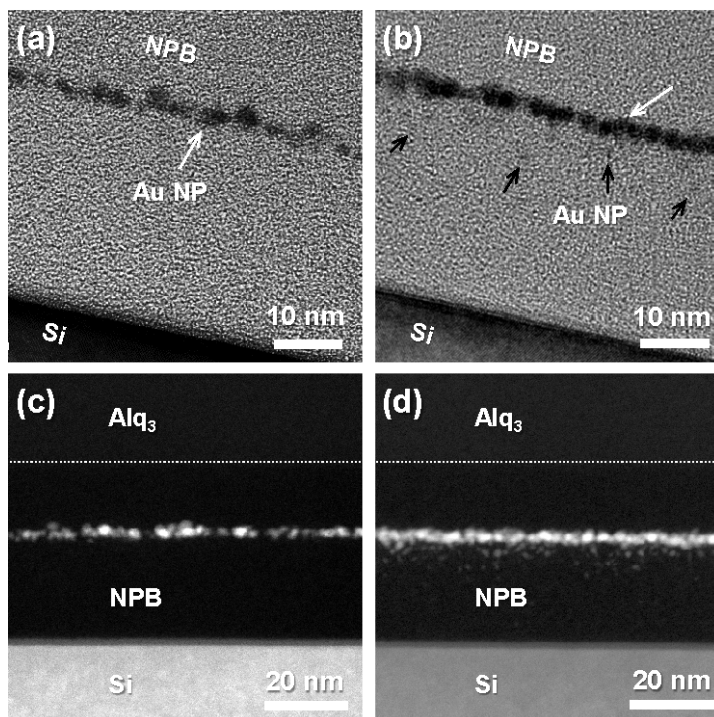


Figure 3.6 Cross-sectional TEM images of (a) the SDG OLED and (b) the VTE OLED structures, both with $d = 20$ nm, deposited on Si substrates. For the VTE OLED, the “thickness” and the deposition rate of the Au layer are 3.0 \AA and 0.2 \AA/s , respectively. (c) and (d) are STEM images of the same samples in (a) and (b), respectively. In (b), small Au NPs marked by black arrows were formed at $d > 20$ nm, indicating that thermally evaporated Au atoms have penetrated into the underlying NPB, which is more clearly shown in (d).

layer with a kinetic energy similar to $3/2 kT \sim 0.4 \text{ eV}$, where k is Boltzmann’s constant and T is the boiling temperature of Au. Since this value is comparable to a van der Waals bond energy of typical organic

semiconductors,[16] thermally evaporated Au atoms in the VTE OLED are likely to degrade the hole transport properties of the NPB layer, leading to the significant increase in driving voltage as shown in Figure 3.4a. The situation is quite different in the room temperature deposition of Au NP layers via the SDG. The impinging velocity (v) of the NPs is estimated to be 1.5 m s^{-1} , which is determined by balancing the electrostatic and fluid frictional forces: [17]

$$v = \frac{neEC_c}{3\pi\mu d_p} \quad (3.1)$$

where n ($= 1$) is the number of elementary charges, e is the electron charge, E ($= 1.07 \times 10^5 \text{ V/m}$) is the electrical field strength, C_c ($= 57.9$) is the Cunningham correction factor, μ ($= 1.78 \times 10^{-5} \text{ kg s}^{-1} \text{ m}^{-1}$) is the viscosity and d_p ($= 4 \text{ nm}$) is the particle diameter. The resulting kinetic energy of an Au NP is approximately 4.4 meV , which is two orders of magnitude smaller than that of the thermally evaporated Au atom. Thus, although the size of Au NPs are larger than that in the VTE OLED, the adverse impact on the underlying organic is minimized in the aerosol deposition of Au NPs. As a result, the penetration of the Au NPs into the NPB layer is not observed in the TEM images, and the increase in driving voltage of the SDG OLED is much smaller than that of the VTE OLED. In addition, unlike in vacuum thermal evaporation, the independent and precise control of the size, density, and vertical location of Au NPs is possible in the deposition of Au NPs by the aerosol method. This unique feature of the aerosol technique can be exploited to control the electrical and/or optical properties of organic electronic and

optoelectronic devices, and our results are, to our knowledge, the first demonstration that the performance of an OLED is maximized by incorporating metal NPs without surfactants in a specific plane in the interior of an OLED.

3.3.3. Photoluminescence Analysis

To investigate how Au NPs embedded in different locations affect the OLED performance, we consider the following general expression for the external quantum efficiency:[18]

$$\eta_{\text{ext}} = \eta_{\text{out}} \varphi \chi \gamma \quad (3.2)$$

where η_{out} is the light extraction efficiency, φ is the probability that an emissive exciton actually produces a photon, χ is the probability that an exciton created by electron-hole recombination is emissive as determined by the spin selection rules,[19] and γ is the probability that injected charge carriers recombine to form excitons. In typical Alq₃-NPB OLEDs, γ is limited by holes that reach the cathode without recombining with electrons in the Alq₃ layer.[20] One can view that the first two terms on the right hand side of Eq. (2), η_{out} and φ , concern with optical or electromagnetic processes, while the last two terms, χ and γ , are related to electrical processes.

To investigate the optical aspects, we performed PL measurements on samples whose structures were identical to the SDG OLEDs with different d 's ($d = 10, 20, 30$ or 40 nm), except that the 50-nm-thick Alq₃ layer in the SDG OLEDs was replaced with a bilayer of 5-nm-thick Alq₃ (on the NPB

side) and 45-nm-thick NPB (on the Al side). The samples were illuminated with a monochromatic light whose wavelength ($\lambda = 430$ nm) was chosen to excite Alq₃ only, confining the region of exciton generation to the vicinity of the Alq₃-NPB interface as in the electrically pumped SDG OLEDs. Figure 3.7a shows the PL intensities measured using a microscope objective lens with a numerical aperture of 0.2. Except the sample with $d = 10$ nm, the PL intensities were very similar to that of the control sample without Au NPs. Considering that the distribution of the NPs was rather sparse (one particle in 194 nm² on average) and that the transmission of the NPB layer at $\lambda = 430$ nm was reduced by less than 2% upon the incorporation of the NPs, the number of Alq₃ excitons generated in each sample per unit time is expected to be nearly the same. This means that the PL intensities shown in Figure 3.7a represent the relative magnitudes of $\eta_{\text{out}} \phi$ for the SDG OLEDs. Moreover, time-resolved PL decays of Alq₃ in the samples were measured using time-correlated single photon counting (Figure 3.7b). The observed PL decay profiles monitored at $\lambda = 600$ nm with photoexcitation at $\lambda = 430$ nm can be fit well as a single exponential decay with time constants of 13.4, 14.3, and 14.1 ns for Alq₃ in the samples with $d = 20, 30,$ and 40 nm, respectively. These values are similar to that of the control sample without Au NPs (= 14.0 ns). In the case of Alq₃ in the samples with $d = 10$ nm, however, the observed excited-state lifetime was decreased to 9.9 ns. Therefore, we conclude that the decrease in $\eta_{\text{out}} \phi$ of the SDG OLED with $d = 10$ nm was primarily due to decreased ϕ , which was caused by the metal-induced quenching [21,22] arising from decreased exciton-to-NP distances in this sample. This conclusion is further supported by our observation that

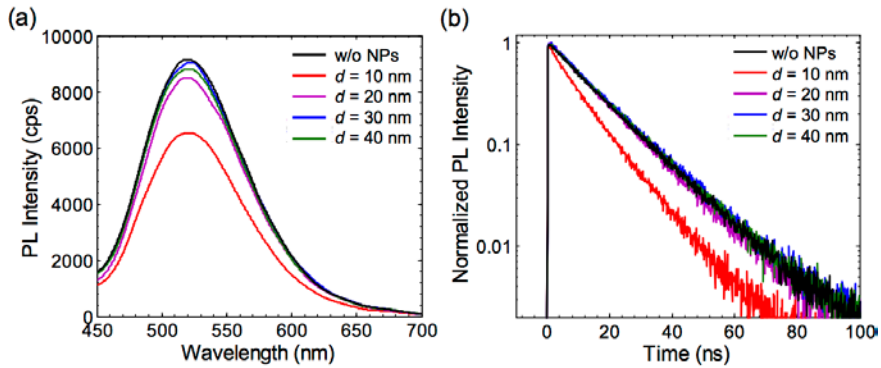


Figure 3.7 (a) Photoluminescence spectra and (b) transient photoluminescence decay profiles of the samples whose structures were identical to the SDG OLEDs with different d 's ($d = 10, 20, 30$ or 40 nm), except that the 50-nm-thick Alq₃ layer in the SDG OLEDs was replaced with a bilayer of 5-nm-thick Alq₃ (on the NPB side) and 45-nm-thick NPB (on the Al side). In (a) and (b), the excitation wavelength was 430 nm, while the photoluminescence decay profiles were detected at 600 nm.

the angular distributions of Alq₃ emission from all SDG OLEDs were nearly identical to that of the control device, suggesting that η_{out} was not affected by the small, sparsely distributed Au NPs.

3.3.4. Charge Transport Analysis

The PL measurements presented in Figure 3.7 do not provide any explanation for the η_{ext} enhancement of the SDG OLEDs, but rather show that the presence of Au NPs adversely affected the optical processes in the SDG OLED with $d = 10$ nm. Using the measured η_{ext} values shown in Figure

3.4b and the relative magnitudes of $\eta_{\text{out}} \phi$ determined from the PL intensities, the relative change in γ depending on d can be extracted from Equation (3.2). Figure 3.8a, where η_{ext} , $\eta_{\text{out}} \phi$, and γ normalized to the corresponding values of the control device are plotted as functions of d , shows that the enhancements in η_{ext} of the SDG OLEDs are attributed to increases in γ . Here, we assume that χ is constant for all devices, since the presence of Au NPs is not expected to affect the spin-related aspect of exciton formation process and the probability of intersystem crossing.[23] As d decreases from 40 nm, the value of γ , which is larger for all SDG OLEDs than that of the control device, monotonically increases. Owing to this increase in γ , η_{ext} increases until $d = 20$ nm, beyond which η_{ext} decreases due to the increase in metal-induced quenching of Alq₃ excitons. The value of η_{ext} for the SDG OLED with $d = 10$ nm remains larger than that of the control device, since the relative increase in γ exceeds the relative decrease in $\eta_{\text{out}} \phi$.

To investigate how the Au NPs affect γ , we examined the effect of the Au NPs on the hole transport properties of the NPB layer by measuring the J - V characteristics of hole-only devices comprising: glass / ITO / 100 nm NPB / 100 nm Al, where Au NPs ($N \approx 5,150 \mu\text{m}^{-2}$) were embedded in the NPB layer using the SDG-ESP system under the same condition as that used to fabricate the SDG OLEDs. The distance between the Au NP layer and the ITO-NPB interface, d_{ITO} , was chosen to be the same as that in the SDG OLEDs ($d_{\text{ITO}} = 10, 20, 30, \text{ or } 40$ nm). The J - V characteristics compared with that of the control hole-only device without Au NPs are shown in Figure 3.8b. The driving voltages of all SDG hole-only devices were higher than that of the control device throughout the entire current density range. This is

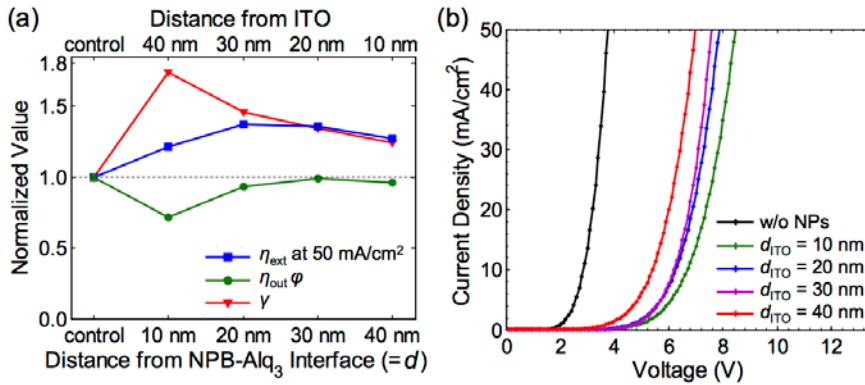


Figure 3.8 (a) Plots of η_{ext} , $\eta_{\text{out}} \phi$, and γ normalized to the corresponding values of the control device as functions of d . (b) Current density vs. voltage characteristics of hole-only devices comprising: glass / ITO / 100 nm NPB / 100 nm Al, where Au NPs were embedded in the NPB layer using the SDG-ESP system. The distance between the Au NP layer and the ITO–NPB interface, d_{ITO} , was chosen to be the same as that in the SDG OLEDs ($d_{\text{ITO}} = 10, 20, 30,$ or 40 nm).

attributed to hole trapping in the Au NPs since the Fermi level of Au is slightly above the highest occupied molecular orbital level of NPB, as was previously reported for poly(9,9'-dioctylfluorene) embedded with Au NPs.[24] In addition to hampering hole transport in the NPB layer, the holes trapped in the Au NPs possibly decrease the local electrostatic field at the anode, decreasing the rate of hole injection into NPB. This occurs to a greater extent as the Au NPs are located closer to the anode, consistent with the observation that the driving voltages of the SDG hole-only devices increase with decreasing d_{ITO} (Figure 3.8b).

The same dependency of driving voltage on the location of the Au NPs, that is, the increase in driving voltage as the Au NPs are located closer to the anode, was observed in the SDG OLEDs, as shown in Figure 3.4a. This similarity indicates that the change in the J - V characteristics of the SDG OLEDs is also primarily due to the decreased hole current in the NPB layer upon the introduction of the Au NPs. Given that the control and the SDG OLEDs are hole-rich, that is, γ is limited by holes that reach the cathode without forming excitons in the Alq₃ layer,[25,26] which is confirmed by the fact that there is no NPB emission in these devices, we expect that the enhancement in γ increases as the hole current at the NPB–Alq₃ interface decreases. However, the opposite trend was observed in Figure 3.8a: γ monotonically increases with decreasing d , which can be explained by the following. As the Au NPs, which are positively charged due to trapped holes, are located closer to the NPB–Alq₃ interface, the electric field near that interface increases. This in turn increases the electron density near the NPB–Alq₃ interface, resulting into increased γ . Therefore, we conclude that the enhancement in γ of the SDG OLEDs is attributed to the combination of the following effects of the charged Au NPs: the decrease in hole injection at the anode, the decrease in the effective hole mobility in the NPB layer, and the increase in the electron density near the NPB–Alq₃ interface. The monotonic increase in γ with decreasing d shown in Figure 3.8a indicates that the latter effect is dominant over the former two. The effects of the Au NPs with trapped holes on the hole injection at the anode and the electron density near NPB–Alq₃ interface are schematically shown in Figure 3.9.

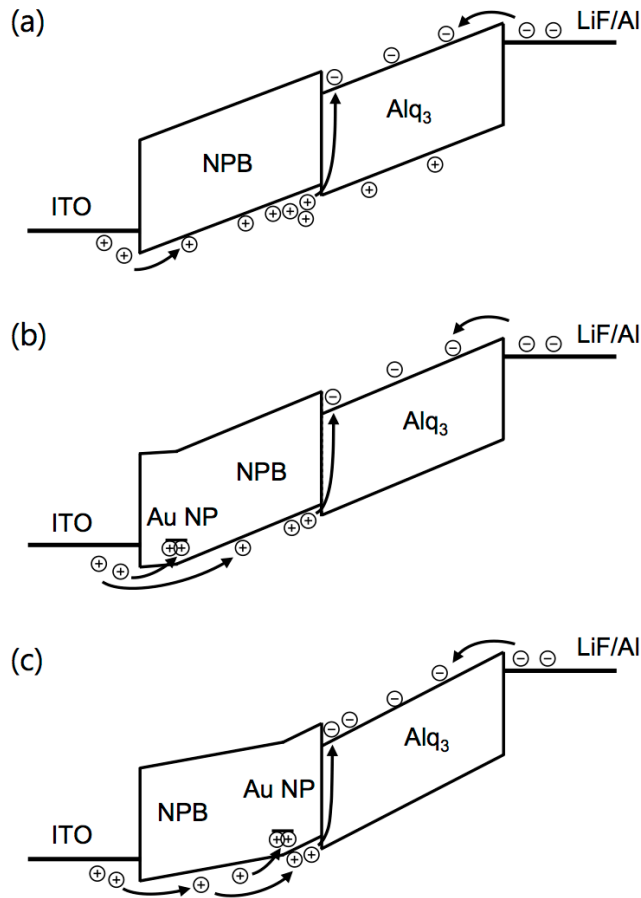


Figure 3.9 Schematic energy-level diagrams. (a) Control device without Au NPs, (b) SDG OLED with $d = 40$ nm. The reduced electric field at the anode due to trapped holes in the Au NPs decreases the hole current, leading to an increased probability of exciton formation. (c) SDG OLED with $d = 10$ nm. As the Au NPs are located closer to the Alq₃-NPB interface, the electrostatic field in the Alq₃ near that interface increases, resulting into a further increase in the exciton formation probability.

3.4. Conclusion

An aerosol method has been employed to incorporate Au NPs in a HTL, composed of NPB, of a fluorescent Alq₃-based OLED with a precise control of the vertical (perpendicular to the substrate surface) position of the NPs within NPB. Being a dry, room-temperature process, the technique enables to embed Au NPs without surfactants in an organic device, while minimizing possible damage to organic materials. This has enabled to increase the external quantum efficiency of the OLED by 38% compared with the control device without Au NPs, by changing the position of the Au NPs. Our optical and electrical characterizations show that the external quantum efficiency increase is attributed to the improved electron-hole recombination probability caused by the electrostatic effects of holes trapped in the Au NPs. Although the effects of Au NPs in this demonstration are mainly electrical due to their small (~ 4 nm in diameter) sizes, the unique attributes of aerosol technology, such as the ability to deposit mono- or poly-disperse NPs, composed of single or multiple materials with core or core/shell structures, [27] and to create three-dimensional NP assemblies with lateral patterning capabilities,[28,29] may offer opportunities for demonstrating organic-based electronic and optoelectronic devices with greater performance enhancement or novel functionalities.

3.5. References

- [1] J.C. Scott, L.D. Bozano, "Nonvolatile memory elements based on organic materials", *Adv. Mater.*, **19**, 1452-1463 (2007)
- [2] M.-K. Kwon, J.-Y. Kim, B.-H. Kim, I.-K. Park, C.-Y. Cho, C.C. Byeon, S.-J. Park, "Surface-plasmon-enhanced light-emitting diodes", *Adv. Mater.*, **20**, 1253-1257 (2008)
- [3] A. Fujiki, T. Uemura, N. Zettsu, M. Akai-Kasaya, A. Saito, Y. Kuwahara, "Enhanced fluorescence by surface plasmon coupling of Au nanoparticles in an organic electroluminescence diode", *Appl. Phys. Lett.*, **96**, (2010)
- [4] D. Derkacs, S.H. Lim, P. Matheu, W. Mar, E.T. Yu, "Improved performance of amorphous silicon solar cells via scattering from surface plasmon polaritons in nearby metallic nanoparticles", *Appl. Phys. Lett.*, **89**, 093103-093103 (2006)
- [5] F.-C. Chen, J.-L. Wu, C.-L. Lee, Y. Hong, C.-H. Kuo, M.H. Huang, "Plasmonic-enhanced polymer photovoltaic devices incorporating solution-processable metal nanoparticles", *Appl. Phys. Lett.*, **95**, 013305 (2009)
- [6] K.R. Catchpole, S. Pillai, "Surface plasmons for enhanced silicon light-emitting diodes and solar cells", *J. Lumin.*, **121**, 315-318 (2006)
- [7] L.S. Hung, C.H. Chen, "Recent progress of molecular organic electroluminescent materials and devices", *Mat. Sci. Eng. R*, **39**, 143-222 (2002)
- [8] P. Peumans, A. Yakimov, S.R. Forrest, "Small molecular weight

organic thin-film photodetectors and solar cells", *J. Appl. Phys.*, **93**, 3693-3723 (2003)

[9] G. Li, R. Zhu, Y. Yang, "Polymer solar cells", *Nat Photon*, **6**, 153-161 (2012)

[10] B.P. Rand, P. Peumans, S.R. Forrest, "Long-range absorption enhancement in organic tandem thin-film solar cells containing silver nanoclusters", *J. Appl. Phys.*, **96**, 7519-7526 (2004)

[11] J.-L. Wu, F.-C. Chen, Y.-S. Hsiao, F.-C. Chien, P. Chen, C.-H. Kuo, M.H. Huang, C.-S. Hsu, "Surface plasmonic effects of metallic nanoparticles on the performance of polymer bulk heterojunction solar cells", *ACS Nano*, **5**, 959-967 (2011)

[12] D.S. Ginger, N.C. Greenham, "Photoinduced electron transfer from conjugated polymers to CdSe nanocrystals", *Phys. Rev. B*, **59**, 10622-10629 (1999)

[13] K. Han, W. Kim, J. Yu, J. Lee, H. Lee, C. Gyu Woo, M. Choi, "A study of pin-to-plate type spark discharge generator for producing unagglomerated nanoaerosols", *J. Aerosol Sci.*, **52**, 80-88 (2012)

[14] H. Sung, J. Lee, K. Han, J.-K. Lee, J. Sung, D. Kim, M. Choi, C. Kim, "Controlled positioning of metal nanoparticles in an organic light-emitting device for enhanced quantum efficiency", *Org. Electron.*, **15**, 491-499 (2014)

[15] A.C. Dürr, F. Schreiber, M. Kelsch, H.D. Carstanjen, H. Dosch, "Morphology and thermal stability of metal contacts on crystalline organic thin films", *Adv. Mater.*, **14**, 961-963 (2002)

[16] B. Masenelli, F. Tournus, P. Mélinon, X. Blase, A. Perez, M.

- Pellarin, M. Broyer, A.M. Flank, P. Lagarde, "Si-C60 bond in cluster-based materials", *Surf. Sci.*, **532-535**, 875-879 (2003)
- [17] W.C. Hinds, "Aerosol technology: properties, behavior, and measurement of airborne particles"(1999), *John Wiley & Sons*,
- [18] C. Adachi, M.A. Baldo, M.E. Thompson, S.R. Forrest, "Nearly 100% internal phosphorescence efficiency in an organic light-emitting device", *J. Appl. Phys.*, **90**, 5048-5051 (2001)
- [19] R.H. Friend, R.W. Gymer, A.B. Holmes, J.H. Burroughes, R.N. Marks, C. Taliani, D.D.C. Bradley, D.A.D. Santos, J.L. Bredas, M. Logdlund, W.R. Salaneck, "Electroluminescence in conjugated polymers", *Nature*, **397**, 121-128 (1999)
- [20] C.-a. Di, G. Yu, Y. Liu, X. Xu, Y. Song, D. Zhu, "High-efficiency low operation voltage organic light-emitting diodes", *Appl. Phys. Lett.*, **90**, 133508-133503 (2007)
- [21] E. Dulkeith, M. Ringler, T.A. Klar, J. Feldmann, A. Muñoz Javier, W.J. Parak, "Gold nanoparticles quench fluorescence by phase induced radiative rate suppression", *Nano Lett.*, **5**, 585-589 (2005)
- [22] G. Schneider, G. Decher, N. Nerambourg, R. Praho, M.H.V. Werts, M. Blanchard-Desce, "Distance-dependent fluorescence quenching on gold nanoparticles ensheathed with layer-by-layer assembled polyelectrolytes", *Nano Lett.*, **6**, 530-536 (2006)
- [23] C.-J. Sun, Y. Wu, Z. Xu, B. Hu, J. Bai, J.-P. Wang, J. Shen, "Enhancement of quantum efficiency of organic light emitting devices by doping magnetic nanoparticles", *Appl. Phys. Lett.*, **90**, 232110-232113 (2007)
- [24] J.H. Park, Y.T. Lim, O.O. Park, J.K. Kim, J.-W. Yu, Y.C. Kim,

"Polymer/gold nanoparticle nanocomposite light-emitting diodes: enhancement of electroluminescence stability and quantum efficiency of blue-light-emitting polymers", *Chem. Mater.*, **16**, 688-692 (2004)

[25] S.L. Lai, M.Y. Chan, M.K. Fung, C.S. Lee, L.S. Hung, S.T. Lee, "Applications of Ytterbium in organic light-emitting devices as high performance and transparent electrodes", *Chem. Phys. Lett.*, **366**, 128-133 (2002)

[26] B. Jiao, Z. Wu, X. Yan, X. Hou, "Influence of the thickness of N,N'-Bis(naphthalene-1-yl)-N,N'-bis(phenyl) benzidine layer on the performance of organic light-emitting diodes", *Appl. Phys. A*, **98**, 239-243 (2010)

[27] C. Boissiere, D. Grosso, A. Chaumonnot, L. Nicole, C. Sanchez, "Aerosol route to functional nanostructured inorganic and hybrid porous materials", *Adv. Mater.*, **23**, 599-623 (2011)

[28] H. Kim, J. Kim, H. Yang, J. Suh, T. Kim, B. Han, S. Kim, D.S. Kim, P.V. Pikhitsa, M. Choi, "Parallel patterning of nanoparticles via electrodynamic focusing of charged aerosols", *Nat. Nanotechnol.*, **1**, 117-121 (2006)

[29] H. Lee, S. You, P.V. Pikhitsa, J. Kim, S. Kwon, C.G. Woo, M. Choi, "Three-dimensional assembly of nanoparticles from charged aerosols", *Nano Lett.*, **11**, 119-124 (2011)

Chapter 4.

Reliable Control of Doping Type and Doping Level of Graphene by Aerosol- Derived Metal Nanoparticles

4.1. Introduction

Graphene has attracted much interest due to its superior electrical, optical, chemical, and thermomechanical properties.[1-3] For the practical use of graphene in various fields such as energy, catalysis, electronics, and photonics, graphene doping that can tailor the electronic properties and chemical reactivity of graphene is of great technological importance.[4-6] For a decade, carrier doping control and p-n junction construction of graphene have been demonstrated by electrostatic gating and chemical treatment.[7-9] However, the electrostatic gating typically demands to apply a constant high electric field between the gate electrode and graphene, which is not desirable for certain applications. Also, the chemical doping shows little tunability and generates defects in the lattice, resulting in a reduced carrier mobility.[10,11]

A recent theoretical work has suggested that a metal layer absorbed on graphene surface can induce p- or n-type doping of graphene due to electron transfer between the metal and graphene driven by the work function difference.[12] Then, doping control of graphene by thermally evaporated thin metal films has been demonstrated.[13,14] However, when a metal layer is fabricated by thermal evaporation, metal islands grow and coalesce to form a thin film with increase in deposition thickness, which can influence on the doping property of graphene. For example, when the nominal decoration thickness of Al on graphene increased from 0.5, 1.0 to 1.5 nm, the Dirac point of the graphene was first shifted towards the negative direction and

shifted backwards again.[15] In other case, when graphene was decorated by thermally deposition of Au, the doping type of the graphene changed from n-type to p-type with increasing the deposition thickness of Au.[16] Meanwhile, metal NPs formed on graphene by solution process always tend to form aggregates with spatially non-uniform distribution.[17] Therefore, the established methods for doping graphene with metal NPs are not satisfactory in a precisely controlled manner.

Here, a new metal-graphene contact approach using aerosol-derived metal NPs is investigated to achieve a reliable control of doping type and doping level of graphene. Unlike the conventional thermal evaporation method, the aerosol technique enables to form spatially uniform distribution of metal NPs with consistent size and shape, as well as less damage to the underlying graphene due to the relatively low kinetic energy of the aerosol-driven metal NPs. Ag and Pt NPs with four different surface coverage density for each material type are used to decorate graphene. As a result, Ag NPs lead to a shift in Fermi energy (E_F) in the graphene from the valence band through the Dirac point to the conduction band, providing electron doping, while Pt NPs cause a shift of E_F further into the valence band, resulting in hole doping. The observed transport characteristics of graphene decorated by metal NPs are explained in terms of metal induced E_F shift considering the initial adsorption of oxygen molecules on graphene in ambient condition. The results in this chapter are mainly adapted from the publication by Lee et al.[18]

4.2. Experimental Methods

4.2.1. Fabrication of Graphene Field-Effect Transistors

The back-gated graphene FETs were fabricated on a 300-nm-SiO₂/Si substrate (p+ doping) as schematically shown in Figure 4.1a. Single-layer graphene grown on Cu foil by chemical vapor deposition was transferred on the SiO₂ layer, and identified by micro-Raman spectroscopy with 514 nm excitation. As shown in Figure 4.1b, the G band at 1591 cm⁻¹ and 2D band at 2688 cm⁻¹ are observed in the Raman spectrum, and the peak intensity ratio of the 2D band to the G band is greater than 1, which indicates single-layer graphene.[19] The channel length and width were defined as 10 μm by utilizing photolithography and subsequent reactive ion etching in an oxygen ambient environment. Then, the source–drain electrode region was patterned by depositing Ni (1 nm) and Pd/Au (90/100 nm) metal layers onto the photoresist pattern by electron beam evaporation, followed by a lift-off process. The top view optical microscope image of the completed graphene FET is shown in the inset of Figure 4.1b.

4.2.2. Metal Nanoparticles Deposition Employing an Aerosol Technique

To deposit the aerosol-derived metal NPs,[20] a homemade SDG and an ESP were used as shown in Figure 4.2. The SDG consists of a cylindrical chamber (an inner diameter of 20 mm, a height of 37 mm), a pin electrode made of Ag or Pt wire (a diameter of 1.0 mm, Sigma Aldrich), and

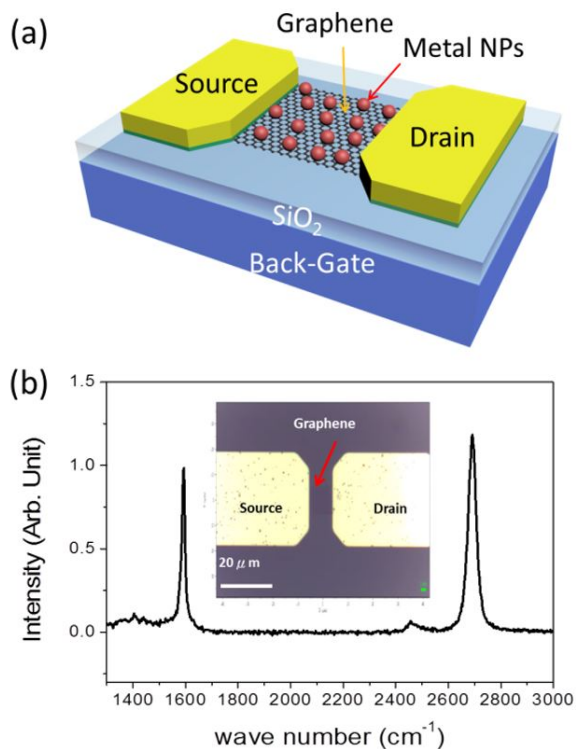


Figure 4.1 (a) Schematic of metal NP-deposited graphene FET fabricated on SiO₂/Si substrate. The electrical contacts are indicated as source, drain, and gate. (b) Raman spectrum (514 nm excitation) of a monolayer graphene film transferred on a SiO₂/Si substrate. The inset shows a top view image of graphene channel and source/drain electrodes from an optical microscope.

a plate electrode made of Ag or Pt foil (5 mm × 5 mm × 0.25 mm, Sigma Aldrich). The axis of the pin electrode was aligned with the center of the plate electrode at which an exit hole of 1 mm in diameter was formed. The tip of the pin electrode was located 1 mm above the plate electrode.

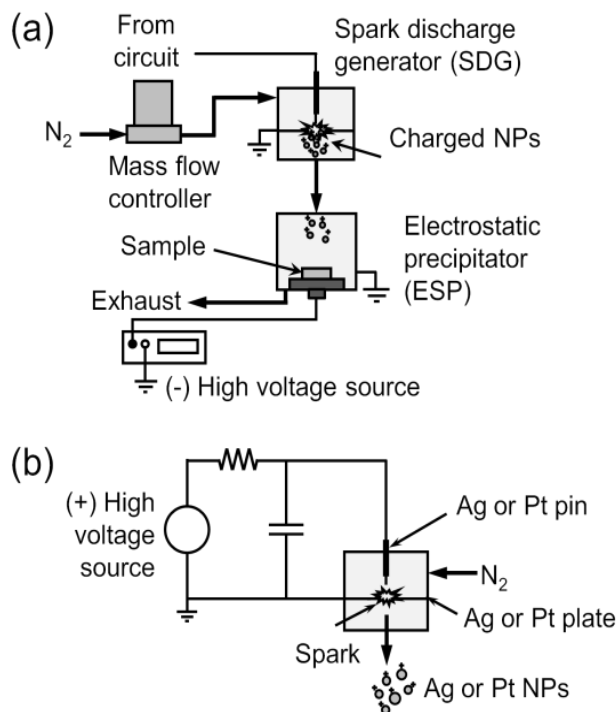


Figure 4.2 (a) Schematic diagram of spark discharge generator consisting of a pin and a plate electrode in a cylindrical chamber for controlling the metal NP generation, equipped with (b) an electrostatic precipitator system composed of a bottom electrode in a grounded cylindrical chamber for regulating the amount of carrier gas.

The Ag or Pt NPs generated by the spark discharge in the SDG were inherently bipolarly charged, and delivered to the ESP through the exit hole by nitrogen carrier gas with a flow rate of 2.0 L min^{-1} or 3.0 L min^{-1} , respectively. The generation of the Ag or Pt NPs in the SDG was controlled by changing the frequency and the energy of sparks generated between the pin and plate electrodes using a RC circuit consisting of a positive high

voltage power supply, a 2 nF capacitor, and a 20-M Ω resistor. The plate electrode was grounded, and the pin electrode was positively biased by 5.0 kV. The ESP was composed of a grounded cylindrical chamber (an inner diameter of 52 mm and a height of 47 mm), and a bottom electrode made of Cu connected to a negative high voltage power supply. Si substrate with graphene FETs was placed on the bottom electrode in the ESP. The positively charged Ag or Pt NPs fed into the ESP were electrostatically guided to and deposited on the substrate surface as the bottom electrode was negatively biased. The magnitude of the negative potential at the bottom electrode was chosen to be -1.0 kV, which resulted in various particle densities on graphene channels across a substrate in a single deposition.

4.3. Characterization

The size distribution of the Ag and Pt NPs generated in the SDG was measured with a scanning mobility particle sizer (SMPS) system consisting of an electrostatic classifier (TSI 3080) with a Kr-85 radiative neutralizer, a differential mobility analyzer (TSI 3085), and a condensation nuclei counter (TSI 3776). The surface coverage derived by the ratio of the occupied area on average for metal NPs to the area of graphene channel was obtained from their SEM images.

4.4. Results and Discussion

4.4.1. Characteristics of Metal Nanoparticle Layers

Figure 4.3 shows the size distribution of the spark-discharge generated Ag and Pt NPs measured using SMPS system. The generated Ag NPs with a total concentration of $9.2 \times 10^7 \text{ cm}^{-3}$ have a geometrical mean diameter (d_g) of 7.5 nm and a standard deviation (σ_g) of 1.5 nm, whereas the Pt NPs with $7.3 \times 10^7 \text{ cm}^{-3}$ have d_g of 6.4 nm and σ_g of 1.4 nm. Upon their generation in the SDG, the metal NPs were fed into the ESP and deposited on the graphene FET.

The surface coverage of the Ag NPs deposited on the graphene channels ranges from 12 (Figure 4.4a), 16, 18 to 21% (Figure 4.4b), while that of the Pt NPs ranges from 24 (Figure 4.4c), 26, 29 to 32% (Figure 4.4d). The insets

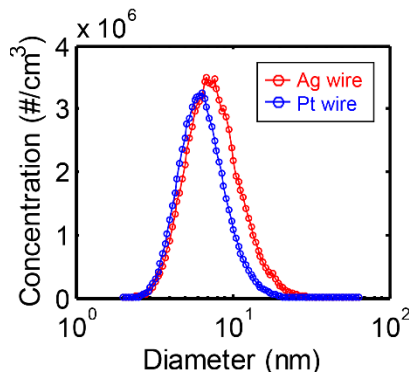


Figure 4.3 Size distribution of aerosol-derived Ag and Pt NPs measured by SMPS system. Geometrical mean diameters of Ag and Pt NPs are 7.5 and 6.4 nm, respectively, and the size of Ag NPs is distributed slightly broader than that of Pt NPs.

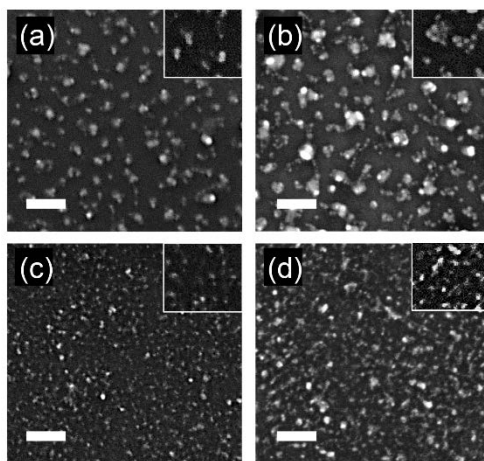


Figure 4.4 FESEM images of the graphene channel deposited with different surface densities of Ag NPs from (a) 12% to (b) 21% and Pt NPs from (c) 24% to (d) 32%, revealing uniformly distributed NPs with consistent size and shape. The scale bars in the images are 100 nm, and the insets represent 2-fold enlarged images.

in Figure 4.4, 2-fold enlarged SEM images, show that the metal NPs are well dispersed with consistent spherical configuration, although the NPs appear to be slightly agglomerated with increasing surface coverage.

4.4.2. Controlled Electrical Transport Properties of Graphene by Doping

Graphene FETs decorated with aerosol-derived Ag or Pt NPs were investigated with transport measurements in ambient condition to observe the shift of Dirac point, the gate voltage of minimum conductivity, depending on electron or hole doping levels.[14,21] Here, a constant drain-source voltage (V_{DS}) of 0.01 V was applied to the graphene FET, and the drain–

source current (I_{DS}) according to the gate-source voltage (V_{GS}) in a range of -60 V to 100 V was measured using an Agilent 4154C semiconductor parameter analyzer at room temperature. Figure 4.5 shows the transport properties of the graphene FETs without and with the decoration of metal NPs. In the absence of metal NPs, the Dirac point of the as-prepared graphene FET was found to be $\sim 22V$, which indicates p-type doping of graphene due to the adsorption of oxygen molecules in the air and the underlying SiO_2 layer.[5,22,23] When the graphene channel was decorated with Ag NPs, electrons transferred from Ag NPs to graphene due to smaller work function (W_F) of Ag (~ 4.64 eV)[24] than that of graphene (~ 4.89 eV)[25], inducing an upward shift in the E_F and n-type doping of graphene. On the other hand, when the graphene channel was covered by Pt NPs, electrons transferred from graphene to Pt NPs due to the larger W_F of Pt (~ 5.9 eV)[24] than that of the graphene, resulting in a downward shift in the E_F and p-type doping of graphene. As the surface coverage of Ag NPs increases from 12, 16, 18 to 21%, the Dirac point in graphene is shifted towards the negative V_{GS} from 18, 9, 3 to -4 V, respectively, as shown in Figure 4.5a. Meanwhile, as the surface coverage of Pt NPs increases from 24, 26, 29 to 32%, the Dirac point in graphene is shifted towards higher positive V_{GS} from 76, 80, 89 to 93V, respectively, as shown in Figure 4.5b.

The carrier density of graphene induced by the deposition of metal NPs is related to the shift of the Dirac point and can be obtained as

$$\Delta n = \frac{C_G}{e} (\Delta V_{Dirac}) \quad (3.3)$$

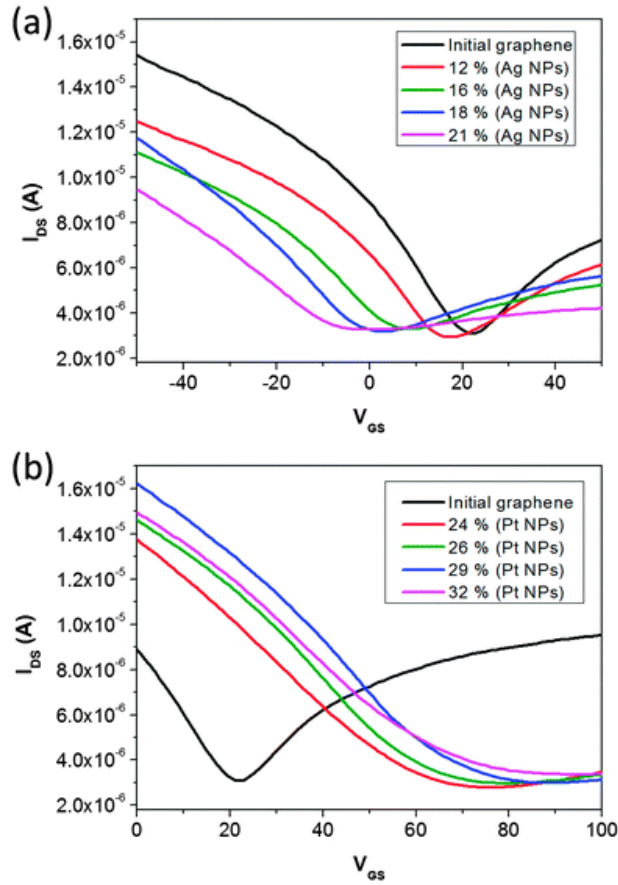


Figure 4.5 Transfer characteristics of graphene FETs with and without (a) Ag NP deposition and (b) Pt NP deposition. Ag NPs on graphene cause a shift in the Dirac point into the negative gate bias direction, while Pt NPs cause a shift into the positive gate bias direction.

where C_G is the gate capacitance per unit area, e is the electric charge, Δn is a net carrier concentration, and ΔV_{Dirac} is a shift of the Dirac point in metal NP-decorated graphene relative to that in the initially p-type doped graphene

($V_{Dirac}^0 = \sim 22$ V). The initial hole doping of graphene due to adsorbed oxygen molecules is estimated to $1.6 \times 10^{12} \text{ cm}^{-2}$. Here it is noted that plus (minus) values corresponds to a concentration of hole (electron) carriers. When the surface coverage of Ag NPs increases from 12, 16, 18 to 21%, ΔV_{Dirac} of -4, -13, -19, to -26 V in the Ag NP-deposited graphenes corresponds to a net electron concentration of -2.9×10^{11} , -9.5×10^{11} , -1.4×10^{12} to $-1.9 \times 10^{12} \text{ cm}^{-2}$, respectively. Meanwhile, when the surface coverage of Pt NPs increases from 24, 26, 29 to 32%, ΔV_{Dirac} of 54, 58, 67, to 71 V in the Pt NP-deposited graphenes leads to a net hole concentration of 3.9×10^{12} , 4.2×10^{12} , 4.9×10^{12} to $5.2 \times 10^{12} \text{ cm}^{-2}$, respectively. The relation of the doping concentration and the surface coverage or interparticle spacing of metal NPs are presented in Figure 4.6. It should be noted here that the doping level of graphene was gradually modulated in correlation with the surface coverage, or interparticle spacing of metal NPs. This is attributed to the consistent spherical configuration of the aerosol-derived metal NPs regardless of the deposition amount, which was hardly achieved by using solution or thermal evaporation processes demonstrated in previous literatures due to random aggregation or island formation issues.

The electrical transport characteristics of the metal NP-decorated graphene are illustrated by the schematic energy band diagrams as shown in Figure 4.7a and Figure 4.7b. The E_F of the initial graphene before the deposition of metal NPs is situated on a valance band (black Dirac cone) due to the adsorption of oxygen molecules on the graphene channel. As the surface coverage of Ag NPs deposited on graphene increases from 12, 16, 18 to 21%, E_F of the graphene is shifted upward to the Dirac point (red,

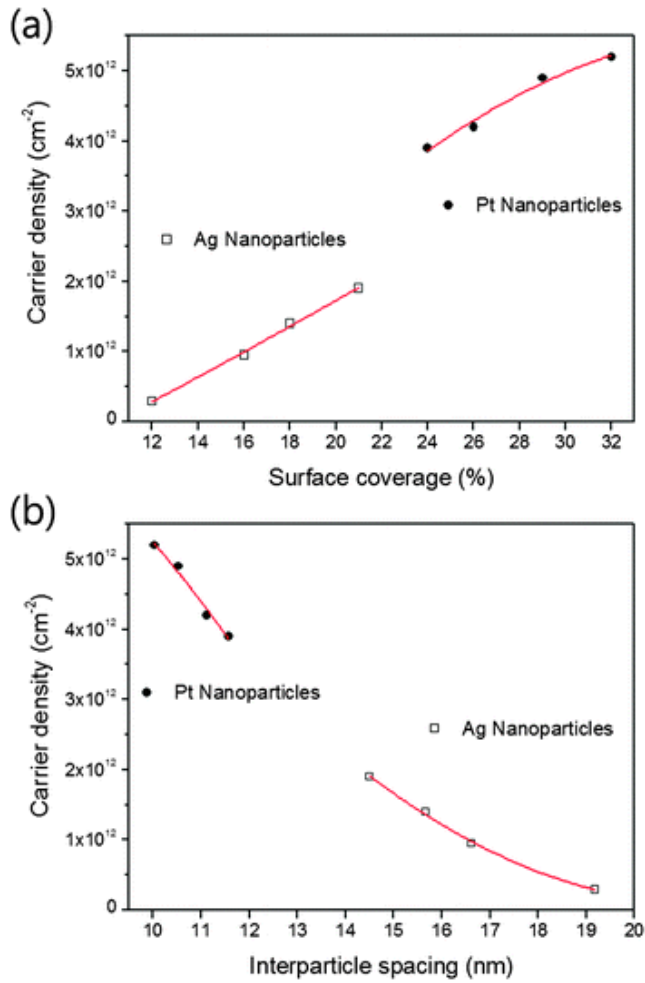


Figure 4.6 Carrier density per unit area of graphene as a function of (a) the surface coverage or (b) the inter-particle spacing for Ag and Pt NPs: the open squares and the closed black circles correspond to Ag and Pt NPs deposited on graphene, respectively, while the solid lines are the fit curves.

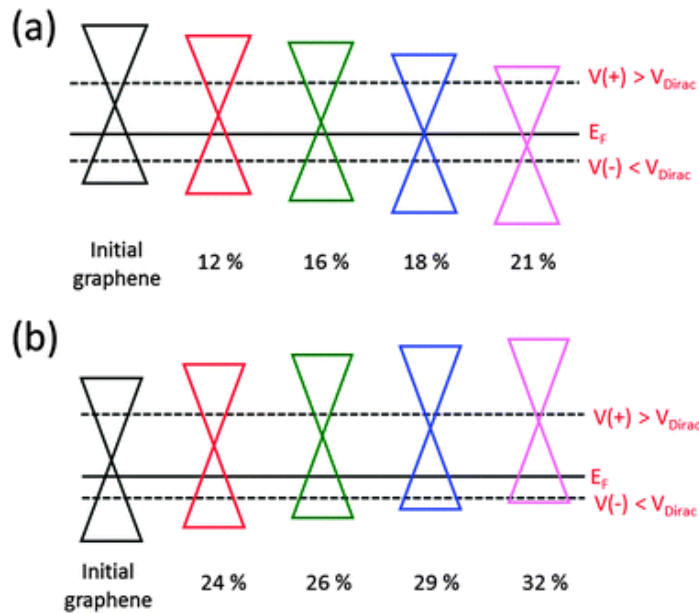


Figure 4.7 Schematic energy band diagrams of graphenes without and with (a) Ag NPs doping with different density of 12, 16, 18, and 21%, and (b) Pt NPs doping with 24, 26, 29 and 32%.

green, blue Dirac cones) and then further moved to conduction band (pink Dirac cone) inducing n-type doping of graphene, as depicted in Figure 4.7a. At V_{GS} less than each Dirac point, e.g. $V_{GS} = -20$ V, the graphene sheets without and with Ag NPs were electrostatically doped to strong p- and p-type, respectively, with the E_F situated in the valence band, inducing lower hole current in the Ag-decorated graphene channel than that in initial graphene as shown in Figure 4.5a. Meanwhile, as the V_{GS} was increased to the positive direction, the E_F s were shifted upward to the conduction band passing through the Dirac point, and the graphene channels without and with Ag NPs were changed to be n- and strong n-type, respectively, with the E_F

located in the conduction band. Now electron transfer was dominated, however, the electron current in Ag-deposited graphene became higher or lower than that in graphene without NPs as shown in Figure 4.5a, which was attributed to the interrelation between the increase of carrier concentration by metal doping and the decrease in carrier mobility by charged impurity scattering. The absorbed oxygen molecules on graphene acted as electron acceptors to become negatively charged impurities,[26] and thus reduced electron mobility of graphene through typical charged impurity scattering.[27]

On the other hand, as the surface coverage of Pt NPs deposited on the graphene increased from 24, 26, 29 to 32%, the E_F of the graphene was shifted downward to valence band region (red, green, blue, and pink Dirac cones), resulting in p-type doping of graphene, as shown in Figure 4.7b. At V_{GS} less than each Dirac point, e.g. at $V_{GS} = 10$ V, the graphene without and with Pt NPs were electrostatically doped to p- and strong p-type, respectively, resulting in higher hole current in Pt-doped graphene than that in the initial graphene as shown in Figure 4.5b. As the V_{GS} was increased to the positive direction, the E_F in the graphene channels was shifted upward to the conduction band passing through each Dirac point. When the E_F met the Dirac point, the reduced density of states in the graphene channel led to minimum conductance. At a positive V_{GS} greater than each V_{Dirac} , the graphenes without and with the Pt NP deposition were electrostatically doped to strong n- and n-type, respectively. Here, the weak n-type conduction in the Pt NP-decorated graphene compared to the strong n-type conduction in the initial graphene led to the suppression of electron currents

in this positive gate voltage range. Additionally, the charge impurity scattering by the oxygen molecules adsorbed on graphene may lower electron mobility of graphene. Thus, as the surface coverage of the Pt NPs increased, a strong p-type doping in graphene was enhanced, and consequently the bipolar characteristics of the graphene became unipolar ones as shown in Figure 4.5b. It is noted again that the consistent surface morphology of the aerosol-derived metal NPs allowed us to attribute the change in doping level of graphene to the electron transfer between the metal NPs and graphene due to the work function difference. In addition, the conductance of graphene at the Dirac point has barely changed by deposition of aerosol metal NPs, indicating an absence of transition from in-plan sp^2 hybridization to off-plane sp^3 hybridization of the graphene surface by metal NP-induced local defects.[28,29] In the previous reports, the bond dissociation energy of C–N and C–C (sp^3 - sp^2) covalent bonds is typically order of 3 ~ 4 eV,[30] and van der Waals bond energy of carbon layers is usually of a few tenths of eV.[31] The kinetic energy of thermally evaporated NPs determined by the process temperature is an order of a few tenth eV, so that they can cause damage on the van der Waals bond underlying graphene layers. Meanwhile, the kinetic energy of aerosol-derived metal NPs determined by balancing the electrostatic and the fluid frictional forces, is estimated to a few meV, suggesting no significant damage on the underlying graphene layers.[32] In this respect, the aerosol-derived metal NPs with consistent size and configuration can provide reliable control of carrier concentration in graphene to modulate its electrical transport properties

without detrimental impacts on a graphene surface, compare to the previously reported methods.

4.5. Conclusion

Aerosol-derived Ag and Pt NPs have been used for reliable control of doping type and doping level of graphene. Ag NPs with a surface coverage of 21% provide an electron concentration of $1.9 \times 10^{12} \text{ cm}^{-2}$, whereas Pt NPs with a surface coverage of 32% induce a hole concentration of $5.1 \times 10^{12} \text{ cm}^{-2}$ in a initially p-doped graphene ($1.6 \times 10^{12} \text{ cm}^{-2}$) by the adsorption of ambient oxygen molecules. The change in doping level and doping type of graphene is attributed to the electron transfer between the metal NPs and graphene owing to the work function difference. Due to the consistent size and shape of the aerosol-derived metal NPs, doping level has been changed monotonously with increasing the surface coverage of the NPs, which has been hardly achieved in the previous reports using thermal evaporation and spin-coating methods due to morphology change and random aggregation of metal NPs. In addition, the aerosol-derived metal NPs with low kinetic energy during deposition may provide no detrimental impacts on a graphene surface unlike to the thermal evaporation method. Therefore, suggested metal-graphene contact approach can be regarded as an effective way to precisely tailor the electronic property and chemical reactivity of graphene for versatile device applications.

4.6. References

- [1] A.K. Geim, "Graphene: status and prospects", *Science*, **324**, 1530-1534 (2009)
- [2] Y. Zhu, S. Murali, W. Cai, X. Li, J.W. Suk, J.R. Potts, R.S. Ruoff, "Graphene and graphene oxide: synthesis, properties, and applications", *Adv. Mater.*, **22**, 3906-3924 (2010)
- [3] W. Bao, F. Miao, Z. Chen, H. Zhang, W. Jang, C. Dames, C.N. Lau, "Controlled ripple texturing of suspended graphene and ultrathin graphite membranes", *Nat. Nanotechnol.*, **4**, 562-566 (2009)
- [4] H. Li, Q. Zhang, C. Liu, S. Xu, P. Gao, "Ambipolar to unipolar conversion in graphene field-effect transistors", *ACS Nano*, **5**, 3198-3203 (2011)
- [5] P. Joshi, H.E. Romero, A.T. Neal, V.K. Toutam, S.A. Tadigadapa, "Intrinsic doping and gate hysteresis in graphene field effect devices fabricated on SiO₂ substrates", *J. Phys.: Condens. Matter*, **22**, 334214 (2010)
- [6] Z. Yan, J. Yao, Z. Sun, Y. Zhu, J.M. Tour, "Controlled ambipolar-to-unipolar conversion in graphene field-effect transistors through surface coating with poly(ethylene imine)/poly(ethylene glycol) films", *Small*, **8**, 59-62 (2012)
- [7] J.R. Williams, L. DiCarlo, C.M. Marcus, "Quantum hall effect in a gate-controlled p-n junction of graphene", *Science*, **317**, 638-641 (2007)
- [8] T. Lohmann, K. von Klitzing, J.H. Smet, "Four-terminal magneto-transport in graphene p-n junctions created by spatially selective doping",

Nano Lett., **9**, 1973-1979 (2009)

[9] X. Miao, S. Tongay, M.K. Petterson, K. Berke, A.G. Rinzler, B.R. Appleton, A.F. Hebard, "High efficiency graphene solar cells by chemical doping

", *Nano Lett.*, **12**, 2745-2750 (2012)

[10] Z. Sun, Z. Yan, J. Yao, E. Beitler, Y. Zhu, J.M. Tour, "Growth of graphene from solid carbon sources", *Nature*, **468**, 549-552 (2010)

[11] Y.-C. Lin, C.-Y. Lin, P.-W. Chiu, "Controllable graphene N-doping with ammonia plasma", *Appl. Phys. Lett.*, **96**, 133110 (2010)

[12] G. Giovannetti, P.A. Khomyakov, G. Brocks, V.M. Karpan, J. van den Brink, P.J. Kelly, "Doping graphene with metal contacts", *Phys. Rev. Lett.*, **101**, (2008)

[13] J. Lee, K.S. Novoselov, H.S. Shin, "Interaction between metal and graphene: dependence on the layer number of graphene", *ACS Nano*, **5**, 608-612 (2011)

[14] Y. Ren, S. Chen, W. Cai, Y. Zhu, C. Zhu, R.S. Ruoff, "Controlling the electrical transport properties of graphene by in situ metal deposition", *Appl. Phys. Lett.*, **97**, 053107 (2010)

[15] X. Shi, G. Dong, M. Fang, F. Wang, H. Lin, W.-C. Yen, K.S. Chan, Y.-L. Chueh, J.C. Ho, "Selective n-type doping in graphene via the aluminium nanoparticle decoration approach", *J. Mater. Chem. A*, **2**, 5417 (2014)

[16] Y. Wu, W. Jiang, Y. Ren, W. Cai, W.H. Lee, H. Li, R.D. Piner, C.W. Pope, Y. Hao, H. Ji, J. Kang, R.S. Ruoff, "Tuning the doping type and level of graphene with different gold configurations", *Small*, **8**, 3129-3136 (2012)

- [17] R. Muszynski, B. Seger, P.V. Kamat, "Decorating graphene sheets with gold nanoparticles", *The Journal of Physical Chemistry C*, **112**, 5263-5266 (2008)
- [18] J.-K. Lee, H. Sung, M.S. Jang, H. Yoon, M. Choi, "Reliable doping and carrier concentration control in graphene by aerosol-derived metal nanoparticles", *J. Mater. Chem. A*, **3**, 8294-8299 (2015)
- [19] A.C. Ferrari, "Raman spectroscopy of graphene and graphite: Disorder, electron-phonon coupling, doping and nonadiabatic effects", *Solid State Commun.*, **143**, 47-57 (2007)
- [20] K. Han, W. Kim, J. Yu, J. Lee, H. Lee, C. Gyu Woo, M. Choi, "A study of pin-to-plate type spark discharge generator for producing unagglomerated nanoaerosols", *J. Aerosol Sci.*, **52**, 80-88 (2012)
- [21] A. Das, S. Pisana, B. Chakraborty, S. Piscanec, S.K. Saha, U.V. Waghmare, K.S. Novoselov, H.R. Krishnamurthy, A.K. Geim, A.C. Ferrari, A.K. Sood, "Monitoring dopants by Raman scattering in an electrochemically top-gated graphene transistor", *Nat. Nanotechnol.*, **3**, 210-215 (2008)
- [22] S. Ryu, L. Liu, S. Berciaud, Y.-J. Yu, H. Liu, P. Kim, G.W. Flynn, L.E. Brus, "Atmospheric oxygen binding and hole doping in deformed graphene on a sio₂ substrate", *Nano Lett.*, **10**, 4944-4951 (2010)
- [23] Y.-J. Kang, J. Kang, K.J. Chang, "Electronic structure of graphene and doping effect on SiO₂", *Phys. Rev. B*, **78**, 115404 (2008)
- [24] D.R. Lide, "CRC handbook of chemistry and physics"(2004), *CRC press*,
- [25] S.M. Song, J.K. Park, O.J. Sul, B.J. Cho, "Determination of work

function of graphene under a metal electrode and its role in contact resistance", *Nano Lett.*, **12**, 3887-3892 (2012)

[26] B. Chen, H. Huang, X. Ma, L. Huang, Z. Zhang, L.-M. Peng, "How good can CVD-grown monolayer graphene be?", *Nanoscale*, **6**, 15255-15261 (2014)

[27] J.H. Chen, C. Jang, S. Adam, M.S. Fuhrer, E.D. Williams, M. Ishigami, "Charged-impurity scattering in graphene", *Nat. Phys.*, **4**, 377-381 (2008)

[28] S. Al-Harhi, M. Elzain, M. Al-Barwani, A. Kora'a, T. Hysen, M.T. Myint, M. Anantharaman, "Unusual surface and edge morphologies, sp² to sp³ hybridized transformation and electronic damage after Ar⁺ ion irradiation of few-layer graphene surfaces", *Nanoscale Res Lett*, **7**, 466 (2012)

[29] M. Lafkioti, B. Krauss, T. Lohmann, U. Zschieschang, H. Klauk, K.v. Klitzing, J.H. Smet, "Graphene on a hydrophobic substrate: doping reduction and hysteresis suppression under ambient conditions", *Nano Lett.*, **10**, 1149-1153 (2010)

[30] D.Y. Kondakov, "Role of chemical reactions of arylamine hole transport materials in operational degradation of organic light-emitting diodes", *J. Appl. Phys.*, **104**, 084520 (2008)

[31] V.V. Gobre, A. Tkatchenko, "Scaling laws for van der Waals interactions in nanostructured materials", *Nat. Commun.*, **4**, (2013)

[32] H. Sung, J. Lee, K. Han, J.-K. Lee, J. Sung, D. Kim, M. Choi, C. Kim, "Controlled positioning of metal nanoparticles in an organic light-emitting device for enhanced quantum efficiency", *Org. Electron.*, **15**, 491-499 (2014)

Chapter 5.

High-Efficiency Transparent Conductive Oxide-Free Solar Cells with Metal Oxide- Modified Graphene Anode

5.1. Introduction

Organic/inorganic hybrid perovskites have been considered as promising materials for use in photoactive layers of solar cells due to their unique properties such as high absorption coefficient, balanced electron/hole mobility, possible low-temperature processing, smaller exciton binding energy, and longer exciton diffusion length than those of organic semiconducting materials.[1-9] Perovskite solar cells with high performances have usually adopted n-i-p architecture consisting of scaffold metal oxide, such as TiO₂ or Al₂O₃, / perovskite material / hole transport material.[9-11] For the preparation of the metal oxide films, however, high-temperature process over 450°C is needed, which limits substrate choice and is not compatible with the low-cost manufacturing.

As an alternative to the metal oxide layers, organic materials have been employed in perovskite solar cells, generally with p-i-n architecture. Here solution-processable (PEDOT:PSS and [6, 6]-phenyl C61-butyric acid methyl ester (PCBM) have been typically used as a HTL and an electron transport layer (ETL), respectively.[5,12-14] Very recently, 18.1% PCE has been achieved with p-i-n devices consisting of ITO / PEDOT:PSS / CH₃NH₃PbI₃ (MAPbI₃) / PCBM / Au,[15] which is still low compared to the n-i-p devices using scaffold metal oxide for ETLs. Nevertheless, p-i-n perovskite solar cells have attracted much research interest due to their benefits of low hysteresis behavior, low processing temperature and facile manufacturing process.[14,15]

Taking advantage of the low-temperature processes, perovskite solar cells with p-i-n architecture have been employed on flexible substrates [5,13] where ITO on plastic substrates has been typically used as a transparent anode. However, ITO was found to generate cracks and induced fracture under bending condition due to its mechanical brittleness.[16] Meanwhile, a variety of bendable conducting electrodes, such as graphene,[17-20] carbon nanotubes,[21-23] metal grids[24-26], and conductive polymers.[27,28], have been demonstrated in organic photovoltaics (OPVs) to replace brittle TCOs for flexible solar cell applications. Among them, graphene, a single-layer 2D carbon material, would be the most promising candidate because it is optically highly transparent (about 97% in visible range), mechanically robust, flexible, and stretchable. TCO-free OPV devices with a graphene anode have already been successfully demonstrated showing a PCE of 8.48%, the highest efficiency for the TCO-free tandem polymer solar cells,[20] although still lower than 11.0% PCE of the TCO-free perovskite solar cells which used PEDOT:PSS as an anode electrode.[29] Graphene electrodes also have been recently utilized in perovskite devices,[30,31] however, in these studies, graphene was not used for replacing the conventional TCO electrode but for a top electrode.

In this chapter, a high-efficiency TCO-free inverted perovskite solar cell is demonstrated using graphene as a transparent anode. A few nanometer thick MoO_3 layers are introduced between graphene and a HTL, PEDOT:PSS, which not only provides hydrophilicity to the graphene surface but also elevates its lower work function (4.23 eV) to a higher level (4.71 eV) by hole doping of graphene. The wettability of PEDOT:PSS and the

device characteristics are affected by the thickness of the MoO₃ layer, and, as a result, best PCE of 17.1% is achieved from the graphene-based devices with a 2-nm-thick MoO₃ interfacial layer. For comparison, ITO-based perovskite solar cells employing MoO₃ interfacial layers have been fabricated. Their PCEs also vary with the thickness of the MoO₃ layer, presenting the best PCE of 18.8% with a 1 nm-thick MoO₃ layer. The effects of the MoO₃ thickness on PCEs of the graphene- and the ITO-based devices are thoroughly examined by analyzing hydrophilicity of electrode surfaces, electrode work functions, surface morphologies of constitutive films, and device properties. The results in this chapter are mainly adapted from the publication by Sung et al.[32]

5.2. Experimental Methods

5.2.1. Fabrication of Graphene-Based Perovskite Solar Cells

The graphene devices were fabricated on a commercially available single-layer graphene-coated glass substrates (Graphene Square Inc., $>1\text{k } \Omega \text{ cm}^{-2}$, $15 \times 15 \text{ mm}^2$) which were provided by transferring the chemical vapor deposition (CVD)-grown graphene on a copper foil to the cleaned glass substrates (AMG, $25 \times 25 \text{ mm}^2$).[33] The Raman spectrum of the as-prepared graphene is shown in Figure 5.1. The I_{2D}/I_G intensity ratio of the spectrum is ~ 3.0 and the FWHM of its symmetric 2D band is $\sim 32 \text{ cm}^{-1}$, indicating that the graphene is single layer. The D band ($\sim 1350 \text{ cm}^{-1}$) corresponding to the

defect level in graphene is seen to be small, indicating good quality of the film.

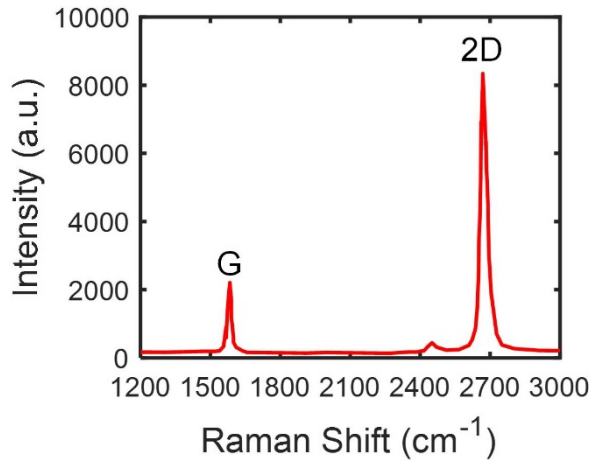


Figure 5.1 Raman spectrum of the as-prepared graphene transferred on a SiO₂/Si substrate.

The ITO devices were fabricated on a commercially obtained ITO-coated glass substrates (AMG, 9.5 Ω cm⁻², 25 × 25 mm²). The graphene-coated glass substrates were used as received, and the ITO-coated glass substrates were used after sequential cleaning in acetone, isopropanol and deionized water using an ultrasonic bath (15 min each), followed by drying with nitrogen gas and storing in an oven at 120 °C. Right before use, the ITO-coated glass substrates were subjected to UVO treatment for 30 min.

The ultra-thin MoO₃ layers with varying thickness from 1 nm to 4 nm were fabricated on the graphene- or ITO-coated glass substrates at deposition rate of 0.1 Å s⁻¹ using a vacuum thermal evaporator, followed by an

annealing at 150 °C for 10 min. The deposition rate and the thickness were monitored by a quartz crystal sensor during the deposition. The thickness values measured by the quartz crystal sensor are very small, and thus they represent the total mass of deposited MoO₃, rather than the actual thickness of the MoO₃ “layer”. To prepare a highly uniform PEDOT:PSS (Clevios P VP Al 4083) HTL, the substrates were prewetted with deionized water, and the PEDOT:PSS solution of 50 µl was dropped onto the rotating substrates right after starting the spin-coating process at 5000 rpm for 30 sec. The MAPbI₃ perovskite layers were fabricated via Lewis base adduct method described by Ahn et al.[34] A 1:1:1 molar ratio mixture of PbI₂ (Alfa Aesar), MAI (MAI was synthesized by the method elsewhere[2,3]) and dimethyl sulfoxide (DMSO, Sigma Aldrich) was dissolved in DMF at 50 wt% without heating. The fully dissolved solution was spin-coated onto the PEDOT:PSS layer at 3500 rpm for 20 sec, with a dropping of 0.3 ml diethyl ether 8 sec after starting the spin-coating process. The transparent green film, so called CH₃NH₃I•PbI₂•DMSO adduct film, changed to a dark brownish perovskite film by heating at 65 °C for 1 min and 100 °C for 4 min. After that, the C₆₀ (20nm), bathocuproine (BCP) (10nm), LiF (0.5 nm), and Al (150 nm) were thermally deposited on the substrates inside the vacuum thermal evaporator under <10⁻⁶ Torr. All the spin-coating processes were carried out in ambient condition.

5.2.2. Characterization

SEM images were obtained using field-emission scanning electron microscopy (AURIGA, Zeiss) and the cross-sectional images were obtained

using the same equipment from the samples milled by focused ion beam. Solar simulated AM 1.5G sunlight was generated with Oriel Sol3A solar simulator calibrated to give 100 mW cm^{-2} using a standard Si photovoltaic cell (RC-1000-TC-KG5-N, VLSI Standards). $J-V$ curves were recorded with a Keithley 2400 source meter. The forward and reverse scan rate was set to 200 ms per 20 mV. The active area of the devices is 1.77 mm^2 . EQE spectra were measured with a Newport IQE200 system equipped with a 300 mW Xenon light source and a lock-in amplifier. Sheet resistance was measured using a four-point probe (CMT-SERIES, Advanced Instrument Technology). Transmittance was measured by UV-vis spectroscopy (Cary 5000, Agilent). ultraviolet photoelectron spectroscopy (UPS) measurement was carried out by using a He discharge lamp (He I 21.2 eV, AXIS-NOVA, Kratos). AFM images were obtained using a XE-100 (Park Systems) scanning probe microscope in noncontact mode.

5.3. Results and Discussion

5.3.1. Device Structure

The structure of the devices consisting of graphene / MoO₃ / PEDOT:PSS / MAPbI₃ / fullerene (C₆₀) / BCP / LiF / aluminum (Al) is schematically illustrated in Figure 5.2. We adopted an inverted MAPbI₃ perovskite solar cell structure using PEDOT:PSS and C₆₀ / BCP as the HTL and the ETL, respectively, because the structure is low-temperature processable and thus suitable for future application on flexible plastic substrates. A single layer graphene, grown by CVD, was utilized as a transparent anode rather than a cathode because increasing its work function (~4.3 eV) by p-doping induced not only an enhanced conductivity but also a desirable energy level alignment with the HOMO level of HTLs (~5.2 eV for PEDOT:PSS, for

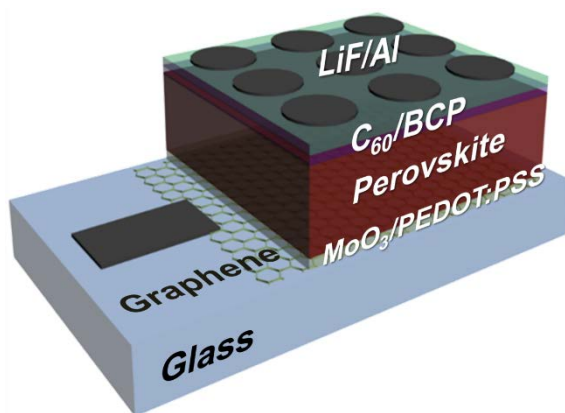


Figure 5.2 Schematic structure of the inverted MAPbI₃ perovskite solar cells utilizing graphene as a transparent anode.

example). Between the graphene and the PEDOT:PSS film, we added a MoO₃ layer by vacuum thermal evaporation, followed by thermal annealing at 150°C on a hot plate to prevent washout during the subsequent spin-coating processes. By varying the thickness of the MoO₃ layer from 0 to 4nm, the interfacial properties of the graphene electrode such as wettability and doping level can be engineered.[18,35]

5.3.2. Wetting Issue of PEDOT:PSS on Graphene Surfaces

The wettability of PEDOT:PSS on graphene and ITO surfaces was crucial for fabricating high performance devices, and it was investigated without and with a MoO₃ layer using a contact angle measurement. Figure 5.3 shows the optical microscopy images of PEDOT:PSS droplets dripped onto the surfaces of graphene and ITO, and the insets show the optical images of PEDOT:PSS/MAPbI₃ deposited on the glass/graphene substrates. Without a MoO₃ layer, as shown in Figure 5.3a, the contact angle of the PEDOT:PSS was measured as $90.4\pm 0.3^\circ$ on graphene surface, on which, consequently, continuous PEDOT:PSS/MAPbI₃ layers were hardly formed by a spin-coating process (inset, Figure 5.3a). With a 1 nm-thick MoO₃ layer on graphene, however, the contact angle was reduced to $46.6\pm 1.3^\circ$, and further to $30.0\pm 1.6^\circ$ with a 2 nm-thick MoO₃ layer, as shown in Figure 5.3b and Figure 5.3c, respectively. The improved wettability by the MoO₃ layers also can be confirmed from the insets of Figure 5.3b and Figure 5.3c. The dark brownish MAPbI₃ films were observed to be well formed in a square shape at the center of the glass substrates where the MoO₃ layers were deposited

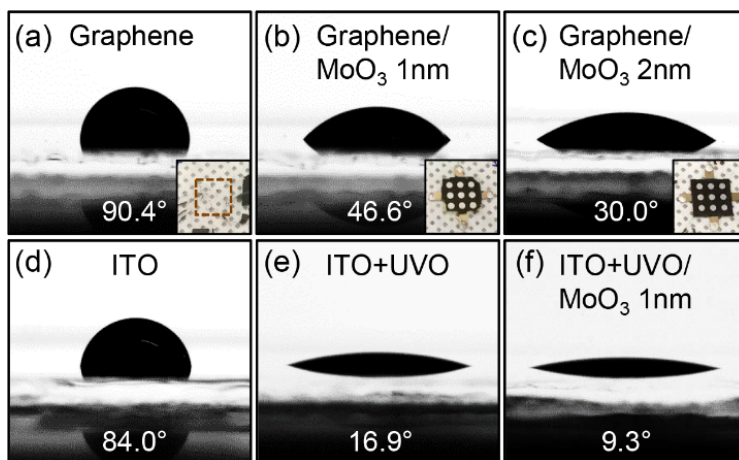


Figure 5.3 Droplets of PEDOT:PSS on (a) as-prepared graphene, (b) graphene covered with 1 nm MoO₃, (c) graphene covered with 2 nm MoO₃, (d) as-prepared ITO, (e) UVO-treated ITO, and (f) ITO covered with 1 nm MoO₃ after UVO treatment. Enhanced wetting of PEDOT:PSS on both graphene and ITO surfaces was observed after thermal deposition of the MoO₃ layers. The insets in (a) – (c) show the optical images of PEDOT:PSS/MAPbI₃ films fabricated on the corresponding glass/graphene surfaces. The MoO₃ layers were pre-formed in a square shape at the center of the substrates before spin-coating those PEDOT:PSS/MAPbI₃ films.

by thermal evaporation in advance. Particularly, a very clear square-shaped MAPbI₃ film was formed on the 2 nm-thick MoO₃ layer, indicating better wetting of PEDOT:PSS on the thicker MoO₃ layer (see inset of Figure 5.3c). The SEM images in Figure 5.4 clearly show that the hydrophobic graphene surface, which was not covered sufficiently by the 1 nm-thick MoO₃ layer,

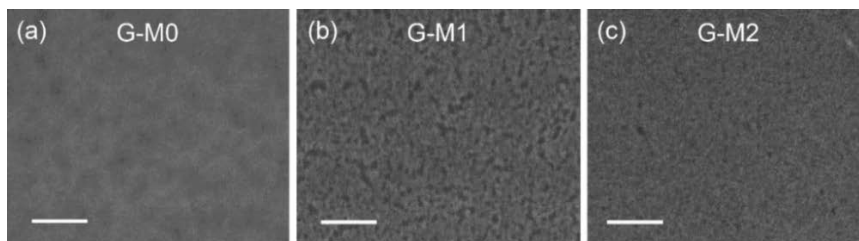


Figure 5.4 Plan-view SEM images of (a) as-prepared graphene, (b) graphene/1 nm MoO₃ and (c) graphene/2 nm MoO₃ (scale bar, 100 nm). The MoO₃ layers were deposited by thermal evaporation with deposition rate of 0.1 Å s⁻¹, followed by 150 °C annealing for 10 min.

became almost completely covered by the 2 nm-thick MoO₃ layer. For comparison, the contact angles of PEDOT:PSS on ITO surfaces were also measured before and after the combinational treatment of UVO and MoO₃ deposition, as shown in Figure 5.3d – Figure 5.3f. Similar to graphene, the as-prepared ITO surface was not wettable for PEDOT:PSS to form a continuous film by spin-coating. Applying UVO treatment to the ITO surface, the contact angle was considerably decreased from 84.0±1.3° (Figure 5.3d) to 16.9±1.8° (Figure 5.3e), and slightly further to 9.3±0.6° (Figure 5.3f) with the 1 nm-thick MoO₃ layer, which implies improved hydrophilicity of the ITO surfaces. Figure 5.5 show the cross-sectional SEM images of the fabricated devices employing the graphene electrode with 2 nm-thick MoO₃ (Figure 5.5a) and the ITO electrode with 1 nm-thick MoO₃ (Figure 5.5b). The images on the left hand side were measured in the secondary electron (SE) mode, and on the right hand side back-scattered electron (BSE) mode. The hydrophilicity imposed by the MoO₃ interfacial layer allows

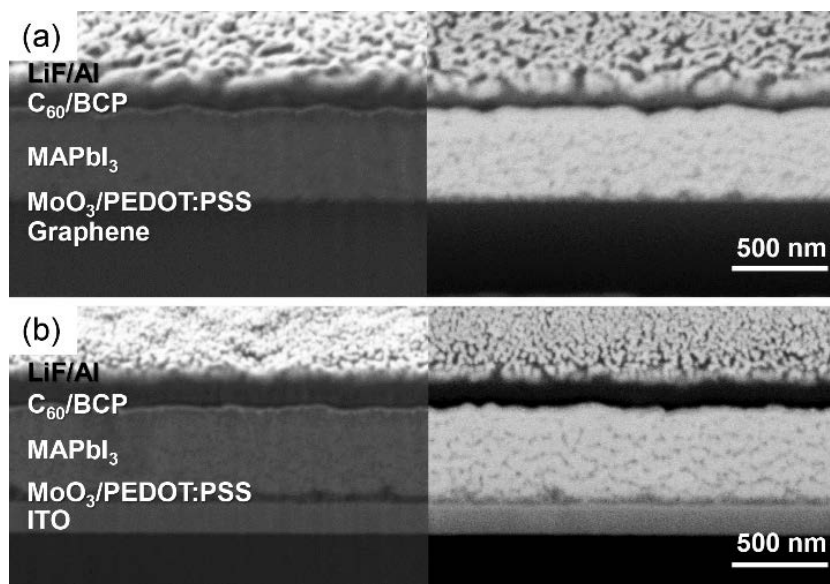


Figure 5.5 Cross-sectional SEM images of the devices employing (a) graphene/2 nm MoO₃ electrode and (b) ITO/1 nm MoO₃ electrode measured in SE mode (left) and BSE mode (right).

for a smooth and continuous formation of the PEDOT:PSS via spin-coating on both graphene and ITO with similar thickness (~50 nm) and morphology. In addition, the surface of the perovskite films were observed to be quite smooth with similar thickness (~510 nm) in both cases as shown in Figure 5.5. These smooth and dense perovskite films were fabricated via Lewis base adduct of PbI₂ that we recently developed to create highly reproducible n-i-p perovskite solar cells with the best PCE of 19.7%. [34]; CH₃NH₃I (MAI)•PbI₂•dimethyl sulfoxide (DMSO) adduct films were first formed by spin-coating with dripping diethyl ether to wash out the surplus

dimethylformamide (DMF) solvent, and then were transformed to the perovskite films through annealing.

5.3.3. Device Characteristics

In order to investigate the influence of the MoO₃ thickness on the device performance, MoO₃ layers with four different thicknesses (0, 1, 2, and 4 nm) were employed to both graphene and ITO electrodes. The resultant photovoltaic properties of the devices are summarized in Table 5.1, and the relationship between the average PCE and the thickness of the MoO₃ layer is depicted in Figure 5.6a and Figure 5.6b for graphene and ITO electrodes, respectively. For convenience, the electrodes modified by the MoO₃ layers

Table 5.1 Photovoltaic parameters of the graphene- and ITO-based devices with MoO₃ layers of varying thickness

Sample ID	Electrode	MoO ₃ thickness [nm]	V_{oc} [V]	J_{sc} [mA cm ⁻²]	FF	PCE [%]	Best PCE [%]
G-M1	Graphene	1	0.72 ± 0.36	17.6 ± 6.3	0.45 ± 0.09	6.7 ± 4.2	12.1
G-M2		2	1.03 ± 0.02	21.9 ± 0.4	0.72 ± 0.02	16.1 ± 0.6	17.1
G-M4		4	1.00 ± 0.01	22.9 ± 0.4	0.70 ± 0.02	15.9 ± 0.5	16.2
ITO-M0	ITO	0	0.96 ± 0.01	21.4 ± 0.5	0.83 ± 0.02	17.0 ± 0.4	17.6
ITO-M1		1	0.97 ± 0.01	22.6 ± 0.4	0.83 ± 0.01	18.2 ± 0.5	18.8
ITO-M2		2	0.95 ± 0.01	22.2 ± 0.4	0.76 ± 0.01	16.1 ± 0.4	16.9
ITO-M4		4	0.94 ± 0.01	21.0 ± 0.4	0.74 ± 0.01	14.7 ± 0.6	15.7

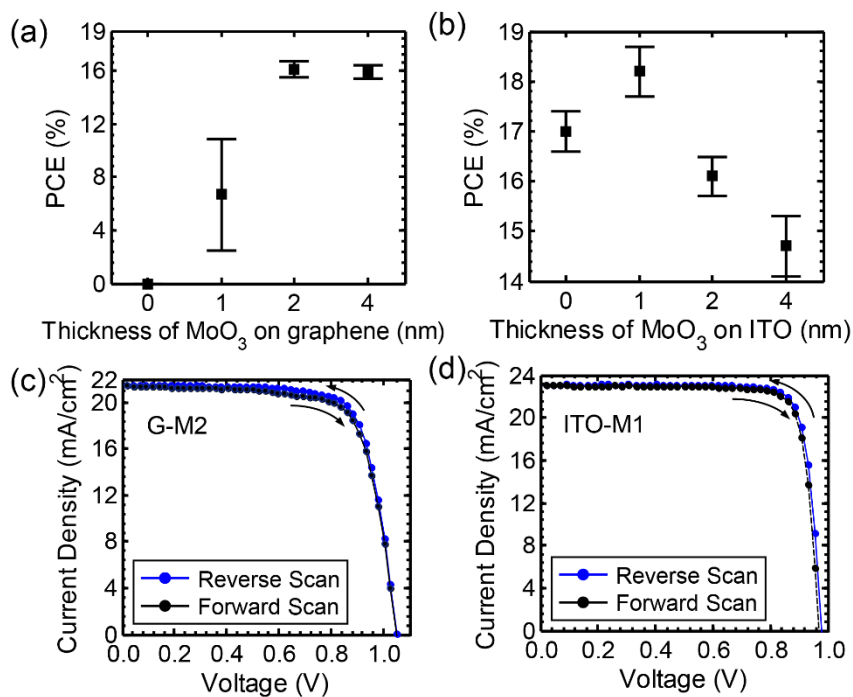


Figure 5.6 (a), (b) Relationship between average PCE and MoO₃ thickness for (a) graphene electrodes and (b) ITO electrodes. (c), (d) *J-V* curves for best-performing (c) G-M2 and (d) ITO-M1 devices under AM 1.5G illumination at 100 mW cm⁻² measured via reverse (blue) and forward (black) bias sweep.

were named as G-M0, G-M1, G-M2, G-M4, ITO-M0, ITO-M1, ITO-M2, and ITO-M4, where the number refers to the thickness of the MoO₃ layer in nanometer, G and ITO refer to the graphene and the ITO electrodes, respectively. In the case of the graphene-based devices, as shown in

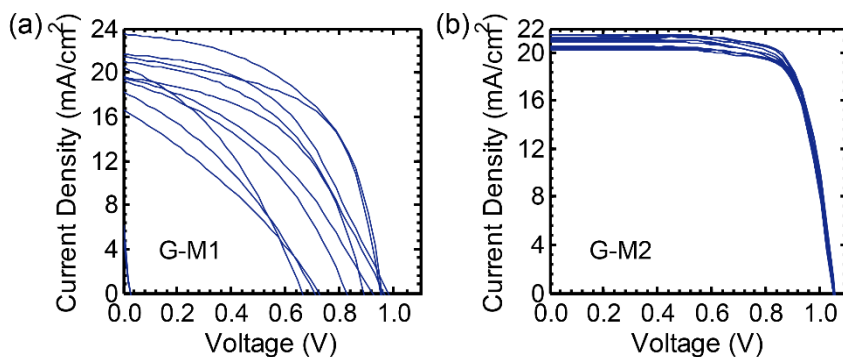


Figure 5.7 J - V curves of (a) G-M1 and (b) G-M2 devices under AM 1.5G illumination at 100 mW cm^{-2} . Non-consistent J - V characteristics appeared in G-M1 devices due to incomplete covering of 1 nm-thick MoO_3 layers over hydrophobic graphene surfaces, resulting in nonuniform formation of PEDOT:PSS and MAPbI_3 films.

Figure 5.7 the PCEs of the G-M0 devices could not be evaluated because neither the PEDOT:PSS nor perovskite solutions wetted the hydrophobic graphene surfaces to form films after spin-coating (also see inset of Figure 5.3a). Even the G-M1 devices exhibited large variation in the PCEs from 0% to 12.1%, which was attributed to a non-uniform coating of PEDOT:PSS on the G-M1 surface. As addressed earlier, the 1 nm-thick MoO_3 layer failed to cover the hydrophobic graphene surface thoroughly. As a result, the current density and voltage (J - V) characteristics were not consistent among devices (See Figure 5.7a). With thicker MoO_3 layers than 1 nm, however, variations in performances among devices became significantly alleviated (see Figure 5.6a and Figure 5.7b), resulting in the average PCEs of 16.1% and 15.9% with the G-M2 and the G-M4 devices, respectively. From the G-M2 device,

the highest PCE of 17.1% was achieved, and, to the best of our knowledge, this is not only the first demonstration of graphene electrodes in perovskite-based solar cells substituting for common TCO electrodes, but also the highest efficiency reported for TCO-free solar cells. For comparison, devices with the same structure but with the ITO electrode were investigated with varied MoO₃ thickness. As shown in Figure 5.6b for the ITO-based devices, the PCE was affected noticeably by a few nanometer changes of the MoO₃ thickness. Utilizing ITO-M1 instead of ITO-M0 electrode increases the average PCE from 17.0% to 18.2%. With the MoO₃ layers thicker than 1 nm, the average PCE of the ITO-M2 and ITO-M4 devices were reduced to 16.1% and 14.7%, respectively. The histogram of the PCEs for each electrode type, G-M2 and ITO-M1, was obtained as shown in Figure 5.8.

The $J-V$ curves for the best-performing G-M2 and ITO-M1 devices under air mass 1.5 global (AM 1.5G) one sun illumination at 100 mW cm⁻² were exhibited in Figure 5.6c and Figure 5.6d, respectively, measured via reverse and forward bias sweep. Both the G-M2 and ITO-M1 devices did not show significant hysteresis by the voltage scan directions, which was similar to the behaviors of the reported solar cells with inverted architecture in other literatures.[14,15] In addition, higher series resistance and lower shunt resistance of the G-M2 device compared to the ITO-M1 device are clearly shown in these figures.

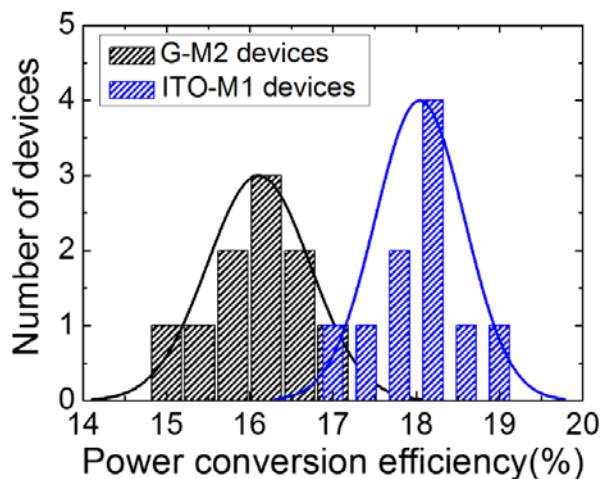


Figure 5.8 PCE Histogram of 10 devices for each electrode type, G-M2 and ITO-M1.

5.3.4. Analysis on Electrical and Optical Properties

To understand the electrical properties of the MoO₃-modified graphene and ITO electrodes, the sheet resistance was measured by a four-point probe. Figure 5.9a shows the relationship between the sheet resistance and the thickness of the MoO₃ layer for graphene and ITO. As shown, the initially high sheet resistance of the as-prepared graphene (>2 kΩ cm⁻²) on a glass substrate was remarkably reduced to ~780 Ω cm⁻² by depositing only a 0.5 nm-thick MoO₃ layer, and decreased further up to ~500 Ω cm⁻² by increasing the thickness of the MoO₃ layer to 2 nm. The sheet resistance of the as-prepared bare ITO was measured as 9.5 Ω cm⁻² and slightly decreased to 9.2 Ω cm⁻² as depositing 1 and 2 nm-thick MoO₃ layers. Although the sheet resistance of the initial single-layer graphene was considerably decreased by over 4-fold owing to the MoO₃ doping,

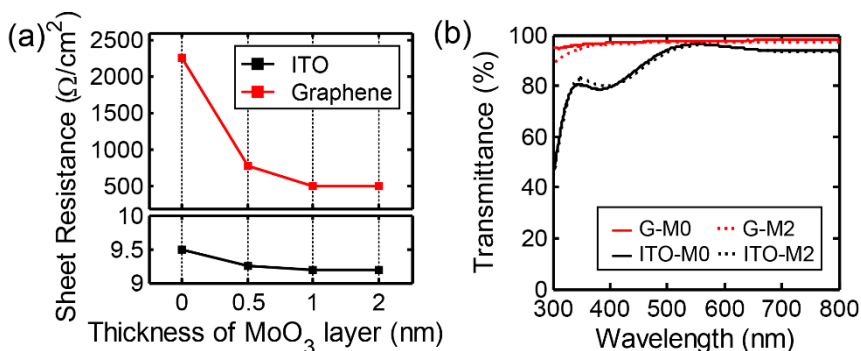


Figure 5.9 (a) Relationship between sheet resistance and MoO_3 thickness for graphene and ITO. (b) Transmittance of graphene and ITO with/without 2 nm-thick MoO_3 layers.

it was still much higher than that of ITO, which resulted in higher series resistance, lower shunt resistance, and lower fill factor (FF) of the G-M2 device than those of the ITO-M1 device. Nevertheless, the G-M2 device exhibited a comparable short-circuit current (J_{sc}) value to the ITO-M1 device due to higher transparency ($\sim 97\%$ transmittance) of the one-atom-thick single-layer graphene than ITO ($\sim 89\%$) over the visible wavelength range, as shown in Figure 5.9b. The EQE spectra for the best-performing G-M2 and ITO-M2 devices were shown in Figure 5.10 from which the integrated photocurrents were calculated as 20.2 and 21.0 mA cm^{-2} , respectively. The EQEs of graphene- and ITO-based devices were similar because the lower carrier collection efficiency of the graphene anode was compensated by its higher optical transmittance (See Figure 5.9b and Figure 5.11) compared to the ITO anode.

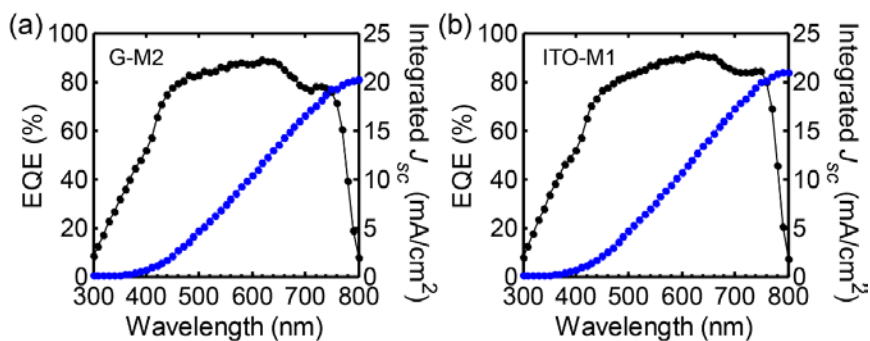


Figure 5.10 EQE spectra (black lines) and integrated J_{sc} (blue lines) of best-performing (a) G-M2 and (b) ITO-M1 devices. The integrated photocurrents were calculated as 20.2 and 21.0 mA cm⁻², respectively.

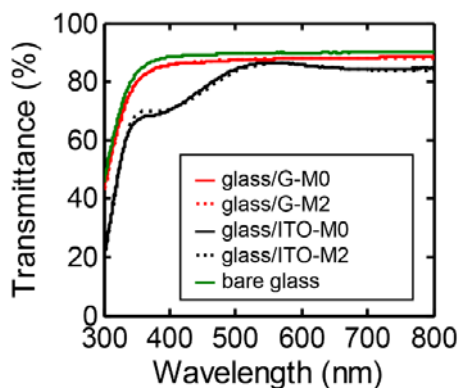


Figure 5.11 Transmittance of glass/graphene and glass/ITO with/without 2 nm-thick MoO₃ layers, and a bare glass substrate.

5.3.5. Analysis on the Open-Circuit Voltage Difference

The G-M2 device showed higher open-circuit voltage (V_{oc}) value than that of the ITO-M1 device, which contributed to the high PCE of the G-M2 device (higher than 90% of that of the ITO-M1 device) despite graphene's

much lower conductivity than ITO. Given the same device structure but electrode, their V_{oc} difference may be related to the work function differences in the electrodes. To investigate the effect of the ultra-thin MoO_3 layer on the work function of the ITO and graphene electrodes, UPS measurements were carried out. Figure 5.12 shows the UPS spectra of the ITO and the graphene electrodes with the MoO_3 layers of varying thickness. As shown in Figure 5.12a, the deposition of a 0.5 nm-thick MoO_3 layer rapidly shifted the secondary electron cutoff of the as-prepared ITO to a higher kinetic energy, indicating the increase of the work function from 4.29 eV to 4.65 eV. Further deposition of the MoO_3 layer to 1 nm and 2 nm in thickness elevated the work function slightly to 4.69 eV and 4.72 eV, respectively. It is desirable to minimize the energy barrier between the anode and the HTL for efficient hole-collection. As shown in the Table 1, the higher J_{sc} and the PCE of the ITO-M1 device than those of the ITO-M0 device were mainly attributed to the increased work function of the electrode, inducing improved hole-collection efficiency. On the other hand, the PCEs decreased as the thickness of the MoO_3 layer increased to 2 and 4 nm. Although thermally evaporated MoO_3 possesses very deep valence band edge, holes can be transported through gap states in the MoO_3 band structure formed near metal contact.[36,37] The hole-collection efficiency of the ITO-M2 and ITO-M4 devices was likely enhanced due to a slight increase in the work function of the electrode by MoO_3 , however, ITO/ MoO_3 /PEDOT:PSS with a thicker MoO_3 layer lacking gap states would not facilitate quasi-ohmic contact for efficient hole extraction [37,38], which resulted in decreased PCE of the ITO-M2 and ITO-M4 devices.

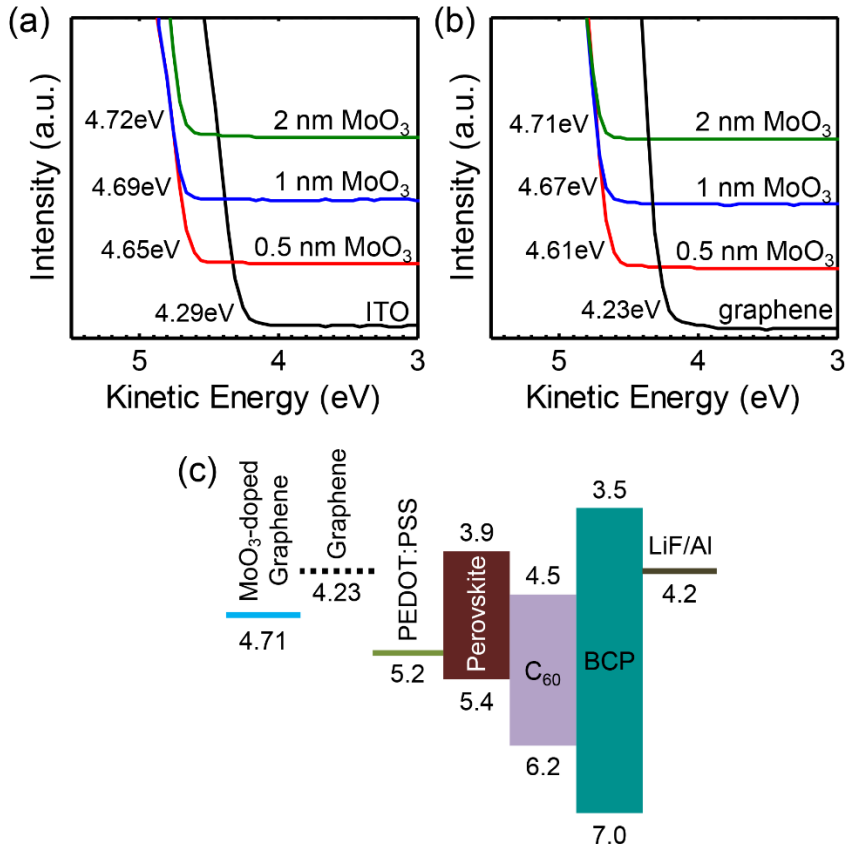


Figure 5.12 (a), (b) UPS spectra and calculated work functions of (a) ITO and (b) graphene with MoO₃ layers of varying thickness. (c) Schematic energy level diagram of the fabricated inverted structure. The energy levels are taken from Jeng et al.[39] The work function of as-prepared graphene (denoted by black dashed line, 4.23 eV) was increased to 4.71 eV by MoO₃ doping (denoted by blue solid line).

The UPS spectra of the graphene-based devices also showed a similar behavior to that of the ITO devices with the deposition of the MoO₃ layer.

As shown in Figure 5.12b, a rapid shift of the onset of photoemission was observed on depositing a 0.5 nm-thick MoO₃ layer on the as-prepared graphene, indicating the increase of the work function from 4.23 eV to 4.61 eV. Further deposition of the MoO₃ layer to 1 nm and 2 nm in thickness increased the work function slightly to 4.67 eV and 4.71 eV, respectively. As illustrated in Figure 5.12c, the ultra-thin MoO₃ layer deposited on graphene consequently facilitated hole collection from the HTL to the graphene anode by reducing the energy barrier at the interface, as well as allowing the PEDOT:PSS film to be successfully spin-coated on the hydrophobic graphene surfaces. Comparing the UPS data for the ITO and the graphene electrodes, the work functions with the same MoO₃ thickness were found to be almost the same. The work function values of the ITO-M1 and G-M2 electrodes also showed no significant difference, implying that the higher V_{oc} of the G-M2 device than that of the ITO-M1 device could not be explained in terms of the energy barrier difference at the anode/HTL interfaces. Since V_{oc} also can be influenced by the interface quality, atomic force microscopy (AFM) measurement was carried out to study the morphology of the electrodes after the formation of the MoO₃ and the PEDOT:PSS films. As shown in Figure 5.13a – Figure 5.13c, the surface root-mean-square (rms) roughnesses for G-M0, G-M2, and G-M2/PEDOT:PSS were measured as 0.47, 0.29 and 0.98 nm, respectively. The rms roughnesses for ITO-M0, ITO-M1 and ITO-M1/PEDOT:PSS were found to be 2.06, 1.95 and 1.21 nm, respectively, as shown in Figure 5.13d – Figure 5.13f. It is noticeable here that G-M2 showed more than 6-fold lower surface rms roughness of 0.29 nm than that of ITO-M1 (1.95 nm rms roughness). From the literature,[40] it is

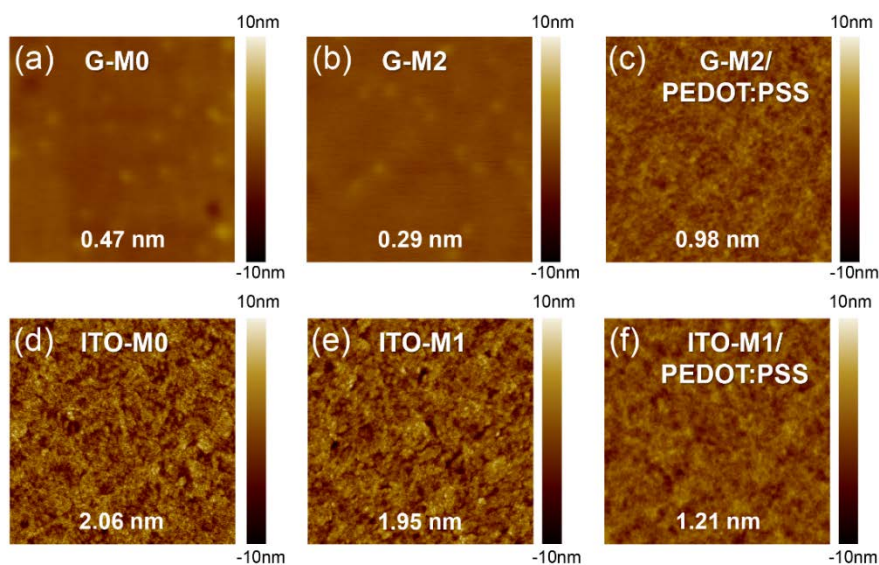


Figure 5.13 AFM topography images ($3 \mu\text{m} \times 3 \mu\text{m}$) of (a) as-prepared graphene, (b) graphene/2 nm MoO_3 , (c) graphene/2 nm MoO_3 after spin-coating of PEDOT:PSS, (d) as-prepared ITO, (e) ITO/1 nm MoO_3 , (f) ITO/1 nm MoO_3 after spin-coating of PEDOT:PSS. The calculated surface rms roughness values were presented in each figure.

known that better interface can be created between stacked layers when the surface roughness of the underlying layer is smaller, which consequently increases V_{oc} . In this respect, the G-M2 electrode seemed to have established better interfaces with PEDOT:PSS than ITO-M1/PEDOT:PSS interfaces, contributing to the higher V_{oc} of the G-M2 devices.

Moreover, it was observed from the SEM images of the perovskite surfaces formed on G-M2/PEDOT:PSS and ITO-M1/PEDOT:PSS, as shown in Figure 5.14, that the overall grain size of the former was larger than that of the latter. The X-ray diffraction patterns of the perovskite films fabricated on G-M2/PEDOT:PSS and ITO-M1/PEDOT:PSS were also provided information on the difference in grain size. It is noticeable in Figure 5.15 that the peak intensities of the (110) and (220) planes for the G-M2 sample are much stronger than those for the ITO-M1 sample. Recently, it was reported that abnormal grain growth behavior of a perovskite film involved a preferred grain orientation.[41,42] In our work, the well-oriented grains on graphene electrode most likely originated from the smaller surface roughness of the underlying layer of the perovskite film. The nano-scale edges of the surface of the underlying layer could serve as nucleation sites and induce formation of randomly oriented grains. In this respect, the grains of the perovskite film on the smoother G-M2/PEDOT:PSS surface could grow to a larger size than those on the ITO-M1/PEDOT:PSS surface. Furthermore, the well-oriented larger grains of the G-M2 devices can be regarded as another factor for the higher V_{oc} in the G-M2 devices compared to the ITO-M1 devices due to reduction in defect-assisted recombination loss at grain boundaries.[43-45]

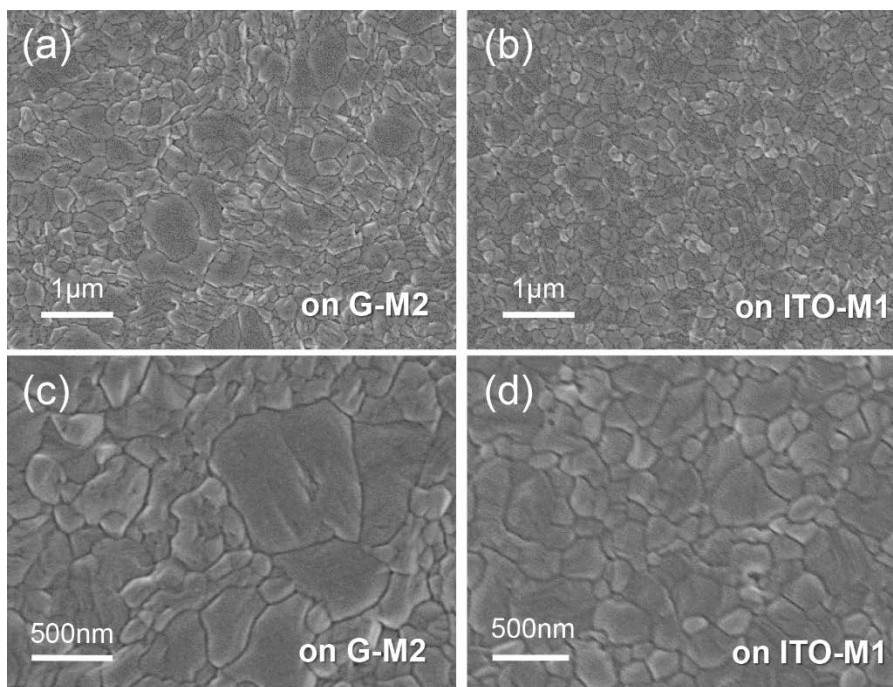


Figure 5.14 Plan-view SEM images of the MAPbI_3 perovskite films fabricated on (a) G-M2/PEDOT:PSS and (b) ITO-M1/PEDOT:PSS surfaces. (c) and (d) are the higher magnification images of (a) and (b), respectively.

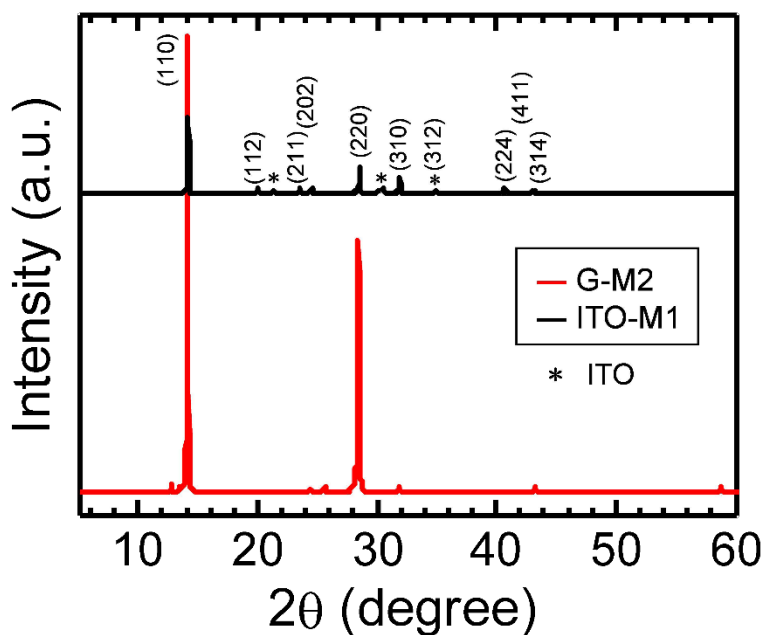


Figure 5.15 X-ray diffraction patterns of G-M2/PEDOT:PSS/MAPbI₃ and ITO-M1/PEDOT:PSS/MAPbI₃. Peaks for perovskite films were observed identically in the X-ray diffraction patterns for both G-M2 and ITO-M1 samples although all the peaks were not seen clearly for the G-M2 sample due to the large difference in intensity among them. It is noticeable that the (110) and (220) peak intensities of the G-M2 sample is much stronger than those of the ITO-M1 sample, which implies that the MAPbI₃ film was formed with better alignment of the grain orientation on the smoother graphene surface than on the relatively rough ITO surface.

5.4. Conclusion

Not only the first perovskite solar cells employing graphene as a transparent conducting anode but also the highest efficiency TCO-free solar cells have been demonstrated. Both graphene- and ITO-based inverted devices with thin MoO₃ interfacial layers of varying thickness have been fabricated for comparison. Interfacial engineering by introduction of a MoO₃ layer on the anode surface enables a better interface formation and a desirable energy level alignment between the anode and the HTL. In particular, MoO₃ dopes holes into graphene allowing it to better serve as a conducting electrode. With the optimized thickness of the MoO₃ layer, best PCEs of 17.1% and 18.8% have been achieved with the graphene- and the ITO-based devices, respectively. The significantly lower conductivity of the graphene electrode than that of the ITO electrode is compensated by graphene's higher transparency and lower surface roughness, leading to comparable J_{sc} , higher V_{oc} , and consequent >90% PCE of the graphene device compared to the ITO device. The present work may highlight the great potential of graphene as a transparent electrode and provide new insights into future studies for developing robust flexible solar cells with high efficiency.

5.5. References

- [1] A. Kojima, K. Teshima, Y. Shirai, T. Miyasaka, "Organometal halide perovskites as visible-light sensitizers for photovoltaic cells", *J. Am. Chem. Soc.*, **131**, 6050-6051 (2009)
- [2] J.-H. Im, C.-R. Lee, J.-W. Lee, S.-W. Park, N.-G. Park, "6.5% efficient perovskite quantum-dot-sensitized solar cell", *Nanoscale*, **3**, 4088-4093 (2011)
- [3] H.-S. Kim, C.-R. Lee, J.-H. Im, K.-B. Lee, T. Moehl, A. Marchioro, S.-J. Moon, R. Humphry-Baker, J.-H. Yum, J.E. Moser, M. Grätzel, N.-G. Park, "Lead Iodide perovskite sensitized all-solid-state submicron thin film mesoscopic solar cell with efficiency exceeding 9%", *Sci. Rep.*, **2**, 591 (2012)
- [4] G. Xing, N. Mathews, S. Sun, S.S. Lim, Y.M. Lam, M. Grätzel, S. Mhaisalkar, T.C. Sum, "Long-range balanced electron- and hole transport lengths in organic-inorganic CH₃NH₃Pb₃", *Science*, **342**, 344-347 (2013)
- [5] P. Docampo, J.M. Ball, M. Darwich, G.E. Eperon, H.J. Snaith, "Efficient organometal trihalide perovskite planar-heterojunction solar cells on flexible polymer substrates", *Nat. Commun.*, **4**, 2761 (2013)
- [6] S.D. Stranks, G.E. Eperon, G. Grancini, C. Menelaou, M.J.P. Alcocer, T. Leijtens, L.M. Herz, A. Petrozza, H.J. Snaith, "Electron-hole diffusion lengths exceeding 1 micrometer in an organometal trihalide perovskite absorber", *Science*, **342**, 341-344 (2013)
- [7] W. Ke, G. Fang, J. Wan, H. Tao, Q. Liu, L. Xiong, P. Qin, J. Wang, H. Lei, G. Yang, M. Qin, X. Zhao, Y. Yan, "Efficient hole-blocking layer-

free planar halide perovskite thin-film solar cells", *Nat. Commun.*, **6**, 6700 (2015)

[8] W. Ke, G. Fang, Q. Liu, L. Xiong, P. Qin, H. Tao, J. Wang, H. Lei, B. Li, J. Wan, G. Yang, Y. Yan, "Low-Temperature Solution-Processed Tin Oxide as an Alternative Electron Transporting Layer for Efficient Perovskite Solar Cells", *J. Am. Chem. Soc.*, **137**, 6730-6733 (2015)

[9] J.M. Ball, M.M. Lee, A. Hey, H.J. Snaith, "Low-temperature processed meso-superstructured to thin-film perovskite solar cells", *Energy Environ. Sci.*, **6**, 1739 (2013)

[10] J.H. Heo, S.H. Im, J.H. Noh, T.N. Mandal, C.-S. Lim, J.A. Chang, Y.H. Lee, H.-j. Kim, A. Sarkar, K. NazeeruddinMd, M. Gratzel, S.I. Seok, "Efficient inorganic-organic hybrid heterojunction solar cells containing perovskite compound and polymeric hole conductors", *Nat. Photonics*, **7**, 486-491 (2013)

[11] G.E. Eperon, V.M. Burlakov, P. Docampo, A. Goriely, H.J. Snaith, "Morphological control for high performance, solution-processed planar heterojunction perovskite solar cells", *Adv. Funct. Mater.*, **24**, 151-157 (2014)

[12] O. Malinkiewicz, A. Yella, Y.H. Lee, G.M. Espallargas, M. Graetzel, M.K. Nazeeruddin, H.J. Bolink, "Perovskite solar cells employing organic charge-transport layers", *Nat. Photonics*, **8**, 128-132 (2014)

[13] J. You, Z. Hong, Y. Yang, Q. Chen, M. Cai, T.-B. Song, C.-C. Chen, S. Lu, Y. Liu, H. Zhou, Y. Yang, "Low-temperature solution-processed perovskite solar cells with high efficiency and flexibility", *ACS Nano*, **8**, 1674-1680 (2014)

[14] J. Seo, S. Park, Y. Chan Kim, N.J. Jeon, J.H. Noh, S.C. Yoon, S.I.

- Seok, "Benefits of very thin PCBM and LiF layers for solution-processed p-i-n perovskite solar cells", *Energy Environ. Sci.*, **7**, 2642-2646 (2014)
- [15] J.H. Heo, H.J. Han, D. Kim, T.K. Ahn, S.H. Im, "Hysteresis-less inverted CH₃NH₃PbI₃ planar perovskite hybrid solar cells with 18.1% power conversion efficiency", *Energy Environ. Sci.*, **8**, 1602-1608 (2015)
- [16] B.J. Kim, D.H. Kim, Y.-Y. Lee, H.-W. Shin, G.S. Han, J.S. Hong, K. Mahmood, T.K. Ahn, Y.-C. Joo, K.S. Hong, N.-G. Park, S. Lee, H.S. Jung, "Highly efficient and bending durable perovskite solar cells: toward a wearable power source", *Energy Environ. Sci.*, **8**, 916-921 (2015)
- [17] J. Wu, H.A. Becerril, Z. Bao, Z. Liu, Y. Chen, P. Peumans, "Organic solar cells with solution-processed graphene transparent electrodes", *Appl. Phys. Lett.*, **92**, 263302 (2008)
- [18] Y. Wang, S.W. Tong, X.F. Xu, B. Özyilmaz, K.P. Loh, "Interface engineering of layer-by-layer stacked graphene anodes for high-performance organic solar cells", *Adv. Mater.*, **23**, 1514-1518 (2011)
- [19] H. Park, S. Chang, X. Zhou, J. Kong, T. Palacios, S. Gradecak, "Flexible graphene electrode-based organic photovoltaics with record-high efficiency", *Nano Lett.*, **14**, 5148-5154 (2014)
- [20] A.R.b. Mohd Yusoff, D. Kim, F.K. Schneider, W.J. da Silva, J. Jang, "Au-doped single layer graphene nanoribbons for a record-high efficiency ITO-free tandem polymer solar cell", *Energy Environ. Sci.*, **8**, 1523-1537 (2015)
- [21] M.W. Rowell, M.A. Topinka, M.D. McGehee, H.-J. Prall, G. Dennler, N.S. Sariciftci, L. Hu, G. Gruner, "Organic solar cells with carbon nanotube network electrodes", *Appl. Phys. Lett.*, **88**, 233506 (2006)

- [22] I. Jeon, K. Cui, T. Chiba, A. Anisimov, A.G. Nasibulin, E.I. Kauppinen, S. Maruyama, Y. Matsuo, "Direct and dry deposited single-walled carbon nanotube films doped with MoO_x as electron-blocking transparent electrodes for flexible organic solar cells", *J. Am. Chem. Soc.*, **137**, 7982-7985 (2015)
- [23] R.V. Salvatierra, C.E. Cava, L.S. Roman, A.J.G. Zarbin, "ITO-free and flexible organic photovoltaic device based on high transparent and conductive polyaniline/carbon nanotube thin films", *Adv. Funct. Mater.*, **23**, 1490-1499 (2013)
- [24] B. Muhsin, R. Roesch, G. Gobsch, H. Hoppe, "Flexible ITO-free polymer solar cells based on highly conductive PEDOT:PSS and a printed silver grid", *Sol. Energy Mater. Sol. Cells*, **130**, 551-554 (2014)
- [25] J. Zou, H.-L. Yip, S.K. Hau, A.K.-Y. Jen, "Metal grid/conducting polymer hybrid transparent electrode for inverted polymer solar cells", *Appl. Phys. Lett.*, **96**, 203301 (2010)
- [26] M. Song, H.-J. Kim, C.S. Kim, J.-H. Jeong, C. Cho, J.-Y. Lee, S.-H. Jin, D.-G. Choi, D.-H. Kim, "ITO-free highly bendable and efficient organic solar cells with Ag nanomesh/ZnO hybrid electrodes", *J. Mater. Chem. A*, **3**, 65-70 (2015)
- [27] Y.H. Kim, C. Sachse, M.L. Machala, C. May, L. Müller-Meskamp, K. Leo, "Highly conductive PEDOT:PSS electrode with optimized solvent and thermal post-treatment for ito-free organic solar cells", *Adv. Funct. Mater.*, **21**, 1076-1081 (2011)
- [28] W. Zhang, B. Zhao, Z. He, X. Zhao, H. Wang, S. Yang, H. Wu, Y. Cao, "High-efficiency ITO-free polymer solar cells using highly conductive

PEDOT:PSS/surfactant bilayer transparent anodes", *Energy Environ. Sci.*, **6**, 1956-1964 (2013)

[29] K. Sun, P. Li, Y. Xia, J. Chang, J. Ouyang, "Transparent conductive oxide-free perovskite solar cells with PEDOT:PSS as transparent electrode", *ACS Appl. Mater. Inter.*, **7**, 15314-15320 (2015)

[30] P. You, Z. Liu, Q. Tai, S. Liu, F. Yan, "Efficient semitransparent perovskite solar cells with graphene electrodes", *Adv. Mater.*, **27**, 3632-3638 (2015)

[31] K. Yan, Z. Wei, J. Li, H. Chen, Y. Yi, X. Zheng, X. Long, Z. Wang, J. Wang, J. Xu, S. Yang, "High-performance graphene-based hole conductor-free perovskite solar cells: schottky junction enhanced hole extraction and electron blocking", *Small*, **11**, 2269-2274 (2015)

[32] H. Sung, N. Ahn, M.S. Jang, J.-K. Lee, H. Yoon, N.-G. Park, M. Choi, "Transparent conductive oxide-free graphene-based perovskite solar cells with over 17% efficiency", *Adv. Energy Mater.*, n/a-n/a (2015)

[33] W.H. Lee, J. Park, S.H. Sim, S.B. Jo, K.S. Kim, B.H. Hong, K. Cho, "Transparent flexible organic transistors based on monolayer graphene electrodes on plastic", *Adv. Mater.*, **23**, 1752-1756 (2011)

[34] N. Ahn, D.-Y. Son, I.-H. Jang, S.M. Kang, M. Choi, N.-G. Park, "Highly reproducible perovskite solar cells with average efficiency of 18.3% and best efficiency of 19.7% fabricated via Lewis base adduct of Lead(II) Iodide", *J. Am. Chem. Soc.*, **137**, 8696-8699 (2015)

[35] J. Meyer, P.R. Kidambi, B.C. Bayer, C. Weijtens, A. Kuhn, A. Centeno, A. Pesquera, A. Zurutuza, J. Robertson, S. Hofmann, "Metal oxide induced charge transfer doping and band alignment of graphene electrodes

- for efficient organic light emitting diodes", *Sci. Rep.*, **4**, 5380 (2014)
- [36] P. Qin, G. Fang, W. Ke, F. Cheng, Q. Zheng, J. Wan, H. Lei, X. Zhao, "In situ growth of double-layer MoO₃/MoS₂ film from MoS₂ for hole-transport layers in organic solar cell", *J. Mater. Chem. A*, **2**, 2742 (2014)
- [37] M.T. Greiner, L. Chai, M.G. Helander, W.-M. Tang, Z.-H. Lu, "Metal/metal-oxide interfaces: how metal contacts affect the work function and band structure of MoO₃", *Adv. Funct. Mater.*, **23**, 215-226 (2013)
- [38] Z. Liu, M. Kobayashi, B.C. Paul, Z. Bao, Y. Nishi, "Contact engineering for organic semiconductor devices via Fermi level depinning at the metal-organic interface", *Phys. Rev. B*, **82**, 035311 (2010)
- [39] J.-Y. Jeng, Y.-F. Chiang, M.-H. Lee, S.-R. Peng, T.-F. Guo, P. Chen, T.-C. Wen, "CH₃NH₃PbI₃ perovskite/fullerene planar-heterojunction hybrid solar cells", *Adv. Mater.*, **25**, 3727-3732 (2013)
- [40] N. Kang, M. Hoang, D. Choi, B.-K. Ju, J.-M. Hong, J.-W. Yu, "Enhanced performance of organic photovoltaic devices by photocrosslinkable buffer layer", *Macromol. Res.*, **21**, 65-70 (2013)
- [41] Q. Dong, Y. Yuan, Y. Shao, Y. Fang, Q. Wang, J. Huang, "Abnormal crystal growth in CH₃NH₃PbI₃-xCl_x using a multi-cycle solution coating process", *Energy Environ. Sci.*, **8**, 2464-2470 (2015)
- [42] W.S. Yang, J.H. Noh, N.J. Jeon, Y.C. Kim, S. Ryu, J. Seo, S.I. Seok, "High-performance photovoltaic perovskite layers fabricated through intramolecular exchange", *Science*, **348**, 1234-1237 (2015)
- [43] W. Nie, H. Tsai, R. Asadpour, J.-C. Blancon, A.J. Neukirch, G. Gupta, J.J. Crochet, M. Chhowalla, S. Tretiak, M.A. Alam, H.-L. Wang, A.D. Mohite, "High-efficiency solution-processed perovskite solar cells with

millimeter-scale grains", *Science*, **347**, 522-525 (2015)

[44] J. You, Y. Yang, Z. Hong, T.-B. Song, L. Meng, Y. Liu, C. Jiang, H. Zhou, W.-H. Chang, G. Li, Y. Yang, "Moisture assisted perovskite film growth for high performance solar cells", *Appl. Phys. Lett.*, **105**, 183902 (2014)

[45] Q. Chen, H. Zhou, Z. Hong, S. Luo, H.-S. Duan, H.-H. Wang, Y. Liu, G. Li, Y. Yang, "Planar heterojunction perovskite solar cells via vapor-assisted solution process", *J. Am. Chem. Soc.*, **136**, 622-625 (2014)

Chapter 6.

Concluding Remarks

This dissertation has investigated performance enhancement of devices based on organic materials and graphene, such as an OLED, a graphene FET, and a graphene perovskite solar cell, by interfacial layer engineering.

First, by precisely positioning Au NPs in a specific plane in an OLED, the EQE has increased by maximum 38% from that of the control device without metal NPs. The typically used methods for incorporating metal NPs in an organic layer, such as vacuum thermal evaporation or spin coating, can degrade the underlying organic materials that are vulnerable to heat, moisture and chemicals, and may not allow for metal NPs to be located at a controlled vertical position in an organic layer. Due to these limitations of the existing fabrication methods, an OLED has not been fully employing the benefits that metal NPs offer although performance increase of metal NP-embedded OLEDs has been widely expected. In this work, charged Au NPs have been deposited via weak electrostatic force on the surface of an organic layer using a dry, room temperature aerosol technique, and thus can be incorporated in a specific plane in an OLED while not damaging the underlying organic materials. This study is the first experimental work to investigate the effect of the position of metal NPs in an OLED on the device characteristics with in-depth analysis by distinguishing the factor of changing the electrical property from that of changing the optical property. In addition, this is the first report of combining aerosol technology with organic device fabrication technology. In these respects, this study may provide an insight to design not only a new metal NP enhanced OLED but also a new aerosol-NP enhanced organic electronic/optoelectronic devices.

Secondly, reliable control of doping type and doping level of graphene has been realized by controlled deposition of aerosol-derived metal NPs on the channel of a graphene FET. When metal NPs are deposited on graphene surface, electron transfer occurs at the interface between the metal NPs and graphene because of their work function difference, resulting in p-type or n-type doping of graphene. Tailoring the doping type and doping level of graphene with metal NPs has been demonstrated employing commonly used methods for depositing metal NPs, such as vacuum thermal evaporation and spin coating. However, the results are not satisfactory in a precisely controlled manner, for example doping type changes from p-type to n-type because the morphology of metal NPs changes along with the deposition amount or random aggregation of NPs occurs not making a uniformly distributed layer. In this work, metal NPs with a fairly narrow size distribution are deposited on graphene channels using an aerosol technique that is capable of controlling size, shape, and deposited density of NPs independently. As a result, both doping type and doping level of graphene can be reliably modulated according to the materials of the metal NPs deposited – Ag and Pt NPs induce n-type and p-type doping, respectively – and the deposition amount, respectively. In this regard, the present work is capable of being applied to future CMOS circuit or pn junction devices based on graphene.

Thirdly, highly efficient TCO-free inverted perovskite solar cells have been fabricated by employing graphene as a transparent anode. For the reliable flexible photovoltaic devices, bendable transparent electrodes are essential, and graphene, which is optically highly transparent, mechanically

robust, flexible, and stretchable, is one of the promising candidates. However, superhydrophobicity and low electrical conductivity of graphene hinder reliable fabrication and high performance of the devices. In order to overcome these obstacles, a few nanometer thick MoO_3 layer has been introduced on graphene surface by vacuum thermal evaporation so that graphene surface changes to hydrophilic to enable uniform fabrication of HTL, and hole-doping in graphene is induced to improve graphene's electrical conductivity. As a result, graphene-based perovskite solar cells presenting the best PCE of 17.1% and the average PCE of 16.1% have been obtained, which is so far the record-high efficiency for TCO-free solar cells. As a basic research work that points out the suitability and the potential of graphene to be utilized as a transparent electrode in high efficiency perovskite solar cells, the present work may provide new insights into future studies for developing robust flexible solar cells with high efficiency.

계면제어기술을 통한 전자 및 광전자 소자의 성능 향상

서울대학교 대학원 기계항공공학부

성 향 기

요약

전자 및 광전자소자 성능에 있어서 적절한 계면층의 선택은 매우 중요하다. 특히 전하수송체(charge carrier)의 이동이 성능에 밀접한 관련이 있는 전자 및 광전자소자는 정공 또는 전자 도핑으로 인한 계면층의 전기적 특성 변화를 통해 소자의 성능 개선이 가능하다. 최근 수 년간 유기물질과 그래핀은 유연성 소자나 투명 소자와 같은 차세대 전자 소자의 응용 가능성으로 인해 많은 연구적 관심을 받아왔다. 그러나 이들은 고 에너지 공정이 관여된 기존의 도핑 공정에 의해 쉽게 손상될 수 있고, 특히 유기물질은 화학물질에 쉽게 변형되기 때문에 도핑으로 전기적 특성을 변화시킬 수 있는 실험적인 방법이 제한적이다. 본 연구는 계면제어기술을 통하여 유기발광다이오드 (OLED), 그래핀 전계효과 트랜지스터 (FET) 및 그래핀 페로브스카이트 태양전지로 선택된 유기소자 및 그래핀 응용 소자의 성능 개선을 실험적으로 구현하였다.

첫째로 유기발광다이오드(OLED) 내에 금 나노입자층을 유기물의 손상 없이 도입하여 최고 38%의 외부양자효율 증가를 얻었다. 금속나노입자 도입을 통한 OLED의 효율 향상 가능성은 이론적으로

익히 예상되는 바였으나, 기존의 금속나노입자층을 형성하는 열증착 및 스펀코팅 방법이 열, 수분, 화학물질에 취약한 유기물 층을 손상시키거나 입자의 위치제어가 불가능한 제약으로 인해 실제적인 구현이 어려웠다. 본 연구는 상온, 상압 공정의 에어로졸 방법을 이용하여 하전된 금 나노입자를 약한 정전기력으로 유기물 표면에 부착시킬 수 있었고, 이를 통하여 하부 유기물 층으로의 침투나 유기물의 손상 없이 OLED 내 특정 평면에 선택적으로 나노입자층을 도입할 수 있었다. 이를 통하여 OLED 층 내 나노입자의 위치가 OLED 소자 구동에 미치는 영향을 처음으로 실험적으로 분석하였고, 그 동안 해당 연구에서 간과되었던 금속나노입자에 의한 소자 내의 전기장 분포 변화를 광학적 특성 변화와 구별하여 보임으로써 금속나노입자가 도입된 OLED 소자의 효율 변화 요인을 보다 면밀하게 분석할 수 있었다.

둘째로 에어로졸 금속나노입자를 통하여 그래핀의 도핑 타입 및 도핑 레벨을 일관성 있게 제어할 수 있음을 보이고, 이를 그래핀 전계효과 트랜지스터로 평가하였다. 금속나노입자-그래핀 계면을 형성하게 되면 해당 계면에서 금속나노입자와 그래핀의 일함수 차이에 의한 전자 이동이 유발되어 그래핀이 p형 또는 n형으로 도핑되게 된다. 기존의 금속나노입자층을 형성하는 열증착 및 스펀코팅 방법은 입자의 크기, 모양 제어가 불가하거나(입자에서 박막으로 성장) 입자 간에 불규칙 응집으로 인하여 그래핀의 도핑타입이 금속입자층의 증착량에 따라 n형에서 p형으로 바뀌는 등 일관되게 제어되지 않는 문제가 있었다. 본 연구에서는 에어로졸 방법을 통하여 금속 나노입자의 크기 및 모양을 일관되게 유지하면서 고른 밀도 분포의 나노입자층을 형성하였고, 그 결과

입자 종류(Ag 또는 Pt) 및 증착 밀도 따라 그래핀의 도핑 타입(n형 또는 p형) 및 도핑 레벨을 일관성 있게 제어할 수 있었다.

셋째로 기존의 투명전도성산화물(TCO) 전극을 그래핀으로 대체한 고효율의 페로브스카이트 태양전지를 구현하였다. 그래핀의 경우 우수한 투명도, 유연성, 강도, 열전도성, 내약품성으로 인해 차세대 유연성 소자 개발에 있어 기존의 ITO로 대표되는 깨짐성 있는 TCO 전극의 대체물로서 기대를 받고 있다. 그러나 그래핀의 극소수성 및 낮은 전기전도도는 안정된 소자 구현 및 소자 성능에 있어서 걸림돌로 작용하고 있다. 이를 해결하기 위하여 수 나노미터 두께의 산화몰리브덴 (MoO_3) 박막을 진공열증착방법으로 그래핀 표면에 도입하였다. MoO_3 층으로 인해 그래핀의 표면이 친수성으로 변화되어 그래핀 위에 정공수송층으로 대표되는 PEDOT:PSS의 안정적인 형성이 가능해졌을 뿐만 아니라 MoO_3 에 의한 그래핀의 정공 도핑으로 그래핀의 전기전도도가 향상되었다. 그 결과, 최고효율 17.1%, 평균효율 16.1%의 고효율의 그래핀 페로브스카이트 태양전지를 구현할 수 있었고, 이는 TCO 전극을 대체한 제 3세대 태양전지를 통틀어 세계 최고 효율이다. 또한 MoO_3 층을 기존의 ITO 기반 페로브스카이트 태양전지에 적용하여서도 최고효율 18.8%, 평균효율 18.2%로 역 구조 페로브스카이트 태양전지 중에 최고 효율을 보였다.

주요어: 나노입자, 에어로졸, 그래핀, 광전소자, 유기발광소자, 그래핀 전계효과 트랜지스터, 페로브스카이트 태양전지

학번: 2010-20686

List of Publications

- [1] **H. Sung**[†], N. Ahn[†], M.S. Jang, J.-K. Lee, H. Yoon, N.-G. Park, M. Choi, "Transparent Conductive Oxide-Free Graphene-Based Perovskite Solar Cells with over 17% Efficiency", *Advanced Energy Materials*, (2015) ([†] equally contributed) (**Front Cover**)
- [2] J.-K. Lee, **H. Sung**, M.S. Jang, H. Yoon, M. Choi, "Reliable Doping and Carrier Concentration Control in Graphene by Aerosol-Derived Metal Nanoparticles", *Journal of Materials Chemistry C*, 3, 8294-8299 (2015) (**Front Cover**)
- [3] **H. Sung**[†], J. Lee[†], K. Han, J.-K. Lee, J. Sung, D. Kim, M. Choi, C. Kim, "Controlled Positioning of Metal Nanoparticles in an Organic Light-Emitting Device for Enhanced Quantum Efficiency", *Organic Electronics*, 15, 491-499 (2014) ([†] equally contributed)
- [4] **H. Sung**, M. Choi, "Assembly of Nanoparticles: Towards Multiscale Three-Dimensional Architecturing", *KONA Powder and Particle Journal*, 30, 31-46 (2013)

Conferences

Oral Presentations

- [1] **H. Sung**, J. Lee, K. Han, J.-K. Lee, M. Choi, C. Kim, "Incorporation of Size-Controlled Aerosol Particles for Enhanced Efficiency of Optoelectronic Devices", International Aerosol Conference, Pusan, Korea (2014)
- [2] **H. Sung**, J. Lee, K. Han, J.-K. Lee, C. Kim, M. Choi, "Controlled Positioning of Aerosol Nanoparticles in an Organic Light-Emitting Device for Enhanced Quantum Efficiency", Korean Particle and Aerosol Conference, Yongpyong, Korea (2013) (**Best Paper Award**)

Poster Presentations

- [1] **H. Sung**, N. Ahn, M.S. Jang, J.-K. Lee, H. Yoon, N.-G. Park, M. Choi, "Highly efficient inverted perovskite solar cells with graphene electrodes", Materials Research Society Fall Meeting, Boston, USA (2015)
- [2] H. Yoon, J.-K. Lee, **H. Sung**, M.S. Jang, M. Choi, "A Study on MoO₃ in Fullerene-Based Schottky Junction Solar Cells", Materials Research Society Fall Meeting, Boston, USA (2015)
- [2] **H. Sung**, J. Lee, K. Han, J.-K. Lee, C. Kim, M. Choi, "Positioning of Nano-Sized Noble Metal Aerosols in an Organic Light-Emitting Diode for Enhanced Quantum Efficiency", European Aerosol Conference, Prague, Czech Republic (2015)